Investigations on Additive Manufacturing of Metallic Materials by Micro-Plasma Transferred Arc Powder Deposition Process

Ph.D. Thesis

By

Sawant Mayur Sudhakar

Discipline of Mechanical Engineering

Indian Institute of Technology Indore

April 2018

Investigations on Additive Manufacturing of Metallic Materials by Micro-Plasma Transferred Arc Powder Deposition Process

A Thesis

Submitted in partial fulfillment of the

requirements for the award of the degree

of

Doctor of Philosophy

By

Sawant Mayur Sudhakar

Discipline of Mechanical Engineering

Indian Institute of Technology Indore

April 2018

Indian Institute of Technology Indore

Candidate's Declaration

I hereby certify that the work which is being presented in the thesis entitled **Investigations on Additive Manufacturing of Metallic Materials by Micro-plasma Transferred Arc Powder Deposition Process,** in the partial fulfillment of the requirements for the award of the degree of **DOCTOR OF PHILOSOPHY** and submitted in the **Discipline of Mechanical Engineering, Indian Institute of Technology Indore**, is an authentic record of my own work carried out during the time period from **Jan 2014 to April 2018** under the supervision of **Prof. Neelesh Kumar Jain**, and **Dr. I. A. Palani** of Discipline of Mechanical Engineering.

The matter contained in this thesis has not been submitted by me for the award of any degree from any other institute.

(Sawant Mayur Sudhakar)

This is to certify that the above statement made by the candidate is correct to the best of our knowledge.

05/04/2018 5/4/2018

(Prof. Neelesh Kumar Jain) **(Dr. I. A. Palani)**

Sawant Mayur Sudhakar has successfully completed his Ph.D. Oral Examination held on **..........**

Signature of Thesis Supervisors
Date:

Signature of Convener, DPGC
Date:

Signature of PSPC Members
Date:

Signature of External Examiner
Date:

Signature (with date) of Chairman of PhD Oral Examination Board

Acknowledgements

First and Foremost, I would like to thank my supervisors **Prof. Neelesh Kumar Jain** and **Dr. I. A. Palani** for providing me with the opportunity to complete my PhD thesis at **Indian Institute of Technology, Indore**. As my supervisors, they have constantly forced me to remain focused towards achieving my goal. Their observations and comments helped me to establish the overall direction of the research and to move forward with investigation in depth. I am very grateful for their patience, motivation, enthusiasm, and immense knowledge in advanced manufacturing processes and especially in additive manufacturing that taken together, make them a great mentor.

I am extremely happy to express my gratitude towards my PSPC members **Dr. Santosh K. Sahu** and **Dr. Vipul Singh** for their guidance and co-operation. I am grateful to the **Prof. Pradeep Mathur, Director**, **IIT Indore** and **Dr. Satyajit Chatterjee, Dr. Devendra Deshmukh, Prof. Anand Parey, Dr. Sunil Kumar and faculty members** of Discipline of **Mechanical Engineering** for providing the essential facilities and guidance.

I want to thank past scholars of the Advanced Manufacturing Lab **Dr. Suyog Jhavar** for giving me an introduction into the Additive Manufacturing and for sharing his knowledge and expertise. I would also like to thank and express my gratitude towards **Dr. Sagar Nikam, Mr. Sujeet K. Chaubey, Mr. Aniket Kulkarni, Mr. Debjit Misra, Mr. Pravin Kumar, Mr. Vishal Kharka, Dr. Kinny Pandey, Mr. Nitin Upadhyay, Dr. Sambhaji Kadam, Dr. Sunil Pathak** and **Mr. Balmukund Dhakar** for motivating me and helping me during the tough phases of my research. Special thanks to my friends of IIT Indore **Anshu Mishra**, **Rajagopalan**, **Sagnik Sengupta**, **Shalu, Pramila, Pramod Mane**, **Dr. Harimohan**, **Dr**. **Yogesh Madaria**, **Dr. Ankur Saxena**, **Swagat Dwivedi** and **Arun Ghidode** for giving me company and comments despite their busy schedules during tea breaks.

Cooperation and use of facilities extended by **Magod Fusion**, Pune for Stellite coating by Nd-YAG laser and **MM Machine Works,** Coimbatore for Stellite coating by PTA process are acknowledged. The research scholar is also very thankful to Sophisticated Instrumentation Center (SIC), Advanced Manufacturing Processes (AMP) Lab, Tribology Lab, Solid Mechanics Lab and Central Workshop of IIT Indore for allowing him to use their facilities in successful completion of his PhD thesis work. I am also thankful to Lab staff of Mechanical Engineering Labs and Central Workshop, specially **Mr. Anand Petare ASW, IIT Indore, Mr. Santosh Sharma Mr. Sandip Patil, Mr. Sandeep Gour, Mr. Deepak Rathore**, **Mr. Suresh Bhagore, Mr. Vinay Mishra, Mr. Hrishi, Mr. Pawan, Mr. Satish, Mr. Deepak, Mr. Umakant**, **Mr. Balkrishna** for their cooperation in fabrication of my experimental setup.

I acknowledge and thankful to **MHRD, Govt. of India** for providing fellowship to pursue my doctoral studies.

Last, but not least, I would like to dedicate this thesis to **my family** and **friends** for their love, patience, support and understanding. They allowed me to spend most of the time on my thesis, without which this journey would not have been possible**.**

Sawant Mayur Sudhakar

Dedicated

To my mother, father and sister, who taught me to learn. To my beloved wife Tejaswini and my two stars Shreeansh and Surya, who taught me to live and who brought the real joy in my life. To my all-in laws for their respect, love, patience and support in each step of my life. And of course, to my friends who inspires me all the time and have special place in social, professional and personal life. Goodbyes hurt more than anything especially when friends like Shivratna and Nilesh were deep down and when I know I won't be able to say "hello" again.

Extended Abstract

Additive manufacturing (AM) is a bottom-up approach based manufacturing philosophy in which a product is manufactured directly from its computer-aided design (CAD) model by depositing the material in thin successive layers in such a way that good mechanical properties, dimensional accuracy and surface finish are achieved along with sound metallurgical bonding between the deposited layers. AM processes are generally material-efficient because they incur a small loss of the product material than subtractive, primary accretion (i.e. casting, powder metallurgy), and deformative type manufacturing processes. Being material-efficient makes them energy saving and consequently environment friendly as well. They offer following worth-mentioning advantages over other processes: (i) ability to additively manufacture a part of complex geometry made of diverse materials such as polymer, composites or metallic materials; (ii) ability to economically repair damaged components or products which are very expensive, complex and require longer delivery time; (iii) ability and more flexibility to add delicate features to an existing component; (iv) ability to modify surfaces of a product by coating and/or texturing; (v) reduced design-to-market time and material procurement time and consequently reduced cost of the manufactured product (Nikam et al., 2016). Therefore, AM has generated a lot of research interest and industry expectations in the recent times. Some worth-mentioning applications of AM include rapid prototyping (RP), rapid tooling (RT), rapid manufacturing (RM) of an actual part, surface modification, surface coating, repairing and remanufacturing.

Type of energy source used in AM processes is one of the most important criteria distinguishing between them. Arc [such as gas tungsten arc (GTA) or plasma transferred arc (PTA)] and high-energy beam [such as laser or electron beam] are the commonly used heat source. Arc-based AM processes have some major advantages such as higher deposition efficiency, lower capital and maintenance costs but they yield poor deposition quality having higher dilution, porosity and oxides and are energy inefficient. High-energy beam-based AM processes have more focused and precisely controlled heat source than the arc-based AM processes. However, they suffer from major drawbacks such as poor energy conversion efficiency and higher capital cost, operating cost, and maintenance cost. Suryakumar et al. (2011) reported that the deposition rate achieved by high-energy beam-based AM processes is of the order of 2-10 g/min whereas arc-based AM processes can achieve it in the range of 50-130 g/min. Jhavar et al. (2014) developed micro-plasma wire

deposition (μ-PTAWD) process to bridge the gaps between capabilities of arc-based and high-energy beam-based AM processes. But, this process cannot be used for good quality deposition of those materials which are very difficult to be drawn in the form of wire (i.e. hard and/or brittle metals and alloys, refractory materials, ceramics, some composites, functionally graded materials). Moreover, use of deposition material in powdered form enables (i) attainment of higher deposition rate; (ii) better metallurgical bond between different deposition layers as well as deposition and the substrate materials; and (iii) better control over the deposition geometry. Therefore, this present work is aimed to develop an energy-efficient and cost-effective process referred to as micro-plasma transferred arc powder deposition (μ-PTAPD) process for various AM applications of the metallic materials with following research objectives:

- To develop experimental apparatus for μ-PTAPD process for various AM applications of the metallic materials with programming movement of the micro-plasma deposition head along x, y, and z axes by microcontroller.
- To study the characteristics of single-layer multi-track coating of Stellite powder on steel substrate by μ-PTAPD process.
- To compare the capabilities of μ-PTAPD process with laser and PTA-based processes for coating of Stellite.
- To study the characteristics of multi-layer single-track deposition of titanium alloy by μ-PTAPD process using continuous and dwell-time modes.
- To study the influence of dimple and spot texturing by μ-PTAPD process on HSS tool in machining of titanium alloy and to compare the performance of textured HSS tools with non-textured tool in terms of machining forces, temperature and wear of the tool, chip formation, and workpiece surface roughness.
- To develop a mathematical model of dilution of deposition by μ-PTAPD process.

1. Experimental Apparatus

Figures 1a and 1b show schematic diagram and photograph of the experimental apparatus respectively for μ-PTAPD process developed by integrating the following (i) micro-plasma power supply system capable of supplying constant value of DC voltage 22 volts and provision to vary current from 0.1 to 20 A with an increment of 0.1 A. It can supply power both in continuous and pulsed modes, (ii) in-house developed powder feeding system to ensure an uninterrupted supply of the deposition material in powdered form with particle size ranging from 20 to 200 μm. It consists of a hopper to store the powder which is supplied to the deposition head by means of pressurized argon supplied at constant flow rate of 0.5 Nl/min. Mass flow rate of the powder can be varied by changing rotation of a metering shaft driven by DC motor, (iii) in-house developed deposition head consisting of the μ-plasma torch surrounded by 4 equi-spaced inclined nozzles placed at its periphery. It also provides argon shielding-gas during the deposition process to protect the molten pool against oxidation, and (iv) arduino based microcontroller to control movement of the deposition head along X, Y and Z axes.

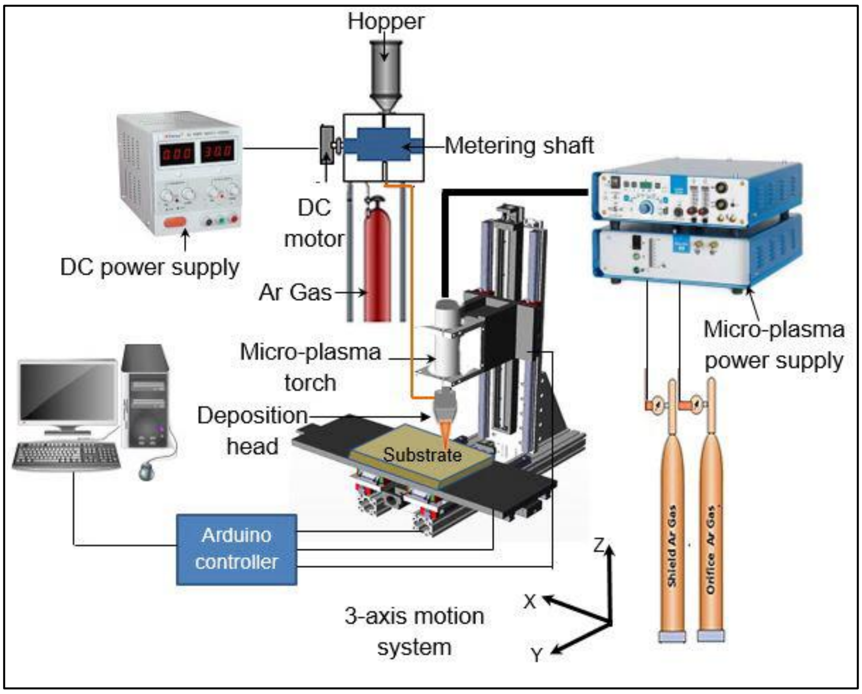

(a)

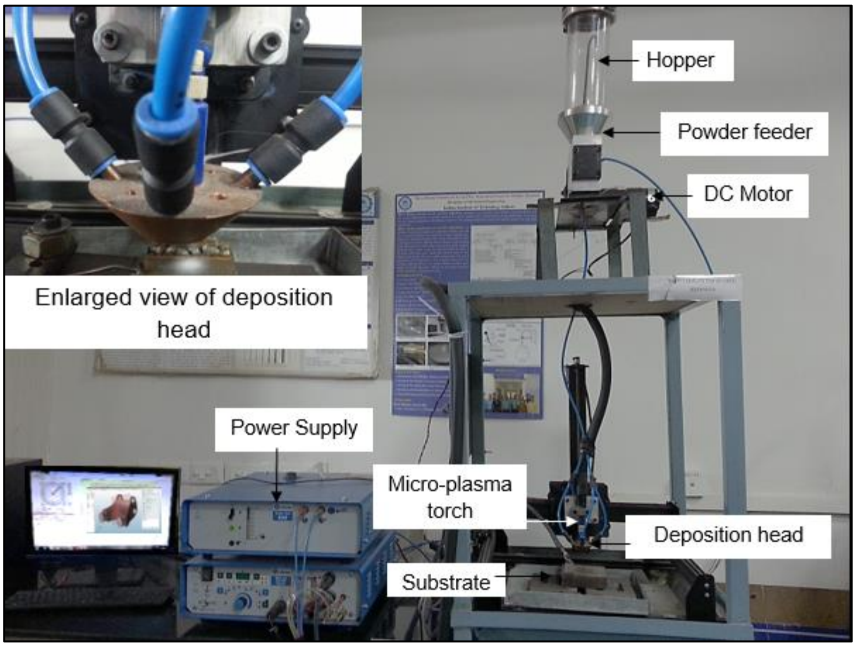

(b)

Fig. 1: (a) Schematic view and (b) photograph of the experimental apparatus developed for μ-PTAPD process.

2. Study on Coating of Stellite 6 on AISI 4130 Steel Substrate

Coatings play significant roles to improve performance and life of those parts which operate in adverse environments and require resistance to different types of wear such as fretting, surface fatigue, corrosion, erosion, abrasion, adhesion, and diffusion. Stellite is a cobalt-based alloy which exhibits very good resistance to erosive and corrosive wear particularly, at higher operating temperature due to intermetallic compounds and carbides formed in its coating (Luo et al., 2012). The experiments were conducted in four stages with objectives to (i) identify optimum values of important parameters of μ-PTAPD process for single-layer multi-track coating of powdered Stellite 6 (with particle size ranging from 50 to 106 μm) on AISI 4130 steel substrate; and (ii) to compare its capabilities with laser-based and PTA-based deposition processes for Stellite coating in terms of dilution, deposition thickness, microstructure, secondary dendritic arm spacing (SDAS), micro-hardness and abrasive wear resistance. In the 1st stage, pilot experiments were conducted varying six significant parameters of μ-PTAPD process namely micro-plasma power, travel speed of worktable, powder mass flow rate, shielding gas flow rate, plasma gas flow rate and stand-off distance to identify their values for the main experiments which will ensure continuous uniform single-layer single-track deposition of Stellite. The identified values for the main experiments were: 407; 418; and 429 W for micro-plasma power, 80; 100; and 125 mm/min for travel speed of worktable, 1.7; 2.9; and 3.5 g/min for powder mass flow rate, 3.5 normal liter per minute for shielding gas flow rate, 0.3 normal liter per minute for plasma gas flow rate and 8 mm for stand-off distance. Twenty-seven main experiments were performed in the 2nd stage to identify optimum values of micro-plasma power (as 407 W), travel speed of worktable (as 125 mm/min), powder mass flow rate (as 3.5 g/min) to ensure minimum energy consumption and dilution of single-layer single-track deposition of Stellite by μ-PTAPD process. Four experiments were conducted in the 3rd stage using 10%; 20%; 30%; and 40% overlapping between two successive tracks and using the identified optimum values from the main experiments in single-layer multi-track deposition of Stellite to identify optimum value of overlapping considering minimum dilution and maximum deposition height as selection criteria. These experiments found 30% overlapping as the optimum value. These identified optimum values were used in the 4th stage experimentation to compare the considered characteristics of single-layer multi-track coatings of Stellite manufactured by μ-PTAPD, Nd-YAG laser-based, and PTA-based deposition processes. The parameters used in Nd-YAG laser-based deposition included: power: 2 kW, spot size: 4 mm, travel speed: 480

mm/min, and powder mass flow rate: 11 g/min. The parameters used in PTA-based deposition were: current: 95 A, voltage: 22.5 V, travel speed: 180 mm/min, powder mass flow rate: 21 g/min; plasma gas (argon) flow rate: 2.1 Nl/min, and shielding (argon) gas flow rate: 2.5 Nl/min.

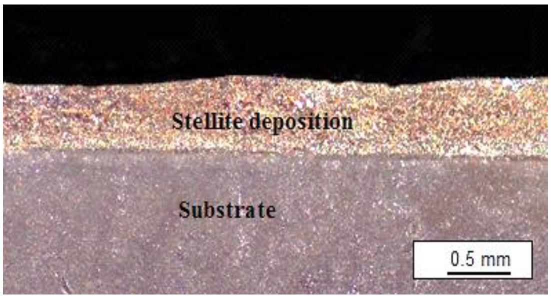

(a)

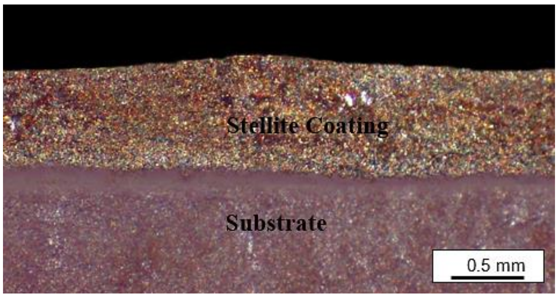

(b)

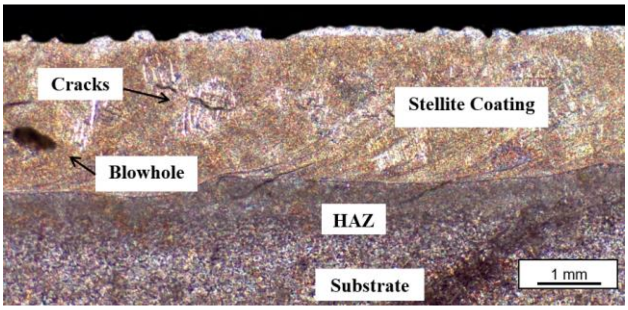

(c)

Fig. 2: Optical micrographs showing cross-section of the coatings of Stellite-6 manufactured by (a) µ-PTAPD; (b) laser deposition; and (c) PTAD processes.

Table 1: Mean values of SDAS, cooling rate, dilution and coating thickness for different processes of Stellite coating.

Stellite coating process	SDAS ‘λ’ (µm)	Cooling rate ‘R’ (°C/s)	Dilution (%)	Coating thickness (mm)
µ-PTAPD	1.74	6.69×10^3	6.3	0.7
Laser deposition	1.72	6.93×10^3	5.8	0.9
PTAD	6.79	1.12×10^2	21.5	2.6

2.1 Some Significant Results

- The optical images of the Stellite coatings by µ-PTAPD (Fig. 2a) and laser-based (Fig. 2b) deposition processes reveal that they have good surface appearance, smaller HAZ, excellent metallurgical bond with the substrate and are free from the defects such as cracks and porosity. In contrast, optical image of the Stellite coating by PTAD process (Figure 2c) shows presence of blowholes and cracks which may be due to trapped gasses and varying contraction during the solidification. It also indicates larger HAZ which is caused by more amount of heat used in PTAD process.

- It can be observed from Table 1 that µ-PTAPD and laser-based deposition processes are capable of manufacturing coatings of thickness less than 1 mm with lower dilution, finer dendritic structure, and smaller SDAS value than the coating manufactured by PTAD. Smaller SDAS result in finer dendritic structure due to higher cooling rate in µ-PTAPD (6.69×10^3 °C/s) and laser deposition (6.93×10^3 °C/s) processes.
- Phase analysis of Stellite coatings manufactured by all three processes by XRD revealed presence of ε-Co having HCP crystal structure and α-Co having FCC crystal structure mixed with chromium-rich carbides ($C_{r23}C_6$, $C_{r7}C_3$), and tungsten containing complex carbide (W_2C). These carbides are responsible for higher hardness and wear resistance of Stellite coating.
- Evaluation of micro-hardness profile revealed that Stellite coating by µ-PTAPD and laser-based deposition processes had almost similar micro-hardness i.e. 553 and 551 HV respectively which is much higher than the coating manufactured by PTAD process (501 HV). This is due to higher cooling rates in µ-PTAPD and laser-based deposition which result in formation of finer carbides which impart higher micro-hardness whereas, lower cooling rate in PTAD process (i.e. 1.12×10^2 °C/s) results in formation of a coarser carbides and higher heat input results in higher dilution (i.e. 21.5%).
- Coatings manufactured by laser-based and µ-PTAPD processes showed lower wear volume than the coating manufactured by PTAD process for all the values of sliding distance (Fig. 3) due to formation of finer carbides, lower dilution and higher micro-hardness of Stellite coatings. Wear volume of PTAD manufactured coating increases drastically after 400 m sliding distance due to extensive ploughing of the coating.

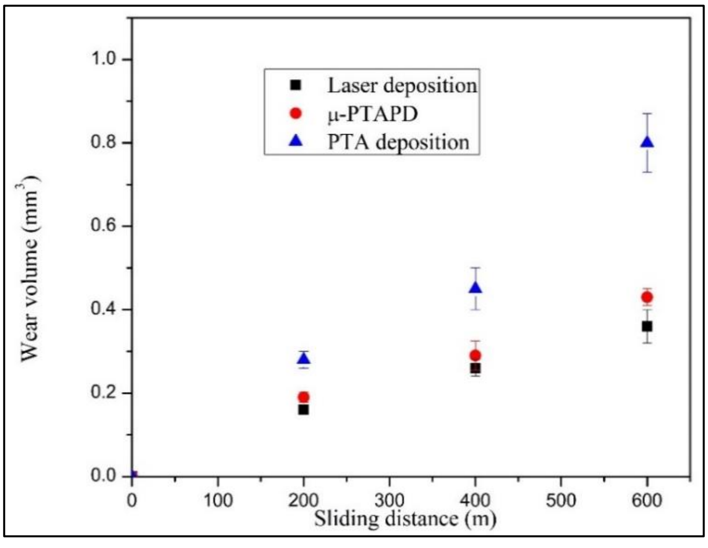

Fig. 3: Variation of wear volume with the sliding distance for the coatings of Stellite 6 manufactured by µ-PTAPD, laser deposition and PTAD processes.

3. Study on Multi-layer Single-track Deposition of Ti-6Al-4V

Higher strength-to-weight ratio, fracture toughness and excellent biocompatibility and corrosion resistance of titanium and its alloys have led to their extensive and varied applications in biomedical, aerospace, power generation, gas turbines, automotive etc. (Mahamood and Akinlabi, 2017). The experimental study was conducted in three stages to (i) identify optimum values of six influential parameters of μ-PTAPD process (i.e. micro-plasma power, travel speed of deposition head, powder mass flow rate, shielding gas flow rate, plasma gas flow rate and stand-off distance) for multi-layer single-track deposition of Ti-6Al-4V on the substrate of same material; and (ii) study their effects on deposition characteristics, tensile properties, microstructure evolution, microhardness, and wear characteristics. Pilot experiments were conducted in the 1st stage to identify those feasible values of six considered parameters of μ-PTAPD process for the main experiments which will ensure continuous single-layer single-track deposition of Ti-6Al-4V powder on the substrate of same material. The identified values for the main experiments were: 418; 429; and 440 W for micro-plasma power, 52; 57; and 62 mm/min for travel speed of the deposition head, 1.5; 2.1; and 2.7 g/min for powder mass flow rate, 5 Nl/min for shielding gas (i.e. argon) flow rate, 0.3 Nl/min for plasma gas (i.e. argon) flow rate and 10 mm for stand-off-distance. Twenty-seven main experiments were conducted in the 2nd stage by varying micro-plasma power, powder mass flow rate and travel speed of the deposition head to identify their optimum values considering minimum energy consumption aspects. Identified optimum values were: micro-plasma power as 418 W; powder mass flow rate as 2.7 g/min; and travel speed of deposition head as 62 mm/min. In the 3rd stage of experimentation, thin wall structures of Ti-6Al-4V were made by moving the deposition head in following two ways for its multi-layer single-track deposition by μ-PTAPD process using the optimum values of the six parameters identified from the main experiments: (i) **continuous deposition:** depositing the successive layers both in forward and backward direction movement of the deposition head; and (ii) **dwell-time deposition:** depositing the successive layers only in the forward direction movement of the deposition head only when the previously deposited layer cools down to 100^{o}C with temperature being monitored by an infrared pyrometer.

3.1 Some Significant Results

- Dwell-time deposition of Ti-6Al-4V yielded lower total wall width (3.73 mm) and higher effective wall width (3.51 mm) than that by continuous deposition (4.1 mm and 3.32 mm, respectively). This led to higher deposition efficiency (89.5%) and lower deposition waviness (0.11 mm) of dwell-time deposition than that given by continuous deposition (i.e. 77.2% and 0.39 mm, respectively). This implies that a component manufactured using continuous deposition will require more amount of finishing which will increase cost and wastage of the deposition material.

- Optical micrograph of the continuous deposition of Ti-6Al-4V (Fig. 4a) shows inter-layer cracks and voids formed due to non-uniform thermal expansion during the solidification process. It indicates weak bonding between different deposition layers as well as the deposition and substrate because continuous deposition produces higher heat which causes higher thermal gradient between the deposition and substrate materials. In contrast, dwell-time deposition of Ti-6Al-4V (Fig. 4b) depicts that there is no inter-layer cracks and voids and has very good metallurgical bonding between different deposition layers as well as between the deposition and substrate.
- SEM image of the continuous deposition (Fig. 5a) shows coarse grained microstructure having colonies of lamellar α and β phases of titanium placed within the boundaries of the big grains. This is due to slowing down of the solidification process by higher heat content in continuous depositions of Ti-6Al-4V which causes larger melt pool. When the molten material is cooled at sufficiently slow rates from the β-phase into the α-β phase region then α-phase lamellae nucleate preferentially at β grain boundaries leading to continuous α-layer along β-grain boundaries. These α-lamellae continue to grow until they reach to other α-colonies nucleated at other grain boundaries. The individual α-lamellae are separated within α-colonies by the retained β-matrix. SEM image of the dwell-time deposition (Fig. 5b) depicts basket-weave fine microstructure which is generally produced by faster cooling rate from β-transition temperature which reduces both α-lamellae thickness and α-colony size. Additionally, new α-lamellae nucleated at other grain boundaries grow perpendicularly to the existing lamellae. This leads to formation of the basket-weave microstructure.
- Measurement of the lamellae width from the microstructures revealed that both continuous and dwell-time depositions of Ti-6Al-4V have smaller lamellae widths in the top portion of the deposition than that in the bottom portion. Lamellae widths of dwell-time deposition are smaller than that of continuous deposition. This is due to faster cooling rate in dwell-time deposition.
- Evaluation of the tensile properties showed that dwell-time deposition of Ti-6Al-4V has higher yield and ultimate strength, and lower % elongation (i.e. 890 MPa; 930.3 MPa;

and 13.2%, respectively) than that for the continuous deposition (i.e. 754 MPa; 788 MPa; and 18.2%, respectively). Examination of the fractured tensile specimen of dwell-time deposition showed fine dimple rupture while that of continuous deposition exhibited occurrence of tear ridges or elongated regions.

- Dwell-time deposition of Ti-6Al-4V had higher microhardness than continuous deposition due to fine basket-weave microstructure.
- Dwell-time deposition showed lower wear volume and coefficient of friction than that of continuous deposition.

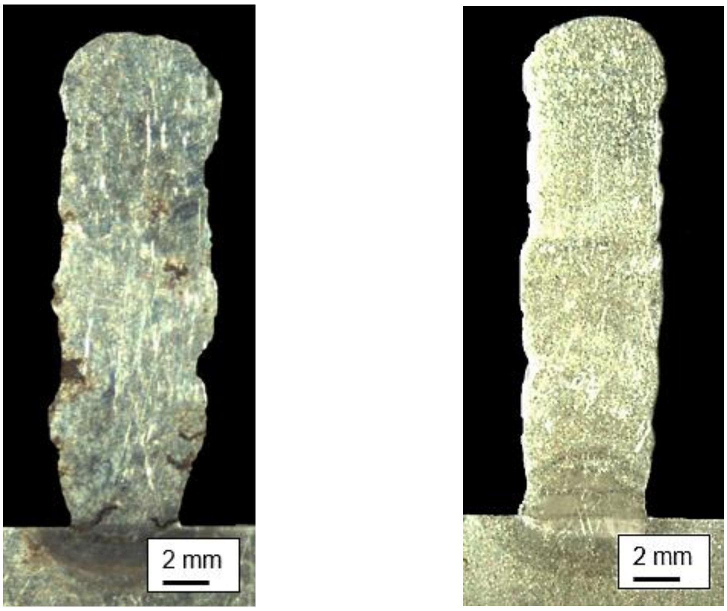

(a) **(b)**

Fig. 4: Optical micrograph of cross-section of the (a) continuous deposition; and (b) dwell-time deposition of Ti-6Al-4V.

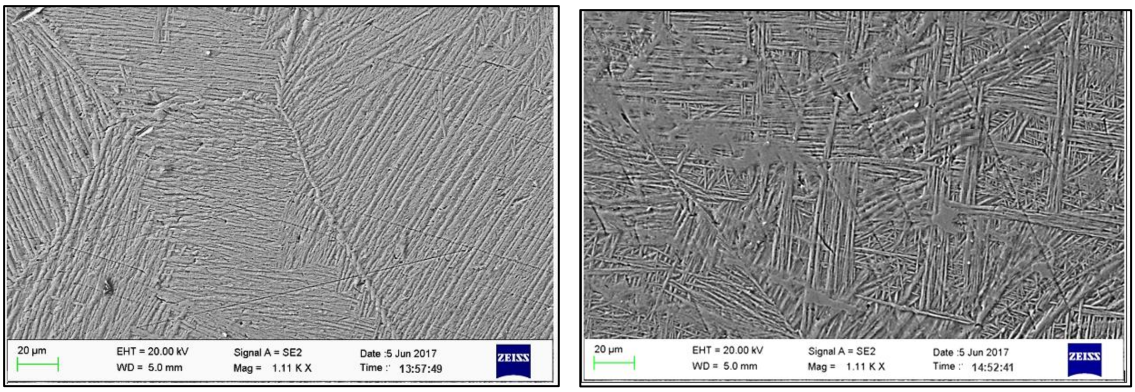

(a) **(b)**

Fig. 5: SEM images showing microstructure of the (a) continuous deposition; and (b) dwell-time deposition of Ti-6Al-4V.

4. Study on Texturing of HSS Tool to Improve Machining of Titanium Alloys

Machining of titanium alloys using high speed steel (HSS) tool is difficult due to their lower thermal conductivity which increases the temperature of the machining tool thus accelerating its wear. Texturing on rake face of a machining tool has recently emerged as a promising and environment friendly method to enhance removal of heat from the machining zone (Wei et al., 2017). Therefore, investigations were conducted to study influence of spot and dimple texturing by μ-PTAPD process on the rake face of a single-point machining tool made of HSS in machining of Ti-6Al-4V alloy. It was done in the following four stages: (i) In the 1st stage, pilot experiments creating single texture on shank of the HSS machining tool to identify feasible values of the variable parameters of μ-PTAPD process (i.e. micro-plasma power and exposure time for the dimple-texturing, and micro-plasma power, exposure time and powder flow rate of Stellite 6 for the spot-texturing,). The identified values for the main experiments were: 246.4; 264; and 281.6 W of micro-plasma power and 15; 30; and 45 s values of exposure time for the dimple-texturing and 264; 286; and 316 W for micro-plasma power; 6; 10; and 14 s for exposure time, 1.45; 1.76; and 2.10 g/min for powder flow rate for the spot-texturing; (ii) Nine main experiments, creating single texture in each experiment, were conducted in the 2nd stage by varying identified values from the pilot experiment and used to identify optimum values for dimple and spot texturing considering maximum aspect ratio and dilution respectively; (iii) In the 3rd stage, an array of 12 textures on rake face of the HSS machining tool were produced using the identified optimum values of the considered variable parameters. The spot-textured HSS tool was ground to make uniform size of the spots; and (iv) In the 4th stage, performance of the dimple-textured, spot-textured and non-textured HSS machining tools were compared in terms of machining forces, temperature and flank wear of the tool, chip formation, and surface roughness of the machined workpiece during turning of the Ti-6Al-4V cylindrical bar under flooded type coolant system. Other parameters selected for turning of Ti-6Al-4V bar were: 45 and 105 m/min as cutting speed; 0.1 mm/revolution as feed rate; and 1 mm as depth of cut (da Silva et al. 2013). Micro-plasma power as 264 W and exposure time as 45 seconds were identified as optimum values to obtain dimple-texture with high aspect ratio and approximately circular shape. They were used for producing an array of dimple texture on the rake face of the HSS machining tool and its optical image and photograph shown in Figs. 6a and 6b. Micro-plasma power as 316 W; exposure time as 14 seconds; and powder flow rate as 1.76 g/minute were identified as optimum values to achieve approximately sphere-shaped spot-textures having high dilution ratio and minimum unmolten particles attached. These values were used to produce an array of spot-textures on the rake face of the HSS tool and its optical image and photograph shown in Figs. 7a and 7b.

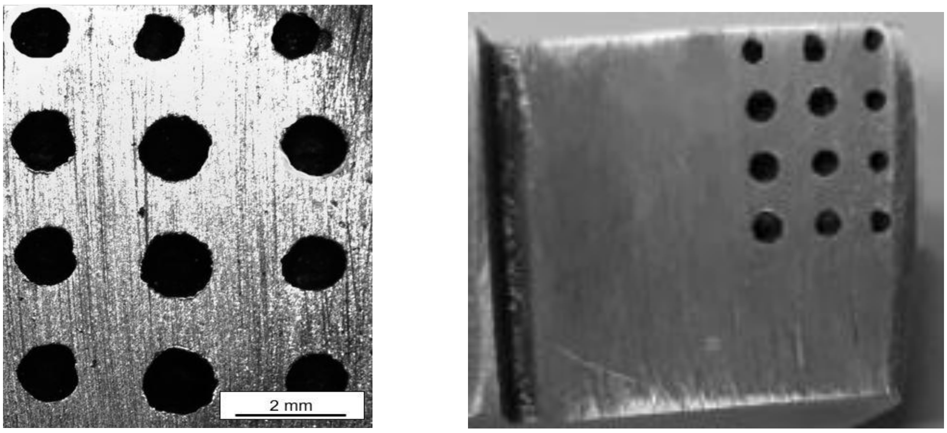

(a) **(b)**

Fig. 6: Array of dimple textures produced by µ-PTAPD process on rake face of the HSS tool: (a) optical image and; (b) photograph.

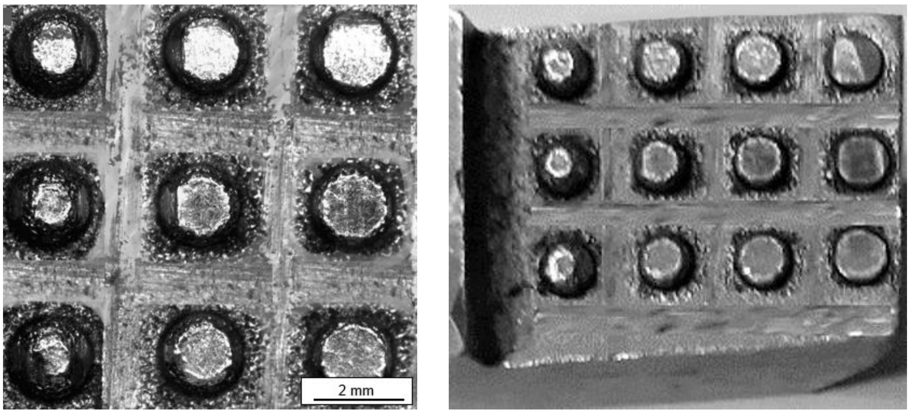

(a) **(b)**

Fig. 7: Array of the spot textures produced by µ-PTAPD process on rake face of the HSS tool: (a) optical image and; (b) photograph.

4.1 Some Significant Results

- Use of spot-textured HSS tool in turning of Ti-6Al-4V resulted in least values of cutting force, thrust force, and tool temperature than the dimple-textured and non-textured HSS tools at different values of cutting speed. These observations can be explained with the help of Fig. 8 which schematically shows how flow of chips over the spot-textured HSS tool increases rake angle and reduces chip curl radius. Increase in rake angle reduces the cutting force whereas reduction in the chip curl radius helps in chip breaking which aids in reduction of thrust force. Additionally, spots act as fins which enhances the heat loss to the machining environment by increasing surface area of the rake face of the spot-textured tool thus helping in further reduction of its temperature.

- Spot-textured tool exhibits least amount of flank wear and adhesion of workpiece material than the dimple-textured and non-textured tools. This is due to higher temperature of the dimple-textured and non-textured tools which increases their sticking tendency for products of machining causing more adhesive wear of their flank surface. Higher temperature also reduces their hardness resulting in further wear of their flank surfaces.
- Use of spot-textured tool resulted in formation of segmented chips in turning of Ti-6Al-4V whereas dimple-textured and non-textured tools formed long continuously curling ribbon-like chips.
- Average surface roughness of the turned Ti-6Al-4V workpiece revealed that spot-textured HSS tool yielded minimum values of average surface roughness 'R_a' of the turned Ti-6Al-4V workpiece than the dimple-textured and non-textured HSS tools at both the cutting speeds. This is due to spot-textured tool having lesser temperature rise and flank wear which results in better surface finish.

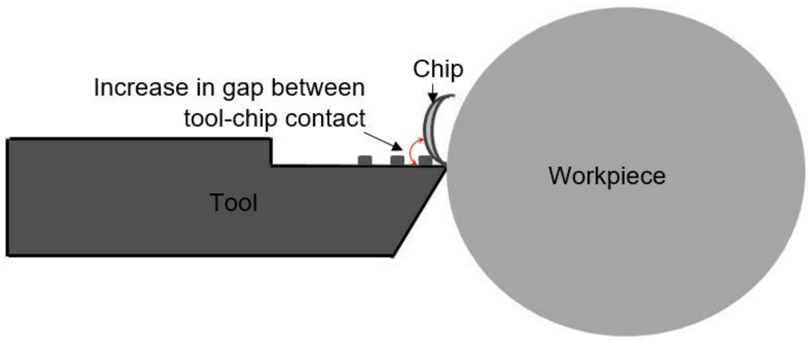

Fig. 8: Schematic of chip flow over the rake face of spot-textured tool during turning of Ti-6Al-4V.

5. Mathematical Modeling of Dilution

Following mathematical model of dilution of single-layer single-track deposition as function of µ-PTAPD process parameters and materials properties was developed using the fundamental principles of energy balance.

$$D = \left(1 + \frac{\eta_d \, V_d \, \rho_s \, \Delta H_s}{(\eta_a \, \eta_m \, P \, t) - (\eta_d \, V_d \, \rho_d \, \Delta H_d)}\right)^{-1} \times 100 \qquad (1)$$

- where, ΔH_d and ΔH_s are change in enthalpies of the deposition and substrate material respectively (J/kg); ρ_d and ρ_s are densities of the deposition and substrate material respectively (kg/m^3); P is micro-plasma power (Watts); V_d is volume of deposited powder (m^3); t is deposition time; η_a is energy transfer efficiency (%)and η_m is melting efficiency (%). The developed mathematical model for dilution of single-layer single-track deposition was experimentally validated depositing Ti-6Al-4V powder on substrate of the same material and depositing Stellite powder on AISI 4130 steel substrate by µ-PTAPD process. The error between the predicted and experimental dilution for Ti-6Al-4V deposition on the same substrate and Stellite 6 deposition on AISI 4130 is in range from -16 to 6.41 % and -16.85 to 14.30 % respectively.

6. Some Significant Conclusions

- µ-PTAPD process has a capability to selectively deposit a thin and sound quality coating of Stellite on metallic substrates. It has capability to provide better techno-economic solution than the existing processes for Stellite coating.
- Multi-layer single-track of deposition of Ti-6Al-4V alloy by µ-PTAPD process using dwell-time mode having better deposition characteristics, fine basket-weave microstructure, tensile properties, higher microhardness and lower wear volume and coefficient of friction. It demonstrates that µ-PTAPD process has capability to additively manufacture complex part geometry of titanium alloys.
- Spot-texturing of rake face of HSS machining tool by µ-PTAPD process is an economical, effective and environment friendly method to improve machining of titanium alloys.
- µ-PTAPD process is a very promising process for different additive manufacturing applications of metallic materials. It can be used for similar as well as dissimilar deposition and substrate materials.

Keywords: Additive manufacturing; Micro-plasma; Powder deposition; Stellite coating; Ti-6Al-4V; Texturing.

List of Publications

(A) Publications from PhD Thesis

(A.1) Papers in Refereed Journals

1. **Mayur S Sawant**, N.K. Jain, I.A. Palani **(2018)** "Influence of dimple and spot-texturing of HSS cutting tool on machining of Ti-6Al-4V" **Journal of Materials Processing Technology,** 261, 1–11 (Nov. 2018) (doi: 10.1016/j.jmatprotec.2018.05.032) (**Impact factor: 3.65)**
2. **Mayur S Sawant,** N.K. Jain **(2018) "**Investigations on additive manufacturing of Ti-6Al-4V by µ-plasma transferred arc powder deposition process" **Transactions of ASME: Journal of Manufacturing Science and Engineering**, 140, (Aug. 2018), p. 081014-10-81014-11 (11 pages), doi: 10.1115/1.4040324 **(Impact factor: 2.58)** (online since 19 May 2018)
3. **Mayur S Sawant**, N.K. Jain **(2018)** "Evaluation of Stellite coatings by µ-PTA powder, laser and PTA deposition processes" **Materials and Manufacturing Processes,** 33(10), 1043-1050 (27 July 2018), doi: 10.1080/10426914.2017.1364764 (online since 10 Aug 2017) (**Impact Factor: 2.67**)
4. **Mayur S Sawant,** N.K. Jain **(2017)** "Characteristics of single-track and multi-track depositions of Stellite by micro-plasma transferred arc powder deposition process" **Journal of Materials Engineering and Performance**, 26(8), 4029-4039 (July 2017) (doi: 10.1007/s11665-017-2828-y) **(Impact Factor: 1.34)**
5. **Mayur S Sawant,** N.K. Jain **(2017)** "Investigations on wear characteristics of Stellite coating by micro-plasma transferred arc powder deposition process" **Wear,** 378-379, 155-164 (May 2017) (doi: 10.1016/j.wear.2017.02.041) (**Impact factor: 2.96)**.

(A.2) Book Chapter

6. Neelesh Kumar Jain, **Mayur S Sawant,** Sagar H Nikam, S Jhavar (2016), **"Metal Deposition: Plasma-Based Processes"** in *Encyclopaedia of Plasma Technology* (Editor: J. Leon Shohet), CRC Press, pp. 722-740, eBook ISBN: 978-1-4822-1431-4 (doi: 10.1081/E-EPLT-120053919). http://www.crcnetbase.com/doi/10.1081/E-EPLT-120053919

Table of Contents

List of Figures

List of Tables

Nomenclature

A	Diluted area (mm^2)
B	Deposited area (mm^2)
D	Dilution (%)
E_l	Energy consumption per unit traverse length (J/mm)
f_v	Volumetric feed rate of the deposition material (m^3/s)
F_p	Plasma gas flow rate (Nl/min)
F_s	Shielding gas flow rate (Nl/min)
f	Powder mass flow rate (g/min)
H	Deposition height (mm)
l	Length of deposition (m)
P_f	Power consumption per unit powder mass flow rate (J/g)
P	Micro-plasma power (W)
R	Cooling rate ($^oC/s$)
R_a	Average surface roughness
T	Relative speed between the deposition head and the substrate material (mm/min)
t	Deposition time (second)
W	Deposition width (mm)
W_t	Combined weight of the deposition and the substrate material (g)
W_s	Weight of the substrate material (g)
W_p	Weight of deposition material delivered to the melt pool (g)
X	Stand-off-distance (mm)
η_a	Energy transfer efficiency (%)
η_m	Melting efficiency (%)
η_d	Deposition efficiency (%)
ΔH_d	Change in enthalpies of the deposition material (J/kg)
ΔH_s	Change in enthalpies of the substrate material (J/kg)
ρ_d	Densities of the deposition material (kg/m^3)
ρ_s	Densities of the substrate material (kg/m^3)
V_d	Volume of the deposited material (m^3)
λ	Secondary dendritic arm spacing (μm)
α_s	Thermal diffusivity of the substrate material (m^2/s)

Abbreviations

AM	Additive manufacturing
CAD	Computer-aided design
CNC	Computer numerical controlled
CAM	Computer-aided manufacturing
DE	Deposition efficiency
DMLS	Direct metal laser sintering
DW	Deposition waviness
EWW	Effective wall width
EBM	Electron beam melting
EDX	Energy dispersive x-ray spectroscopy
FCC	Face centred cubic
FGM	Functionally graded materials
GMAD	Gas metal arc deposition process
GTAW	Gas tungsten arc welding
HAZ	Heat affected zone
HCP	Hexagonal close-packed
HSS	High speed steel
HVOF	High velocity oxygen fuel
LC	Laser cladding
LENS	Laser engineering net shaping
MAG	Metal active gas
MIG	Metal inert gas
MMC	Metal matrix composites
μ-PTA	Micro-plasma transferred arc
μ-PTAPD	Micro-plasma transferred arc powder deposition
μ-PTAWD	Micro-plasma transferred arc wire deposition
PTAD	Plasma transferred arc deposition
PPTA	Pulsed plasma transferred arc
FE-SEM	Field emission scanning electron microscopy
SDAS	Secondary dendrite arm spacing
SLM	Selective laser melting
SLS	Selective laser sintering

SD	Standard deviations
SLD	Supersonic laser deposition
TWW	Total wall width
WC	Tungsten carbide
TIG	Tungsten inert gas
WEDM	Wire electric discharge machining
XRD	X-ray diffraction

Chapter 1

Introduction

Manufacturing industries constantly face challenges to deliver good quality products with maximum possible features at the lowest possible price to meet the customer demands. This has led to the development of the advanced materials and technologies for reducing design and manufacturing lead time. The advanced materials possess useful unique properties such as very high strength and stiffness at elevated temperatures, extreme hardness and brittleness, high strength to weight ratio, very good oxidation and corrosion resistance, chemical inertness, etc. Shaping or processing of these materials is very difficult using a conventional manufacturing process. Therefore, manufacturing industries always look for near net-shape, productive and sustainable manufacturing technology particularly for the products made of the advanced materials and/or products having very complicated geometry. This is achieved by focusing use of new tools, methods and new form of energy sources. In this context, additive manufacturing (AM) has generated a lot of industry expectations and research interest in the recent times.

1.1 Concept of Additive Manufacturing

AM is a bottom-up approach based manufacturing philosophy in which a product is manufactured directly from its computer-aided design (CAD) model by depositing the material in thin successive layers as shown in Fig. 1.1. This unique feature allows production of a complex or customized part directly from the design of CAD model without use of expensive tooling. AM processes are generally material-efficient because they incur a small loss of the product material than subtractive, primary accretion (i.e. casting, powder metallurgy), and deformative type manufacturing processes. Being material-efficient makes them energy saving and consequently environment friendly as well (Jhavar et al., 2014). The bonding strength between the different deposition layers as well as the between deposition and the substrate materials varies according to the deposition energy, deposition volume, deposition pattern and the interaction time between the deposition and substrate material. AM can be used to fabricate parts made of metals, alloys, polymers, ceramics, composites and functionally graded materials (FGM). Some worth-mentioning applications include biomedical (i.e. implants and prosthesis), aerospace, power generation, gas turbines, automotive, marine, sports, oil and gas extraction, digital cameras, mobile phones (Edwards et al., 2013). There are many common synonyms used to describe AM include: additive fabrication (AF), additive layer manufacturing (ALM), direct digital manufacturing (DDM), and solid freeform fabrication (SFF).

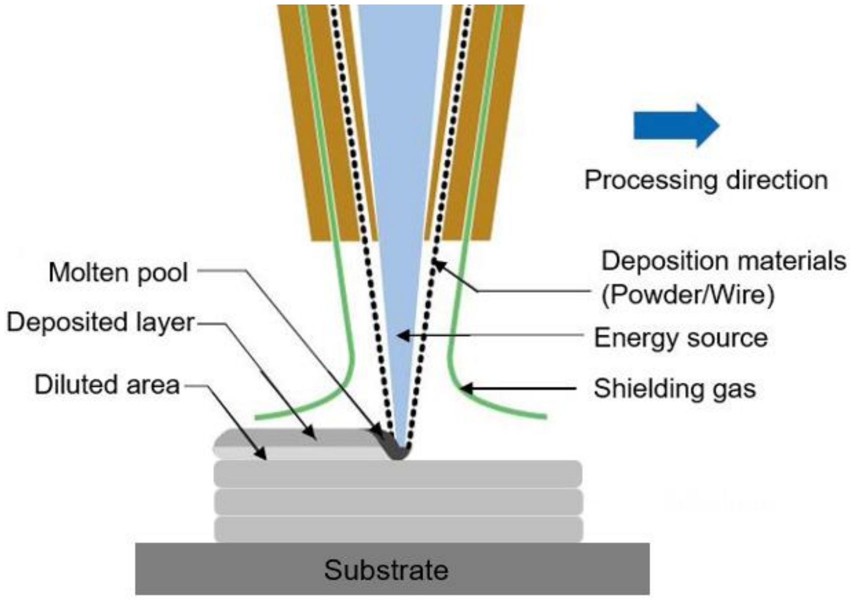

Fig. 1.1: Schematic of a typical additive manufacturing process.

1.2 Advantages of Additive Manufacturing

Additive manufacturing offer following worth-mentioning advantages over other processes: (i) ability to additively manufacture a complex geometry part made of diverse materials such as polymer, composites or metallic materials, (ii) ability to economically repair the damaged components or products which are very expensive, complex and require longer delivery time, (iii) ability and more flexibility to add delicate features to an existing component, (iv) ability to modify surfaces of a product by coating and/or texturing, (v) reduces design-to-market time, material procurement time, intermittent quality checks, human errors, and planning of man power, machines and manufacturing processes, (vi) AM reduces cost of the manufactured product (Nikam et al., 2016).

1.3 Concept of Layer and Track in Additive Manufacturing

Fig 1.2 presents the concept of deposition of layer and track used in AM process. Following different combinations of layer and track are used for different applications of an AM process: (i) *single-layer single-track* (Fig 1.2a) deposition which is typically used for repairing/remanufacturing applications, (ii) *single-layer multi-track* (Fig 1.2b) deposition in which tracks are deposited with some overlap to cover the entire top surface of the substrate material. It is typically used for various coating applications, (iii) *multi-layer single-track* (Fig 1.2c) deposition in which layers are deposited successively to achieve the desired deposition height. It is typically used in manufacturing of thin walled complex geometries, and (iv) *multi-layer multi-track* (Fig 1.2d) deposition in which layers are deposited along the width and height of substrate to achieve the desired deposition width and deposition height of complex geometries typically used in cladding applications and in manufacturing of thick walled complex geometries. For multi-layer depositions (Figs. 1.1c and 1.1d) the previously deposited layer becomes the substrate for deposition of next layer except deposition of very first layer.

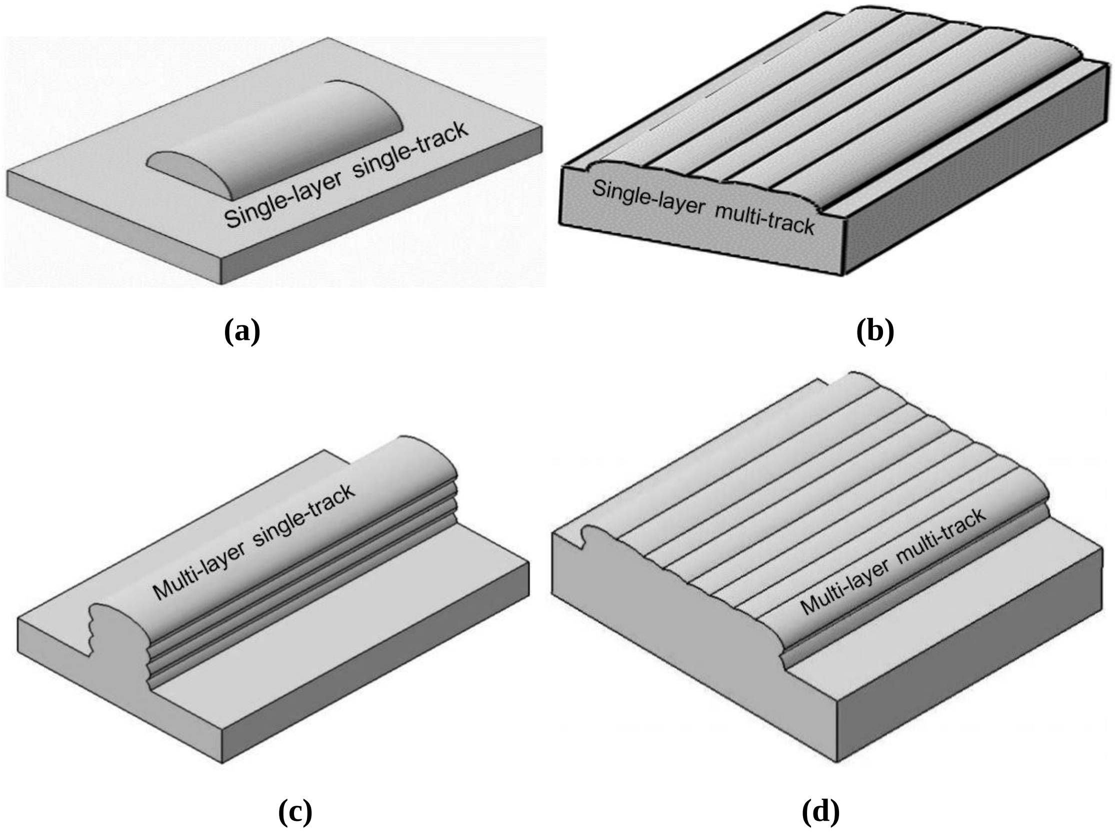

Fig. 1.2: Concept of deposition of layer and track used in an AM process: (a) single-layer single-track deposition; (b) single-layer multi-track; (c) multi-layer single-track deposition; and (d) multi-layer multi-track deposition.

1.4 Applications of Additive Manufacturing

Initially, concept of AM was used for manufacturing model and prototype of the parts. Recently, development of AM has been focussed on manufacturing of free-form surfaces/geometry of the metallic components. Various applications of AM include rapid prototyping, rapid manufacturing, rapid tooling, repairing and surface modification.

1.4.1 Rapid Prototyping

Rapid Prototyping is the fast-emerging application of AM to quickly manufacture layer-by-layer a near-net shaped scaled prototype of a component, assembly or structure of an existing product or a newly designed product from the CAD data for the purpose of visualization, realization or evaluation. Rapid Prototyping models (Fig. 1.3) are also used for replication of the product behaviour under actual service conditions and functional testing (Gurr and Mülhaupt, 2016).

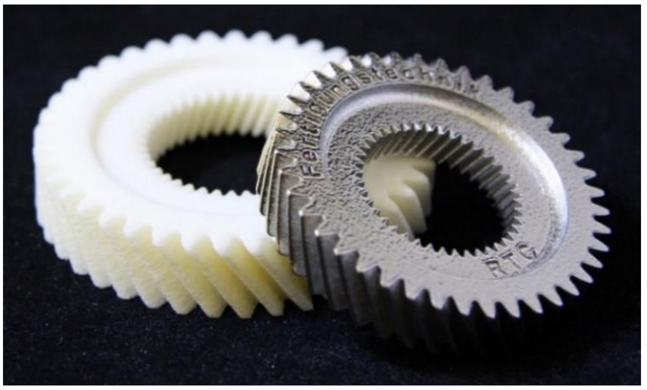

Fig. 1.3: Photograph of replica of a helical gear manufactured by rapid prototyping (Astcad, 2015).

1.4.2 Rapid Manufacturing

Rapid Manufacturing is a new area of manufacturing which is developed from a rapid prototyping process. Rapid manufacturing uses the CAD-based automated additive manufacturing process to construct real life products or components. It can be used for manufacturing of fully functional, long-term end-use products, add delicate features to an existing component and enables the creation of complex products with internal features to increase functionality. Rapid manufacturing has been developed to shorten the design and production cycle and promise to revolutionize many traditional manufacturing procedures. Rapid manufacturing includes major applications in direct parts manufacturing of components required in automotive, aerospace, household appliances and biomedical applications (Han, 2017). Fig. 1.4 shows photograph of a turbine blade of jet engine manufactured by rapid manufacturing

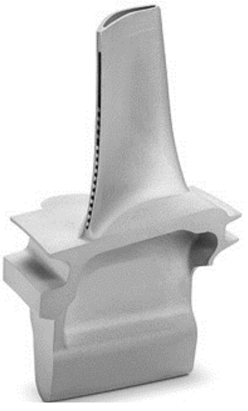

Fig. 1.4: Photograph of a turbine blade of jet engine manufactured by rapid manufacturing (Han, 2017).

1.4.3 Rapid Tooling

Rapid tooling is the fast fabrication of the different tools or dies or moulds for different manufacturing processes such as casting, sheet metal forming (Fig.1.5), injection moulding, electric discharge machining (EDM), electro chemical machining (ECM) process, etc. using a CAD-based automated additive manufacturing. These tools or dies can be used to produce a small quantity of prototypes, samples for marketing, and initial functional testing. Production of parts using rapid tooling ensures shorter production time as compared to that of a conventional tool manufacturing (Afonso et al., 2017).

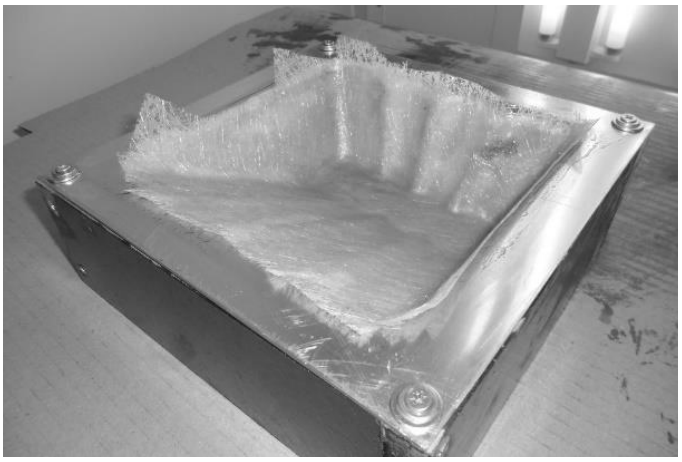

Fig. 1.5: Photograph of rapid sheet metal tool (Afonso et al., 2017).

1.4.4 Repairing

Engineering components such as dies, moulds, and gears are frequently subjected to local impacts, thermal stresses, corrosion, erosion, fatigue and other severe work environment during their service life. It results in the development of various defects before completion of their expected service life and adversely affect their service performance. Types of damages include various types of cracks, plastically deformed geometries, deteriorated edges, heat checks, dents as shown in Fig. 1.6. It is highly uneconomical to reject such components with minor defects much before their service life. AM is a cost-effective, material-efficient, wastage and inventory reducing, and replacement lead time saving option by economically repairing the damaged parts. (Jhavar et al., 2013).

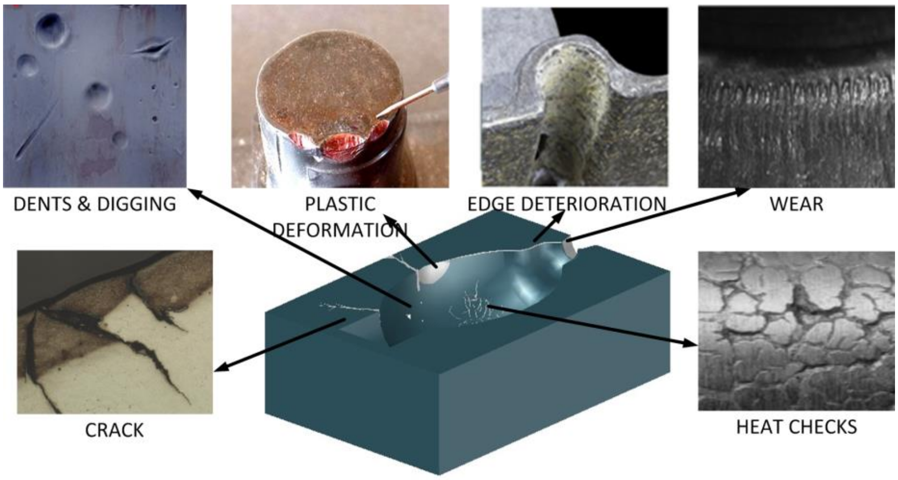

Fig. 1.6: Types of defects in dies and molds (Jhavar et al., 2013).

1.4.5 Surface Modification

AM is an effective process for performing surface modification on abrasion, wear, and heat sensitive components. AM can modify working surfaces of the critical components by coating or texturing. It enhances operating performance and useful life of critical components.

1.4.5.1 Coating

Surface coating plays a vital role in enhancing performance of those components that constantly perform under adverse environment which involves either high operating temperature, dynamic and/or fluctuating loading conditions, highly reactive environment (i.e. corrosive, alkaline, acidic or saline), higher wearing environment (i.e. erosive, abrasive, fretting) or their combinations. Some illustrative examples of such components are gas turbine blades, engine exhaust valves, gate valve, dies and moulds, cutting tools, etc. The adverse work environment leads to higher wear and tear of these components and eventually their premature failure. Use of AM coating process for such components makes their operation trouble-free and enhances their useful life (Lu et al., 2018). Fig.1.7 depicts surface modification process by a laser-based AM process.

1.4.5.2 Surface Texturing

Surface texturing has recently emerged as a promising and environment friendly method for creating growth-fostering texture on implants, texturing the metallic surface to improve its bonding with plastics, effective heat removal from the machining zone, texturing pattern on the tool grips and for the improving the wear resistance of the critical components (Li et al., 2017). Various AM processes can be used for surface texturing of different pattern such as dimple texturing, spot texturing, and groove texturing (Fig. 1.8).

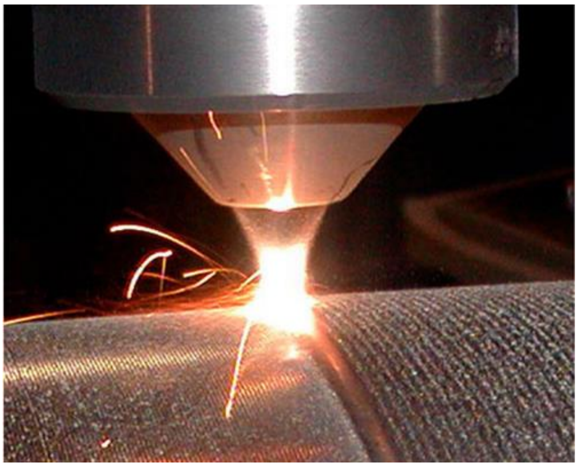

Fig. 1.7: Photograph of surface modification process by a laser-based additive manufacturing process (Lu et al., 2018).

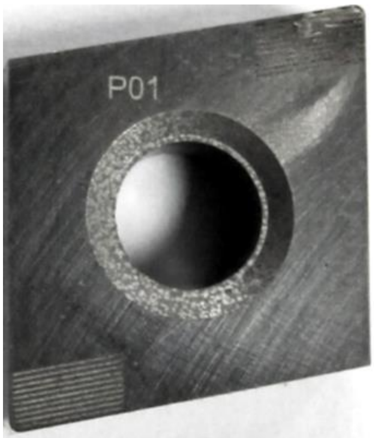

Fig. 1.8: Photograph of the textured groove on rake face of a cutting tool (Li et al., 2017).

1.5 Challenges in Additive Manufacturing

AM faces challenges from poor surface finish, geometrical accuracy, properties, higher cost, and material of the additive manufactured product. The AM products have poor surface finish and geometrical accuracy due to layered deposition. It necessitates use subsequent use of appropriate finishing processes which increases production time and cost. Cost of an AM product increases as production volume increases unlike cost of the products manufactured by conventional processes which decreases as production volume increases. Moreover, AM requires support structure for manufacturing the parts and some AM processes (energy beam-based processes) have higher capital and operating cost which increases the cost of AM products. AM processes face lot of challenges in deposition of the advanced materials such as titanium alloys, superalloys, shape memory materials (SMM), composites, ceramics, FGM. Formation of defects and tensile residual stresses is a critical problem in AM of high-melting point materials because of higher thermal stresses caused due to rapid shrinkage of the molten pool and/or high temperature gradients in the deposition (Lin et al., 2016).

1.6 Additive Manufacturing Processes for Metallic Materials

In first two decades of 21st century, some AM processes have been introduced, developed and patented for metallic materials. These processes can be categorized according to type of energy source used in an AM process which important criteria distinguishing among them. Figure 1.9 shows classification of different AM processes for the metallic materials according to type of energy source used by them. Energy beam and arc are the commonly used heat source in different AM processes. Following paragraphs briefly describe the process principle, applications, advantages and limitations of these processes. It helps to identify the gap between the capabilities of the existing AM processes.

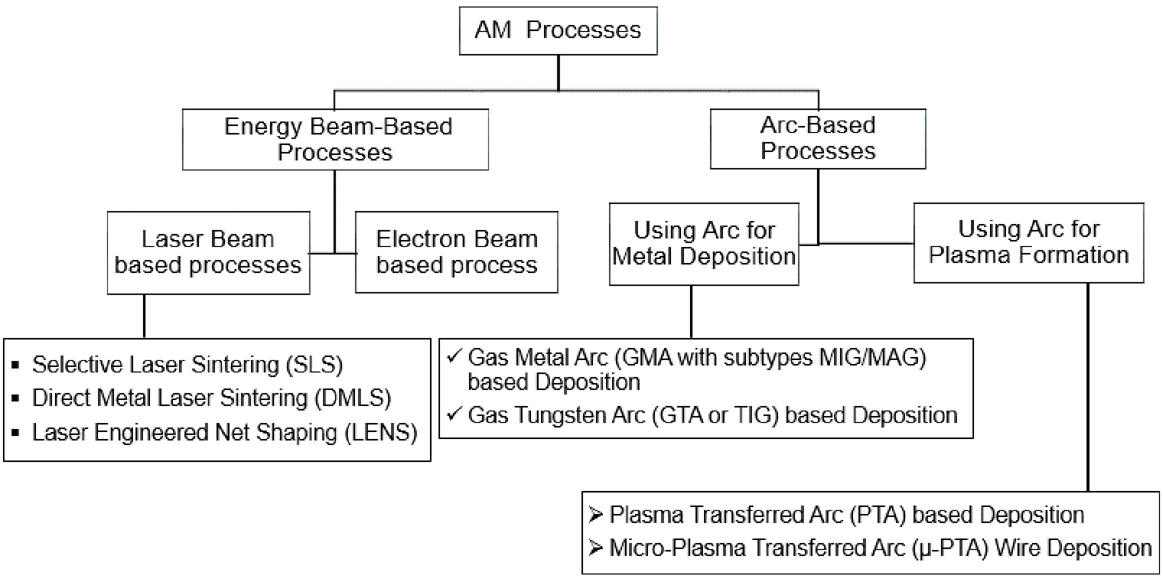

Fig. 1.9: Classification of the AM processes for the metallic materials according to type of energy source.

1.6.1 Energy Beam Based Processes

Energy beam based processes use either laser or electron beam as heat source. They have higher heat transfer efficiency and yield very good quality of deposition, but they are very costly, provide low deposition rate, and more suitable for miniature sized AM of the metallic materials.

1.6.1.1 Selective Laser sintering (SLS)

Selective laser sintering (SLS) is an energy beam based AM process which was developed and patented by University of Texas at Austin in the mid-1980s. Fig. 1.10

shows its working principle schematically. In this process, the laser scans over the powdered bed of the deposition material and selectively melts it partially or fully along with partial melting of the previously deposited layer. After each scanning, the powder bed is lowered by single layer thickness and a new layer of the material is applied on top and the process is repeated until the part is completed. The complete process is performed in a sealed box filled with an inert gas to avoid risk of explosion. This box is maintained at a temperature just below the melting point of the deposition material. This allows the laser to generate only a slight increase in temperature to melt the powder thus speeding up the process. Preheating of the powder helps in defect-free deposition (Yuan et al., 2018). It can be used for polymer (i.e. nylon, polystyrene) and metallic materials (i.e. steel, titanium alloy). It is similar to direct metal laser sintering (DMLS). The version of the SLS which fully melts the deposition material is called selective laser melting (SLM). SLS does not require any support structure, because the powder bed itself can support the material to be deposited subsequently. This reduces consumption of the deposition material and finishing time. But, it takes more time for the products to cool down before removal from the machine. Non-uniform size, shape and orientation of the powder particles lead to poor microstructure of the built product. The powders used in the SLS process are generally less hazardous than the liquids used in the stereo lithography (SL) process although some powder can be explosive if suspended in air. Moreover, the recycled powders may contain impurities and moisture, which can generate the defects such as porosity and inclusions in the SLS manufactured products.

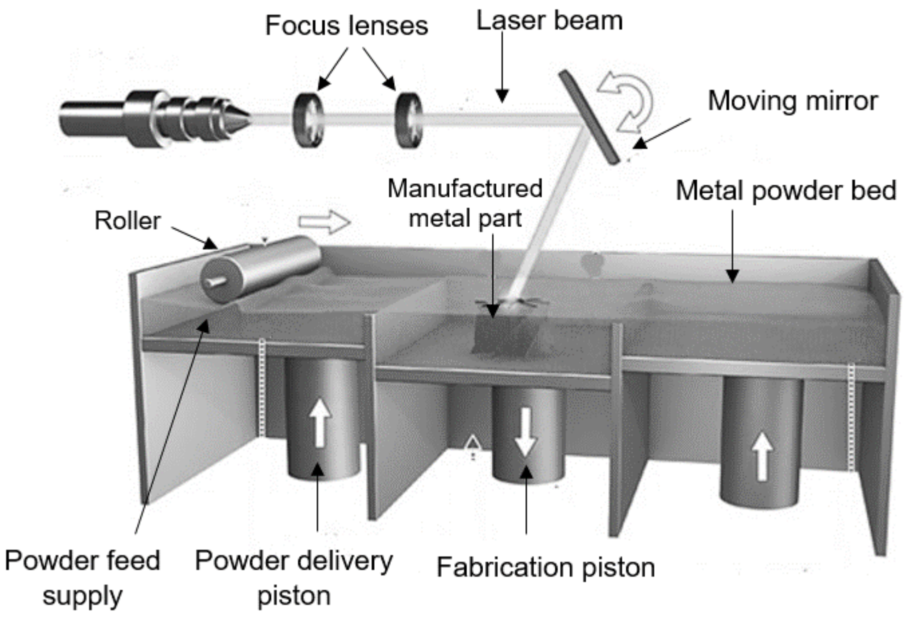

Fig. 1.10: Working principle of the SLS process (Yuan et al., 2018).

1.6.1.2 Laser Engineered Net Shaping (LENS)

Laser engineering net shaping (LENS) process was developed by Sandia National laboratories, USA and it was commercialized in 1997 by Optomec Design Company, USA. Fig. 1.11 shows working principle of LENS process schematically.

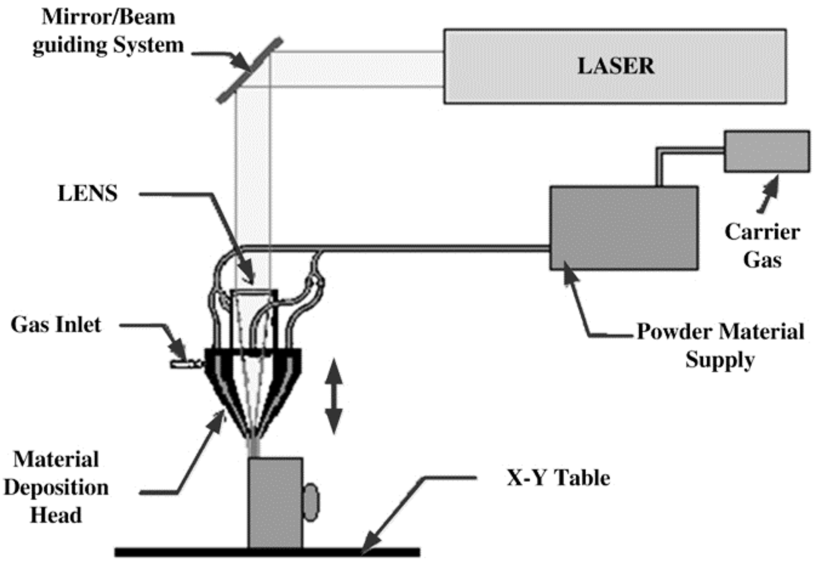

Fig. 1.11: Working principle of the LENS process (Palčič et al., 2009).

Additive deposition of layer is carried out by fusing powdered material (which is injected coaxially to a specific location through a deposition head) within the focal zone of a high-power laser beam. This results in melting and solidification of the deposition material at the desired location. The X-Y table is moved in raster manner to fabricate each layer of the parts. The head is moved up vertically after each layer is deposited. Generally, the process is carried out in a closed chamber filled with an inert gas or in inert shroud gas to shield the melt pool from atmospheric gases for better control of the properties of the AM product. This process has the potential to manufacture complete and dense components from ceramic and metallic materials (Palčič et al., 2009). It is very flexible because components from different materials and having different properties can easily be manufactured. It can be used for manufacturing the parts with specific requirements and applications.

1.6.1.3 Electron Beam Melting

Electron beam melting (EBM) is an emerging process developed by Arcam AB Sweden. It utilizes electron beam at relatively high voltage typically in the range of 30 to 60 kV. Fig. 1.12 shows schematic of working principle of EBM process. The process is similar to selective laser melting with the only difference being the power source. The process possesses advantage of very high energy density and capability to process wide variety of materials. EBM is the best suited for those applications where high strength is required because it produces extremely dense objects that matches characteristics of a fully dense target material (Karlsson et al., 2013). Its major drawback is requirement of vacuum environment for its operation. It also has very high installation and operating costs.

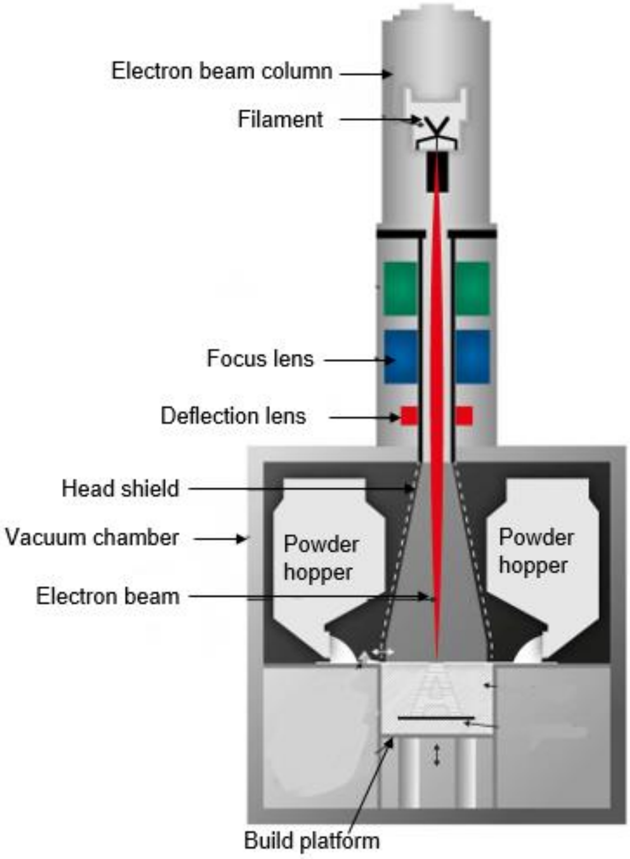

Fig. 1.12: Working principle of the EBM process (Karlsson et al., 2013).

1.6.2 Arc Based Processes

The arc-based deposition processes are classified into two categories i.e. those processes which directly use arc for material deposition and those processes which use arc for formation of plasma which in turn provides heat for material deposition. These processes incur lower capital and operating cost and give higher deposition rate than energy beam based processes.

1.6.2.1 Processes Using Arc for Metal Deposition

In these processes the arc is generated between electrode and the substrate material and it is used for metal deposition. Following paragraphs briefly describe the various arc-based processes.

Gas Metal Arc Deposition (GMAD): Fig. 1.13 shows schematically the working principle of GMAD process in which an electric arc is formed between a consumable wire electrode made of the deposition material (connected to negative terminal of DC power supply) and the substrate (connected to positive terminal of the DC power supply). The arc heats the substrate and the deposition material causing them to melt and fuse together. A shielding gas is provided through the deposition head, along with the wire electrode, which shields the deposition from the atmospheric contaminants (Akula et al., 2006). It is sometime also referred as metal inert gas deposition (MIGD) or metal active gas deposition (MAGD). It offers advantages in terms of higher deposition efficiency and lower capital and maintenance cost. But, this process is found to be energy inefficient and yielding poor deposition having porosity and oxides.

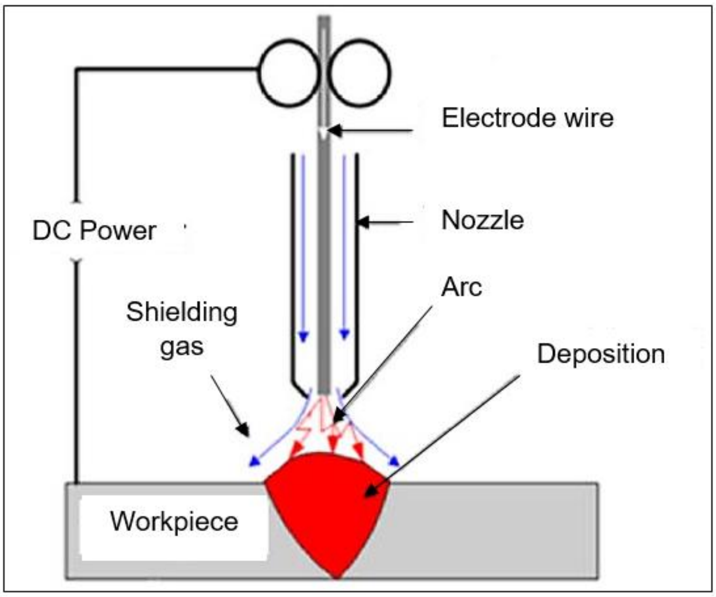

Fig. 1.13: Working principle of GMAD process (Kalpakjian and schimid, 2014).

Gas Tungsten Arc Deposition (GTAD): It is the most commonly used arc-based deposition process. Fig. 1.14 shows schematic of its working principle in which an arc is generated between a non-consumable tungsten electrode (connected to negative terminal of DC power supply) and the substrate (connected to positive terminal of the DC power supply). The produced high amount of heat is used to melt the deposition material supplied in the form of wire or powder. The process is easy to operate, highly portable and less time consuming (Madadi et al., 2012). Sometimes, it is also referred as tungsten inert gas deposition (TIGD). It is widely used to repair the dies due to some special qualities such as highly concentrated arc and stability which provide controlled track deposition.

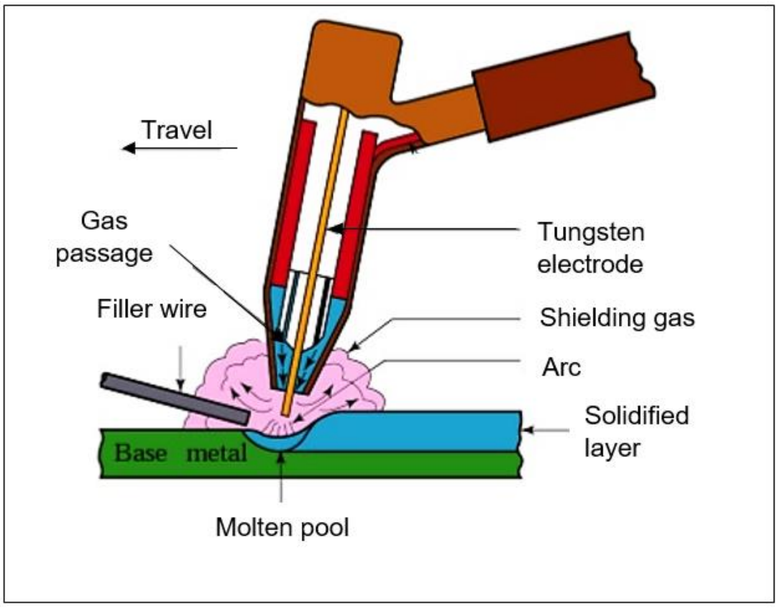

Fig. 1.14: Working principle of GTAD process (Kalpakjian and schimid, 2014).

1.6.2.2 Processes Using Arc for Plasma Formation

In these processes, a pilot arc is generated inside the deposition head which generates the plasma between the deposition head and substrate. Following paragraphs briefly describe the processes which use arc for plasma formation.

Plasma Transferred Arc Deposition (PTAD): It is an advanced form of GTAD process in which a pilot arc is produced, as shown in Fig. 1.15, between the negatively charged tungsten electrode and the positively charged constricting nozzle generally made of copper. This pilot arc ionizes the plasma gas thus forming its high power plasma between the deposition head and the substrate. This plasma can produce an instantaneous temperature of the order of 25,000°C. This plasma is forced to pass through the constricted nozzle the deposition head thus accelerating it towards the substrate. The positioning of the non-consumable electrode within the deposition head is the key difference between GTAD and PTAD processes. The PTAD gives better results than GTAD in terms of efficiency, quality of deposition and cost of production. PTAD offers option to operate it in the straight, reverse and variable polarities. The plasma jet of PTAD and shielding gas prevent entry of the surrounding gases to the deposition zone and thereby providing a better shield to avoid atmospheric contamination. The PTAD process has advantages of higher deposition rates, and lower costs operation as compared to the energy beam processes (Motallebzadeh et al., 2015).

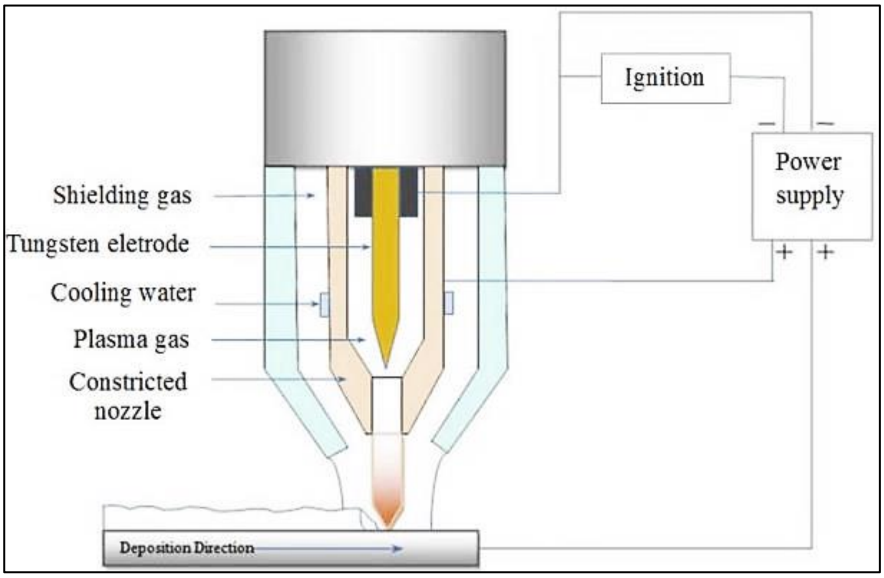

Fig. 1.15: Working principle of PTAD process.

Micro-plasma Transferred Arc Deposition (μ-PTAD): With the advancement in digital power supply and process control, it has become possible to develop micro-version of PTAD process referred as micro-plasma transferred arc deposition (μ-PTAD) process which can be operated at very low current of the order of 0.1 mA with finer control. The principle of plasma generation in the μ-PTAD process is essentially same as that in the PTAD process. This enables the μ-PTAD process to generate precisely controlled and focused micro-plasma arc which gives almost negligible heat affected zone (HAZ), low material distortion, deeper penetration. Additionally, it offers advantages such as improved steady arc direction and stability. The equipment can be automated with the use of a computer numerical controlled (CNC) machine or robotic arm and can be operated either in continuous or pulsed power mode. The μ-PTAD process suits best for miniature or small amount of metal depositions which is required in the small parts manufacturing, repairing of defective/damaged dies, gears, and similar engineering components. Deposition materials can be used either in the form of wire, powder, or combination of both (Jain et al, 2016).

1.7 Comparison of Wire and Powder-based AM Processes

The deposition materials can be used either in wire or powder form in an AM process. Advantages and disadvantages of these forms help the researchers to make proper choice. Table 1.1 compares the wire and powder-based AM processes. The wire-based AM processes have nearly 100% deposition efficiency and less health hazardous than the powder-based AM processes. Moreover, the wire is always in direct contact with the melt pool on the substrate. Any inaccuracy in wire positioning and wire-feed rate disturbs the shape and size of melt pool. This disturbance leads to non-uniform/unsymmetrical shape of deposition. Therefore, the positioning of the wire with respect to the substrate and its size is critical in the wire-based AM processes. In powder-based AM processes, the major advantage is in terms of flexibility in powder deposition rate, flexibility of mixing of different deposition materials, attainment of higher deposition rate and better metallurgical bond between the deposition and substrate materials. Moreover, there are very useful materials (i.e. hard and/or brittle metals and alloys, refractory materials, ceramics, some composites, FGM, and SMM) which are difficult to be drawn as wire but easily available in powder form. The deposition material in powder can be supplied in three different ways i.e. (i) powder delivery being not coaxial with heat source, (ii) continuous powder delivery coaxial with the heat source, and (iii) discontinuous powder delivery coaxial with the heat source (Jhavar et al., 2013).

Table 1.1: Comparison of wire and powder-based deposition processes.

Wire-based AM Processes	**Powder-based AM Processes**
Low deposition rate	High deposition rate
Higher deposition efficiency	Less deposition efficiency
Control of deposition geometry is difficult	Better control over deposition geometry
Metallurgical bond with the substrate is not as good as in a powder-based AM processes	Good metallurgical bond with the substrate
Less hazardous	More hazardous

1.8 Organization of the Thesis

This thesis is organized into eight chapters which explain all the aspect of the present research objectives:

Chapter 2 presents review of the past work covering aspects of development of new processes, process optimization and process control for the AM, coating and texturing belonging to the categories of energy beam based and arc based AM processes for the metallic materials. It also presents summary of review of the past work, identified research gaps, the objectives of the present research work and the research methodology used to meet the research objectives.

Chapter 3 presents the concept of the μ-PTAPD process as well as design and development of its experimental apparatus. It describes the different subsystems and the components used in the development of the experimental apparatus. It also presents the various process parameters of μ-PTAPD process as well as selection of materials for the coating, AM and texturing purposes.

Chapter 4 presents planning and details of the experimental work, evaluation and characterization of the responses as well as results and analyses for the Stellite coating by μ-PTAPD process. It describes the effect of travel speed of worktable on microstructure, secondary dendritic arm spacing, line scan analysis and microhardness of the Stellite coating. It also presents comparative evaluation of μ-PTAPD, PTAD and laser-based deposition processes in terms of morphology, wear characteristics, and microhardness of Stellite coating.

Chapter 5 presents planning and details of the experimental investigations, evaluation and characterization of the responses as well as results and analyses for the additive manufacturing of titanium alloy by μ-PTAPD process. It describes the effect of input process parameters on single-layer single-track deposition characteristics such as deposition height, deposition width, power consumption per unit mass flow rate of powder and energy consumption per unit traverse length. It also presents details of the characterization and analyses of multi-layer single-track deposition of Ti-6Al-4V by continuous and dwell modes. It ends with comparison of performance of μ-PTAPD with other existing AM processes.

Chapter 6 presents planning and details of the experimental investigations, evaluation and characterization of the responses along with the results and their analyses for the texturing of the HSS tool by μ-PTAPD process with an objective to improve performance of material removal process of titanium alloys. It presents the effect of μ-PTAPD process parameters on dilution of the spot textures as well as on diameter, depth, and aspect ratio of dimple textures. It also compares the performance of textured HSS tools with non-textured high speed steel (HSS) tool in terms of machining forces, temperature and wear of the tool, chip formation, and surface roughness of titanium alloy workpiece.

Chapter 7 describes the development of a generic mathematical model to predict dilution of single-layer single-track deposition by μ-PTAPD process along with its experimental validation.

Chapter 8 summarizes the significant achievements and conclusions from the research work reported in this thesis along with the identified directions for the future research work.

Chapter 2

Review of Past Work and Research Objectives

This chapter presents review of the past work on different AM processes for the metallic materials belonging to categories of energy beam based and arc based processes covering aspects of their development, optimization, control, advantages, disadvantages and their applications for coating, additive manufacturing and texturing purposes. It also presents summary of review of the past work, identified research gaps, the objectives of the present research work and the research methodology used to meet the research objectives.

2.1 Past Work on Energy Beam Based AM Processes

Energy beam (laser and electron beam) based AM processes focus energy over very small area of substrate which generates sufficient thermal energy to melt the deposition material (used either in powder or wire form) and fuse it with the substrate or previously deposited layer to produce an AM product. Different researchers have worked on different aspect of these processes during the last decade. Following three subsections present review of past work done on additive manufacturing, coating and texturing by different energy based AM processes.

2.1.1 Review of Past Work on Additive Manufacturing

Palčič et al. (2009) described LENS as an innovative process which offers a breakthrough in additive manufacturing, tools manufacturing, biomedical engineering, and repairing of the metallic products. They presented a comparison of titanium alloy medical implant manufactured by a conventional process and LENS. The LENS manufactured medical implant offered advantages for practical applications such as lightweight due to its hollow structure, easier to insert, and requiring less complicated surgery procedure without use of any complicated instruments over the conventionally manufactured implant. Their results also showed that the LENS manufactured medical implant also had better mechanical properties than the conventionally manufactured implant. The LENS deposited medical implant had rough surface which consequently improves its stabilization in the bone.

Brandl et al. (2011) used 3.5 kW Nd:YAG laser to deposit single layers of Ti-6Al-4V wire on Ti-6Al-4V substrate. Process parameters such as laser beam power, deposition speed, and wire feed rate were varied to perform various experiments. Their experiments revealed relationship between microstructure of the deposition and the process parameters which is helpful for repeatable and predictable manufacturing and for the understanding of the multi-layered depositions. Microstructural characteristics of the deposition and their dependence on various process parameters were studied. Fig. 2.1 shows photograph of 150 mm long single layers of Ti-6Al-4V deposited on same material substrate.

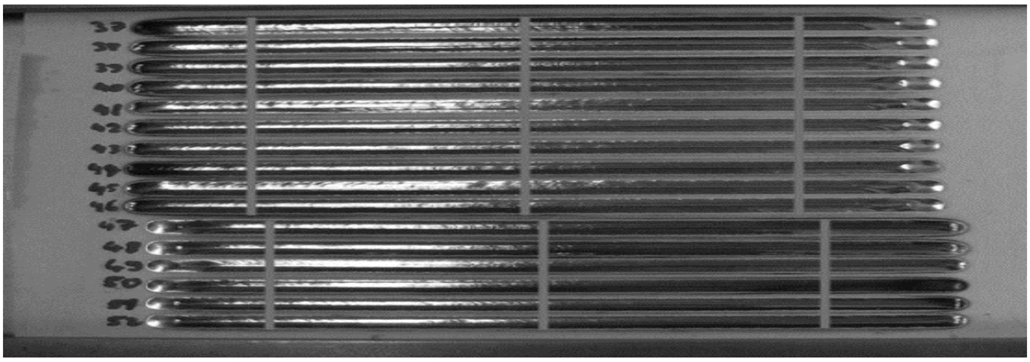

Fig. 2.1: Photograph of deposition of single layers of Ti-6Al-4V wire on substrate of the same material (Brandl et al., 2011).

Heralic et al. (2012) investigated on laser metal wire deposition (LMWD) process for solid freeform fabrication by having online process control by an integrated monitoring system. This system continuously monitors the deposition process and maintains constant value of stand-off distance (SOD) between the robot-held deposition head and substrate. It ensures uniform deposition in each layer. They used their apparatus for manufacturing the parts used in the jet engines and showed that integration of the monitoring system with LMWD process yields very good results for automatic AM of 3D parts.

Gharbi et al. (2013) used Yb-YAG laser for multi-layer deposition of Ti-6Al-4V powder and investigated the mechanisms responsible for its poor surface finish. They developed an analytical model relating surface finish with the melt-pool geometry and found that poor surface finish is due to sticking of the unmelted or partially melted powder particles to deposition and formation of menisci of pronounced curvature radii. They concluded that reducing the layer thickness and increasing melt-pool volume help in improving surface finish of the multi-layer deposition.

Chandramohan et al. (2017) used Nd-YAG laser beam for multi-layer deposition of Ti-6Al-4V powder in horizontal and vertical directions and studied effect of heat treatment on their wear and corrosion resistance. They found that heat treatment influences more than the build direction in determining wear and corrosion resistance of the depositions. They also found that heat-treated specimens of vertical and horizontal depositions had better corrosion resistance than the sintered samples of Ti-6Al-4V.

Mahamood and Akinlabi (2017) investigated influence of laser power and flow rate of powder on metallurgy and mechanical properties of single-layer deposition of Ti-6Al-4V by laser deposition process. They identified that microhardness and the surface roughness of Ti-6Al-4V deposition increases with increase in scanning speed and the powder flow rate. Microstructures changed from the thick lath of basket woven to martensitic microstructure as the scanning speed and the powder flow rate increased. They identified optimum process parameters of laser deposition process for the sound metallurgical and mechanical properties and better surface finish of Ti-6Al-4V deposition which helps to reduce the necessity for secondary finishing operations.

Karlsson et al. (2013) mentioned EBM as a revolutionary technique to manufacture the customized parts to near net-shape from different metallic materials. They compared characteristics of the parts manufactured from two different size of powder particles of Ti-6Al-4V by EBM and found that their microstructural and mechanical properties are not significantly affected by size of powder particles of Ti-6Al-4V alloy.

Edwards et al. (2013) used EBM for deposition of the Ti-6Al-4V powder and evaluated its fatigue properties. They found that fatigue performance of the EBM deposited specimen is lower than wrought Ti-6Al-4V due to porosity and surface roughness.

2.1.2 Review of Past Work on Coating

Jendrzejewski et al. (2008) mentioned that coatings play significant roles in improving the surface properties of those parts which operate in adverse environments and require resistance to wear, fatigue, fracture, corrosion, and creep. They used CO_2 laser cladding process for deposition of Stellite coatings on preheated chromium steel substrate and investigated effect of substrate preheating on the cracking susceptibility, wear, and corrosion resistance. They obtained fine dendrite structure, low-porosity and reduction in the cracks due to preheating of the substrate above 650 ^oC. They concluded that increasing preheating temperature of the substrate decreases the corrosion and wear resistances due to transfer of iron from the substrate to Stellite coating.

Chang et al. (2008) used advanced coaxial laser cladding (LC) to deposit Stellite coating on the seat face of the control valves and compared with Stellite coating by conventional PTAD process. Their results showed that the coating by the LC process exhibited higher wear resistance, refined structure, higher hardness and toughness as compared to the coating by the PTAD process which also had micro-cracks. They concluded that finer grain size obtained with the LC process helps in improving the wear resistance. They highlighted advantages of LC process mentioning that it can deposit a thick layer with controlled thickness on selected area of the metal substrate, has a low energy input and causes less distortion of the component as compared to the conventional deposition processes.

Luo et al. (2012) used advanced technology of supersonic laser deposition (SLD) that evolved from cold spray process. In this process, powder particles are injected at the inlet of the nozzle and accelerated by the supersonic jet stream. The subsequent high-speed impact of powder particle with the substrate produces severe plastic deformation, resulting in good bonding with substrate. They compared performance of SLD and LC for Stellite deposition. Their results revealed that SLD deposited coatings had higher wear resistance, refined structure and lesser dilution as compared to LC deposited Stellite coatings. They concluded that wear resistance strongly depends on coating hardness and solidification rate of the deposition.

Luo et al. (2013) used SLD process for Stellite coatings using the optimised process parameters and compared it with the Stellite coating by high velocity oxygen fuel (HVOF) in terms of line scan analysis and scanning electron microscopy (SEM). They found that the coating produced by SLD process had very low dilution and porosity as compared to the coating produced by HVOF process.

Apay and Gulenc (2016) used micro-laser wire deposition process for coating of Stellite 6 on AISI 1015 steel substrate and studied its microstructure, microhardness and wear characteristics. Their results revealed formation of fine dendritic microstructure in the Stellite coating, gradual increase in hardness values from the substrate to the Stellite coating, and increase in wear volume loss with increase in amount of the applied load.

2.1.3 Review of Past Work on Texturing

Sasi et al. (2017) used pulsed Nd-YAG laser for making of micro scale dimples on the rake face of high speed steel (HSS) cutting tool and compared performance of textured HSS cutting tool with non-textured cutting tool in machining of Al7075-T6 aerospace alloy. Their results show that use of textured cutting tools reduces cutting and thrust forces, and tool-chip contact length as compared to the non-textured cutting tools. They mentioned that texturing of the rake face of the cutting tools has recently emerged as a promising and environment friendly method for reducing tool-chip contact length during machining.

Sugihara and Enomoto (2017) made dimple and groove textured patterns on rake face cutting tool using Nd-YAG laser and compared the effects of the different texture patterns on the performance of the cutting tools. They found that dimple textures on cutting tool significantly enhance tribological behaviour and resistance to crater wear. Their results revealed that dimple-textured cutting tool has better performance than the groove textured cutting tool especially in the lubricated condition. They also reported that dimensions and shapes of the texture on the cutting tool surface affect the machining performance, but there are no rules and guidelines for designing effective textures and these parameters are currently optimized using trial and error method only.

Li et al. (2017) mentioned that machining of titanium alloys is difficult due to their low thermal conductivity which increases temperature of the cutting tool. They suggested that machinability can be improved by surface texturing on the tool. They manufactured nine different types of deep submillimeter-sized texturing on the tools using laser and compared the performance of the textured tools with non-textured tool in terms of cutting forces and coefficient of friction at the tool-chip interface. Their results show that parallel textured tool yielded the best performance in reducing cutting force and improving the friction properties on the rake face. They concluded that reduced tool-chip contact area improves the machinability of Ti-6Al-4V.

2.2 Past Work on Arc Based AM Processes

Arc based AM processes focus energy over larger area and offer advantages in terms of capital investment and operating cost, ease of operation, and skill of the operators over the energy beam based AM processes. Different researchers have reported work on different aspect of arc based AM processes during the last decade. Following two subsections describe review of past work done on additive manufacturing, and coating by different arc based AM processes.

2.2.1 Review of Past Work on Additive Manufacturing

Horii et al. (2009) have developed 3D micro-TIG process for rapid manufacturing the products from the metallic materials. They used this process to manufacture 3D parts from Inconel alloy 600 as shown in Fig. 2.2. They found that the manufactured part was fully dense with no visible cracks and pores, and had 690 MPa tensile strength, 43% elongation and 158 HV microhardness.

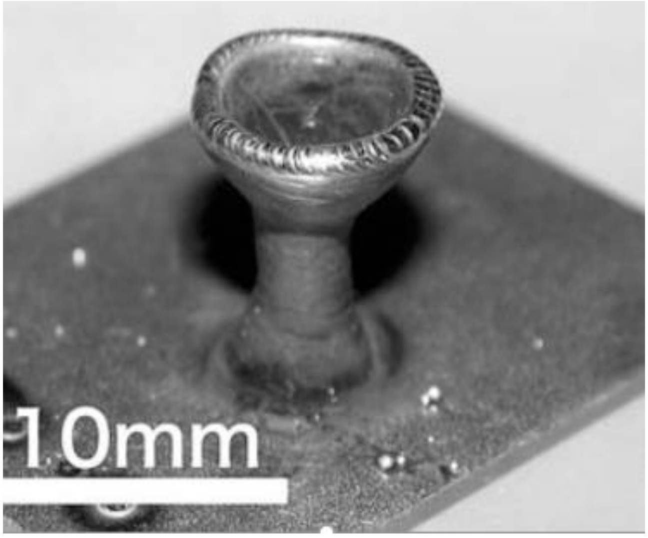

Fig. 2.2: Freeform fabrication of Inconel alloy 600 part by 3D micro-TIG (Horii et al., 2009).

Martina et al. (2012) introduced PTA wire deposition (PTAWD) as a novel AM process and used it for multi-layer deposition of Ti-6Al-4V on substrate of the same material as shown in Fig. 2.3. They studied its characteristics and achieved 93% deposition efficiency and 1.8 kg/h as the highest deposition rate. They also found higher microhardness of the multi-layer deposition than the substrate.

Fig. 2.3: Photograph of multi-layer deposition of Ti-6Al-4V by PTAWD (Martina et al., 2013).

Jhavar et al. (2014) developed cost-effective micro-plasma wire deposition (µ-PTAWD) process for small-sized deposition. They deposited straight wall of AISI P20 wire on substrate of the same material and found that µ-PTAWD process is capable of manufacturing straight walls having total wall width of 2.45 mm and effective wall width of 2.11 mm. They also found 87% deposition efficiency for the maximum deposition rate of 42 g/h.

Lin et al. (2016) used pulsed plasma transferred arc (PPTA) process to additively manufacture multi-layered straight wall of Ti-6Al-4V wire on substrate of the same material. They investigated mechanical properties and morphology of it and found that it consists of various morphologies with different microstructure, such as epitaxial growth of prior β-grains, martensite and horizontal layer bands of Widmanstätten, which depend on the heat input, multiple thermal cycles and gradual cooling rate in the deposition process. Their results showed that the multi-layered deposition had 909 MPa yield strength and 988 MPa ultimate tensile strength. They described PPTA process is a novel, convenient, and cost-effective AM process for aeronautical and biomedical applications.

2.2.2 Review of Past Work on Coating

Gholipour et al. (2011) investigated the microstructure and wear behavior of the Stellite 6 coating on stainless steel (17-4PH) substrate using GTAD process. Their results showed that the microstructure of the coating consisted of carbides embedded in a Co-rich solid solution with a dendritic structure. Their results of the wear tests indicated that the delamination was the dominant mechanism.

Madadi et al. (2012) used optimized pulsed TIG process parameter for deposition of Stellite 6 on plain carbon steel substrate. They found that dilution is significant aspect of a coating. Higher dilution is undesirable because it lowers the mechanical properties due to mixing of materials, higher distortion and more residual stresses. They also described that pulsed TIG process has several advantages such as low heat input, low distortion, controlled deposition volume, less hot cracking tendency and better control of the fusion zone.

Motallebzadeh et al. (2015) mentioned that Stellite is an alloy of cobalt that has higher resistance to abrasive, erosive, and corrosive wear at an operating temperature up to 1100 ^{o}C due to intermetallic compounds and carbides formed in the Stellite coating. They used PTA process for Stellite 12 coating on AISI 4140 steel substrate and studied microstructure and wear resistance of it. They found that chromium and tungsten elements of Stellite promote the formation of carbides ($Cr_{23}C_6$, W_2C) and provide solid solution strengthening in the cobalt matrix which makes the Stellite coating to exhibit superior wear resistance than substrate during dry sliding wear test.

Shoja-Razavi (2016) used HVOF process for Stellite 6 coating and found that the coatings suffer from several drawbacks such as porosity, cracks. Hence, he studied the effects of laser glazing treatment on microstructure, hardness, and oxidation behaviour of Stellite 6 coating deposited by HVOF process. He found that laser glazing treatment helped the Stellite coating to exhibit highly dense and uniform structure with an extremely low porosity than the coating by HVOF process but at the cost microhardness.

2.3 Conclusions from the Past Work

Following conclusions can be drawn from the review of the past work on various aspects of AM processes for metallic materials:

- Energy beam based AM processes are preferred for small sized deposition and the arc based AM processes are preferred for bulk deposition of the metallic materials.
- Several arc based AM processes have been used in the past work for the coatings but, they yield poor bonding of the deposition material with the substrate, thermal distortion, porosity, oxides, higher dilution and lower energy efficiency. These problems have led to the spallation and removal of the coating material and requirement of post-deposition heat treatment to enhance the properties of coatings.
- Main advantages of the energy beam based AM processes include manufacturing of the complex shapes that are difficult to produce with conventional processes, better properties of the deposition, controlled melting which leads to small heat affected zone, negligible defects and very small volume of deposition.
- Major drawback of energy beam based AM processes is inaccessibility of the deposition area because the energy beam is transmitted through straight path using flat mirrors or magnetic field. They are difficult to be used for the materials having high reflectivity. Moreover, they have very high capital, operational and maintenance cost.
- Optimization of AM process parameters plays very important role in their applications. Microstructure of the deposition is depending on the cooling rate which in turn depends on AM process parameters. This makes optimization of AM process parameters even more important particularly for a new deposition process.
- Machining of titanium alloys using cutting tool is difficult due to their lower thermal conductivity which increases the temperature of the cutting tool thus accelerating its wear. Texturing on rake face of a cutting tool has recently emerged as a promising and environment friendly method enhancing removal of heat from the machining zone

2.4 Identified Research Gaps

Following research gaps were identified from the review of the past work on various aspects of different AM processes for the metallic materials:

- There is a wide gap exists between the process capabilities of arc based and energy beam based depositions processes. For example, deposition rate achieved by energy beam based AM processes is in a range from 2 to 10 g/min whereas arc based AM processes can achieve it in a range from 50 to 130 g/min.

- Energy beam based processes are too costly to be used by small and medium scale industries and AM applications requiring miniature or small amount of metallic deposition. Arc based processes are economical but give poor quality of deposition and are not suitable for miniature or small volume of metallic deposition.
- No work has been reported on the μ-PTA powder deposition process for AM applications of the metallic materials, which is economical, material-efficient and energy-efficient, produces good quality of metallic deposition without use of vacuum.
- No work has been reported on the texturing of HSS tool by μ-PTA powder deposition process to improve the machinability of cutting process.

2.5 Objectives of the Present Research Work

The present research work was undertaken with the following research objectives to bridge the identified research gaps:

(i) To develop the experimental apparatus for μ-PTA powder deposition (μ-PTAPD) process for various AM applications of the metallic materials with movement of the deposition head of the apparatus along x, y, and z axes being programmable through a microcontroller.

(ii) To study characteristics of the coating (i.e. single-layer multi-track deposition) of Stellite powder on steel substrate by μ-PTAPD process.

(iii) To compare the capabilities of μ-PTAPD process with laser and PTA-based processes for coating of Stellite.

(iv) To study the characteristics of multi-layer single-track deposition of titanium alloy by μ-PTAPD process using continuous and dwell-time modes and subsequently to manufacture typical additive manufactured product of titanium alloy.

(v) To study influence of dimple and spot texturing by μ-PTAPD process on HSS tool in machining of titanium alloy and to compare performance of textured HSS tools with non-textured tool in terms of machining forces, temperature and wear of the tool, chip formation, and workpiece surface roughness.

(vi) To develop a mathematical model of dilution for single-layer single-track deposition by μ-PTAPD process.

2.6 Research Methodology

Figures 2.4, 2.5, and 2.6 present the research methodology adopted to achieve the identified objectives in the form of flowcharts.

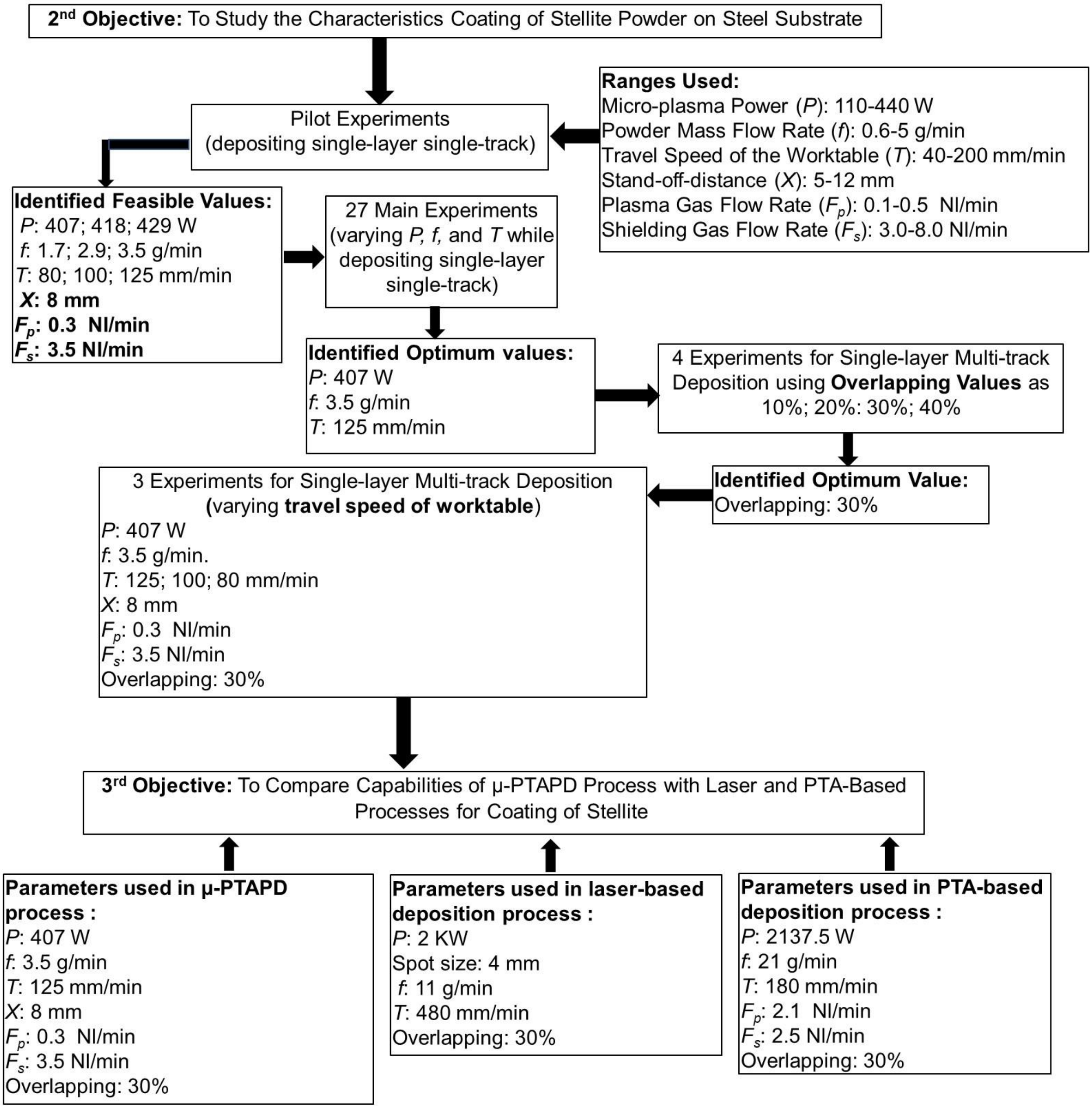

Fig. 2.4: Research methodology used for investigations on Stellite coating.

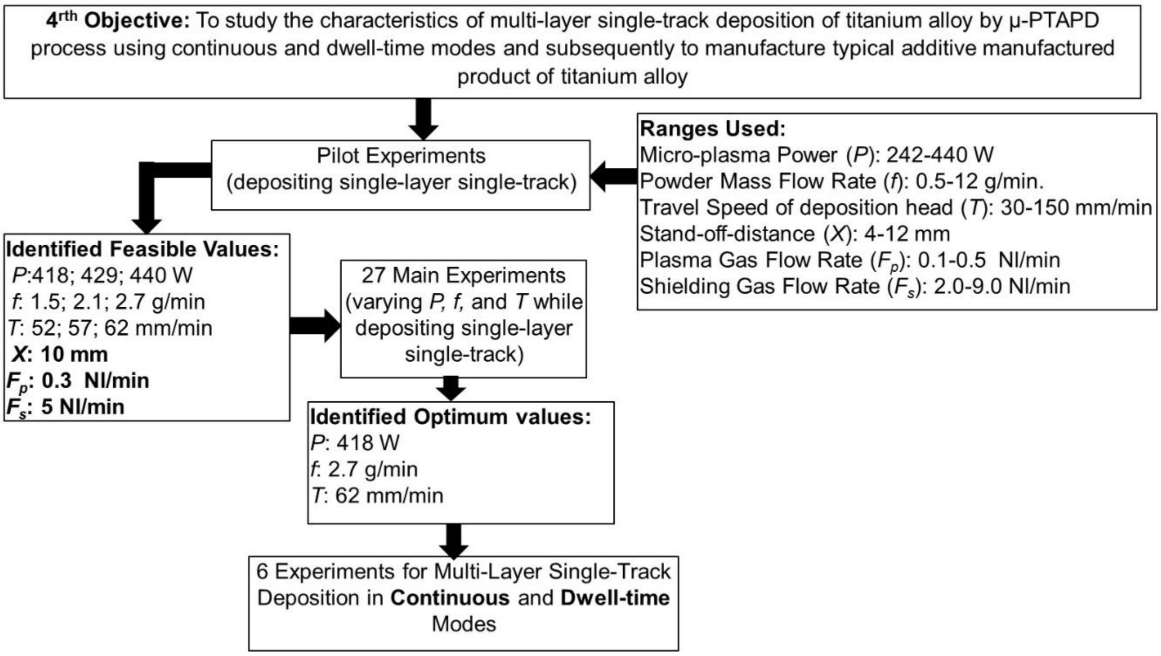

Fig. 2.5: Research methodology used for investigations on additive manufacturing of titanium alloy.

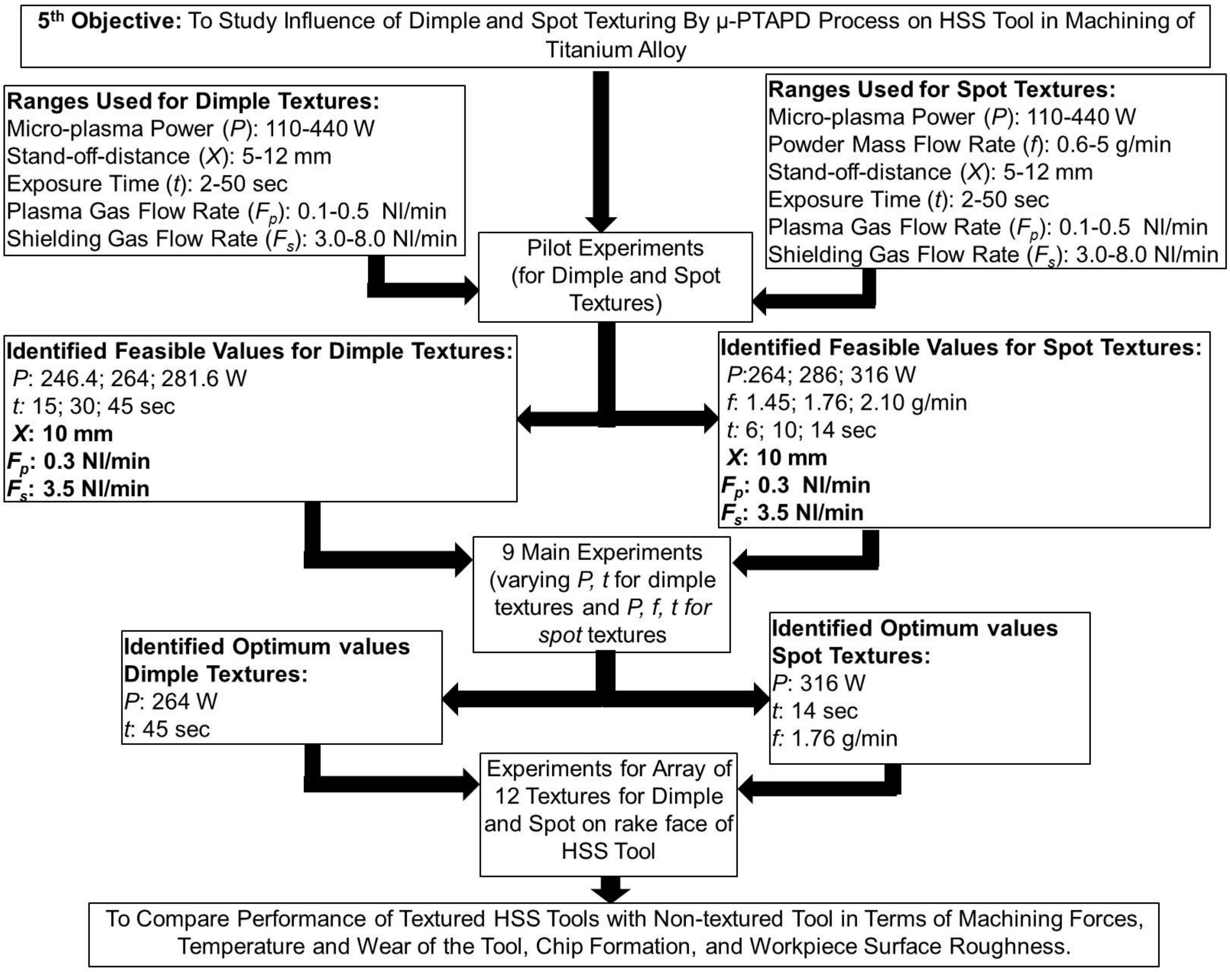

Fig. 2.6: Research methodology used for investigations on texturing of HSS tool.

The ***next chapter*** presents the concept of the μ-PTAPD process as well as design and development of its experimental apparatus. It describes the different subsystems and the components used in the development of the experimental apparatus. It also presents the various process parameters of μ-PTA powder deposition process as well as selection of materials for the coating, AM and texturing purposes.

Chapter 3

Development of Experimental Apparatus

This chapter presents the concept of the μ-PTA powder deposition process as well as design and development of its experimental apparatus. It describes the different subsystems and the components used in the development of the experimental apparatus. It also presents the various process parameters of μ-PTA powder deposition process as well as selection of materials for the coating, AM and texturing.

3.1 Concept of μ-PTA Powder Deposition Process

In powder-based AM processes, the major advantage is in terms of flexibility in powder deposition rate, flexibility of mixing of different deposition materials, attainment of higher deposition rate and better metallurgical bond between the deposition and substrate materials as well as easy availability of the deposition materials in powder form. Figure 3.1 depicts working principle of μ-PTA powder deposition (μ-PTAPD) process which uses very low current in the range of 0.1 to 20 A to generate a pilot arc between non-consumable tungsten electrode (connected to negative terminal of DC power supply unit) and the constricting nozzle housed in a deposition head. This ionizes the inert gas (argon) forming its precisely controlled and focused micro-plasma arc which forms melt pool on the substrate surface by melting the deposition material delivered as powdered stream. When the powder contacts the melt pool it is absorbed into melt pool and creates deposition layer. Use of small current in this process gives almost negligible HAZ, low material distortion, and deeper penetration. This process can greatly reduce the product development time by using modern concepts and techniques of computer aided design (CAD), computer aided manufacturing (CAM), robotics, on-line process monitoring and control. It has the ability to manufacture near-net shape parts of very complex geometries from advanced materials and has potential to overcome limitations of the existing AM processes.

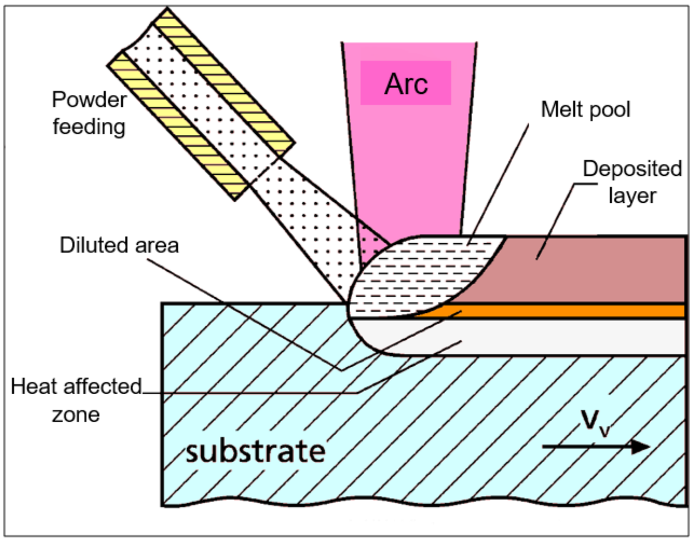

Fig. 3.1: Principle of μ-PTA powder deposition process.

3.2 Design and Development of the Experiment Apparatus

Figures 3.2a and 3.2b show schematic diagram and photograph of the experimental apparatus for μ-PTA powder deposition process developed by integrating (i) power supply unit and torch for micro-plasma, (ii) in-house designed and developed powder feeding system, (iii) in-house developed deposition head, and (iv) manipulator system. Following subsections describe these subsystems of experimental apparatus of μ-PTAPD process.

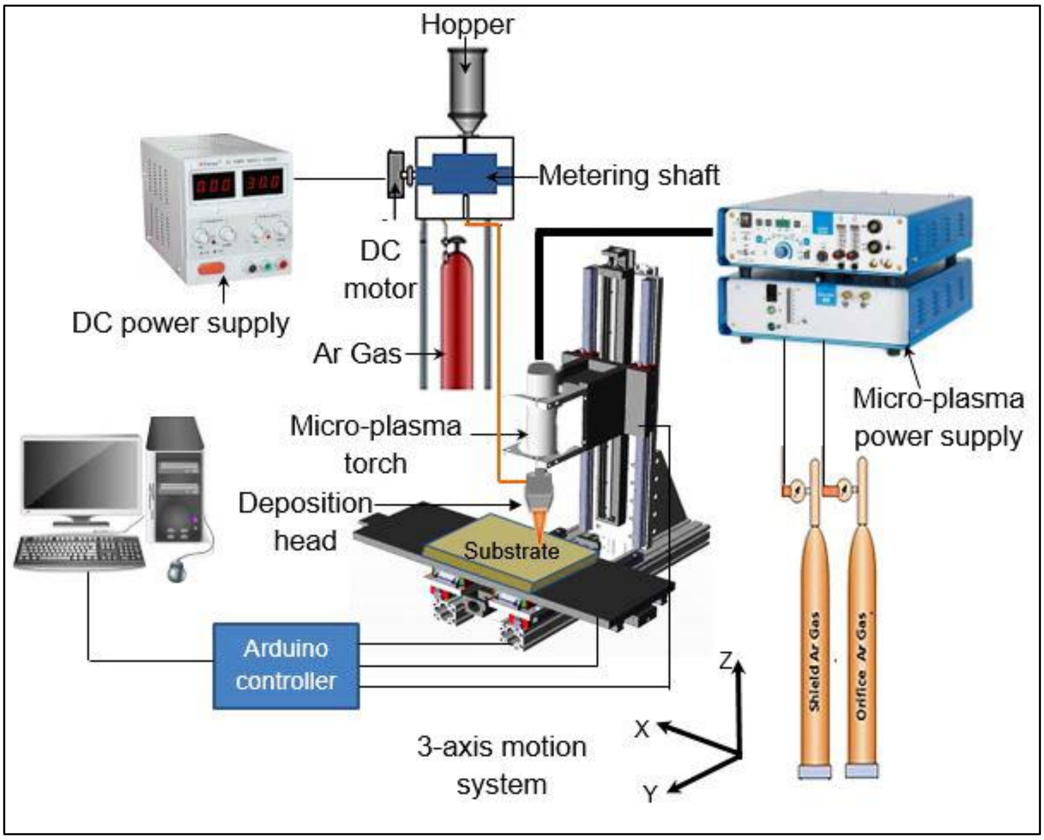

(a)

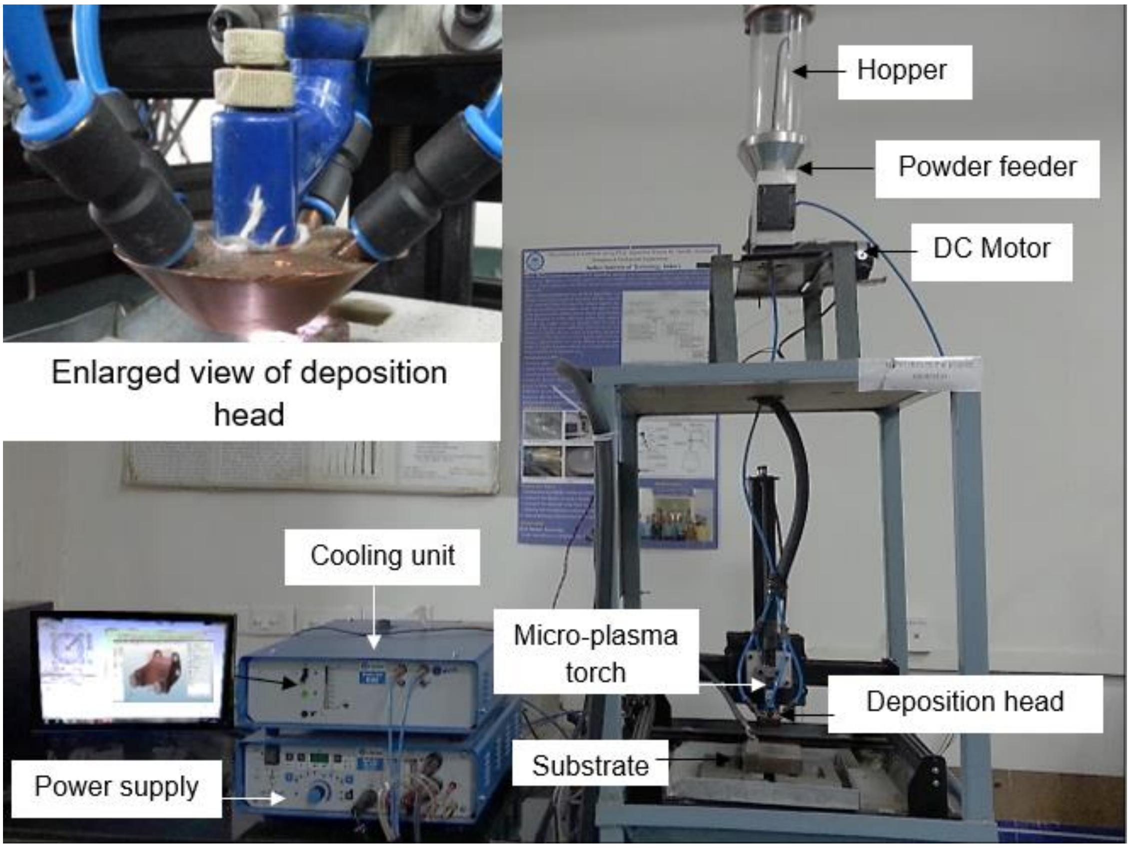

(b)

Fig. 3.2: (a) schematic view and (b) photograph of experimental apparatus developed for μ-PTA powder deposition process

3.2.1 Power Supply Unit for Micro-Plasma

Power supply unit (Fig. 3.3) for micro-plasma (Dual Arc 82-HFP from Pro-Fusion Inc. USA) was used as power source in the experimental apparatus. It has maximum capacity of supplying DC power as 440 W with provision to vary current in a range from 0.1 to 20 A with an increment of 0.1 A while maintaining a constant value of voltage as 22 volts.

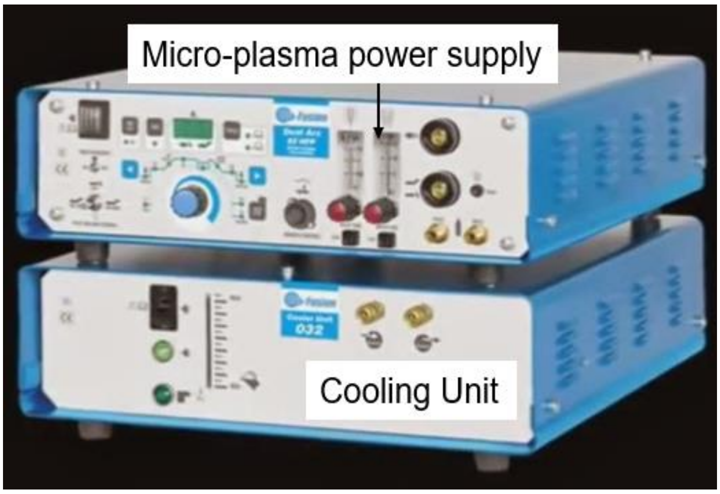

Fig. 3.3: Photograph of power supply unit for μ-PTAPD process.

3.2.2 Deposition Head and Micro-plasma Torch

The deposition head is very important part of µ-PTAPD process because its orientation and position of the powder supplying nozzles with respect to the melt pool significantly affect the powder material efficiency. The deposition head was developed to deliver the deposition material from the powder feeding system to the melt pool. It consists of the micro-plasma torch surrounded by four identical nozzles placed in an inclined manner circumferentially at equal angular interval. This design enables supply of the powdered deposition material at feed angle of 46^o to the centre the melt pool for the stand-off-distance from 8 to 10 mm. Value of the feed angle was chosen in such a way that ensures maximum powder deposition efficiency. Figures 3.4b and 3.4c depict schematic view and photograph of the developed deposition head. The micro-plasma torch (PLT100 series) consisted of tungsten electrode, constricting nozzle, gas lens and gas guiding insert as shown in Fig. 3.4a. Negative and positive terminals of DC power supply unit are connected to tungsten electrode and the constricting nozzle respectively ensuring supply of heat energy required for plasma formation. The plasma-forming gas (i.e. argon) is supplied through the constricted nozzle which is placed inside the micro-plasma torch as shown in Fig. 3.4b. It has a tapered annulus to supply the shielding gas (i.e. argon) to protect the melt pool from oxidation and other contamination by atmospheric gases. It also has circular annulus to supply cooling water from the cooling unit (as shown in Fig. 3.3) to prevent overheating of the micro-plasma torch.

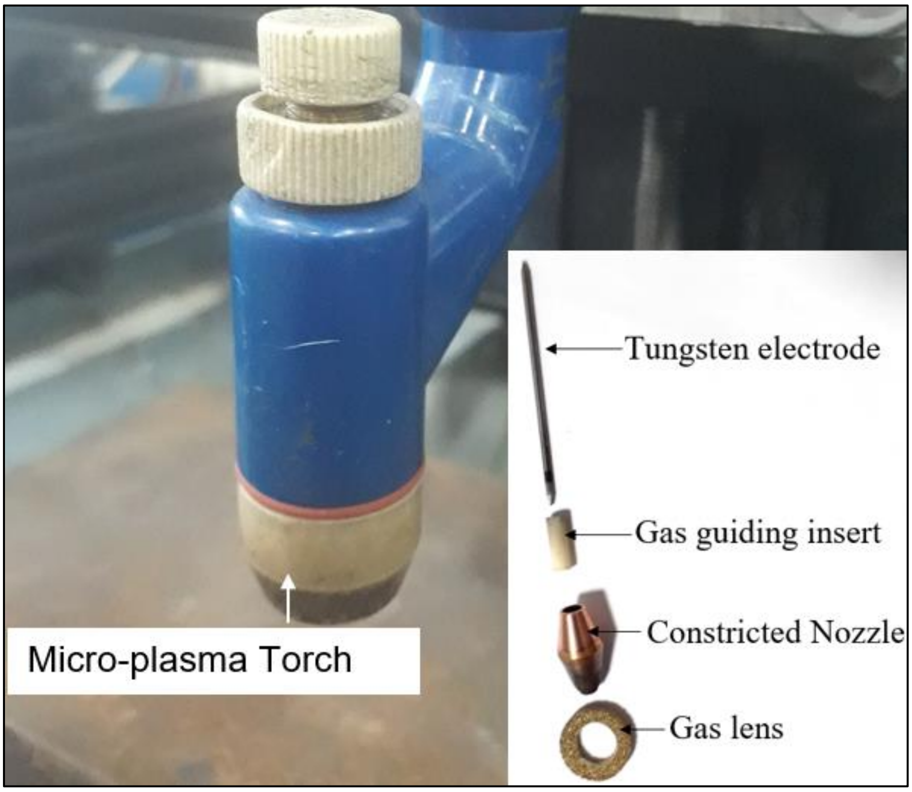
Tungsten electrode
Gas guiding insert
Constricted Nozzle
Gas lens
Micro-plasma Torch

(a)

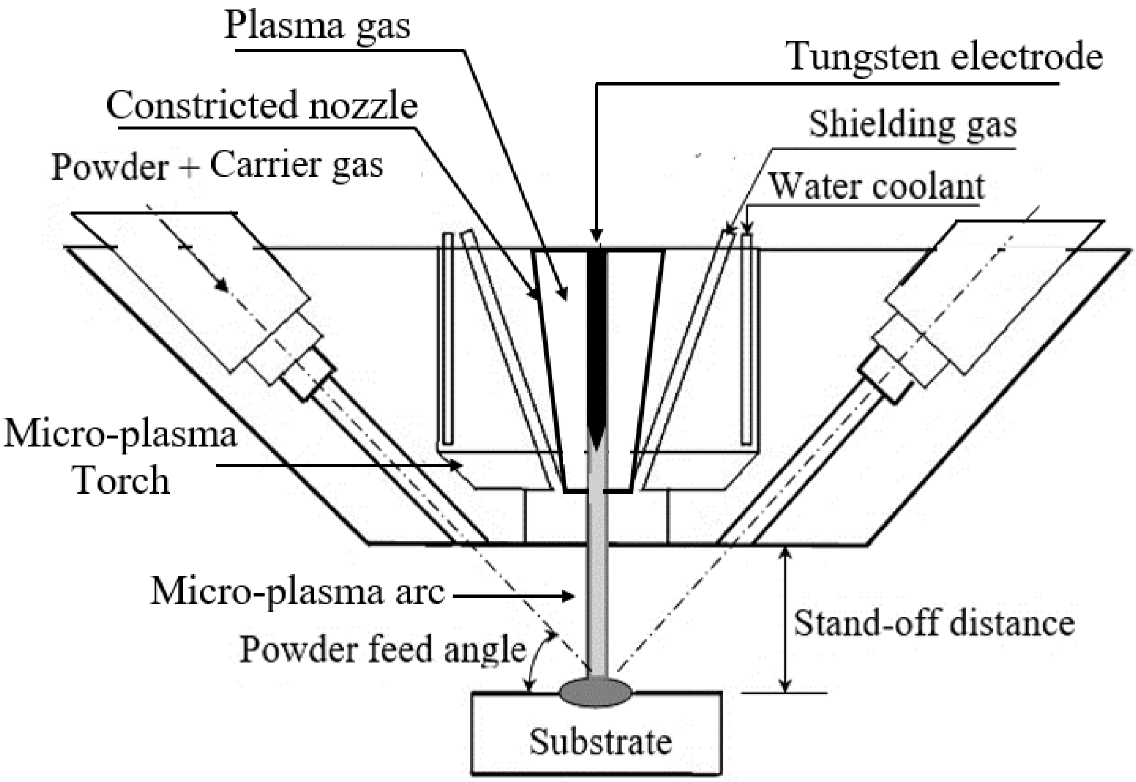
Plasma gas
Tungsten electrode
Constricted nozzle
Shielding gas
Powder + Carrier gas
Water coolant
Micro-plasma Torch
Micro-plasma arc
Stand-off distance
Powder feed angle
Substrate

(b)

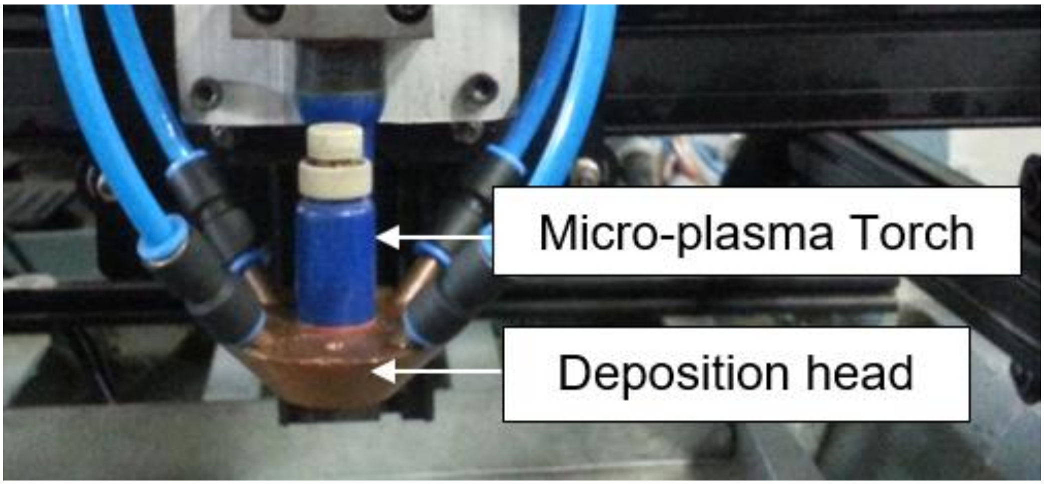

(c)

Fig. 3.4: The deposition head and micro-plasma torch for μ-PTAPD process: (a) micro-plasma torch and its different components; (b) schematic view of the developed deposition head; and (c) photograph of the developed deposition head.

3.2.3 Powder Feeding System

Powder feed rate is important factor for a successful μ-PTAPD process because powder feeder provides continuous and uniform powder stream at the desired mass flow rate to the melt pool. Therefore, powder feeding system was designed and developed to ensure an uninterrupted supply of the deposition material in the powdered form. Its two variants were designed whose details are described in following paragraphs.

First Design of Powder Feeding System

Figures 3.5a and 3.5b depict the schematic view and photograph of the 1st design of powder feeding system respectively. It consisted of a hopper, mixing unit, flow control valve and nozzle. In this powder feeding system, pressurized carrier gas (argon) was supplied to hopper and mixing unit through flow control valve for powder delivery from the hopper to the nozzle. It can vary powder mass flow rate by changing the flow rate of carrier gas through flow control valve. But, following major drawbacks were observed in this design i.e. (i) variation in powder mass flow rate at constant supply of gas flow rate, (ii) sticking of small powder particles to the hopper, and (iii) difficult to use for powder feed rate less than 5 g/min.

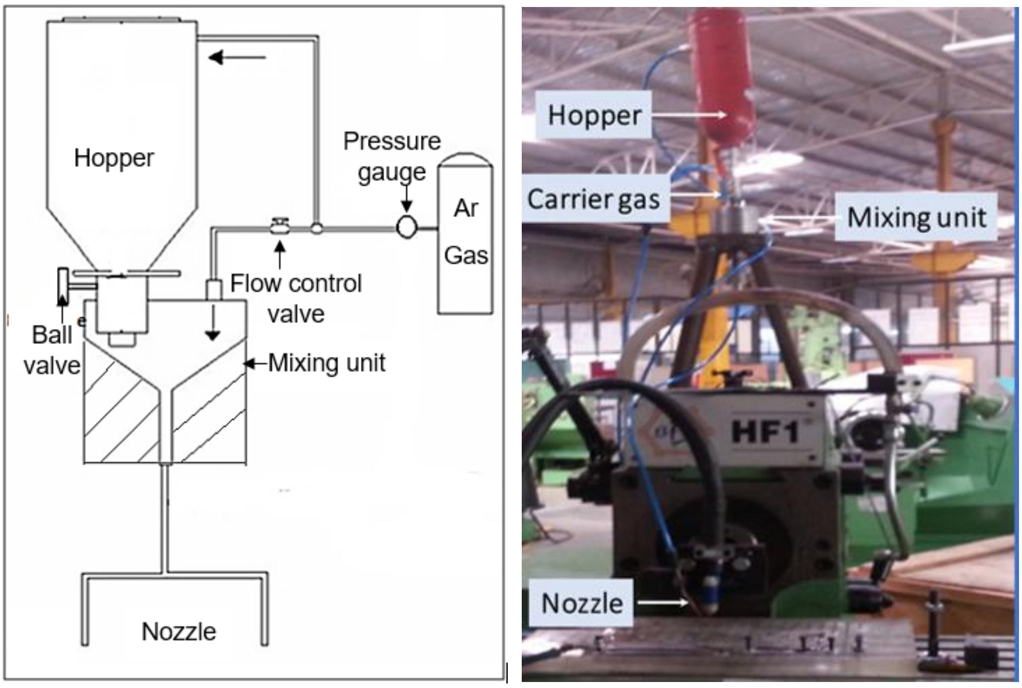

(a) **(b)**

Fig. 3.5: First design of powder feeding system: (a) schematic view and (b) photograph.

Second Design of Powder Feeding System

Figures 3.6a and 3.6b depict the schematic view and photograph of 2nd design of the powder feeding system. It consists of a hopper, shaft, DC motor and power supply unit for the DC motor. Hopper stores the powdered deposition material which is supplied to the deposition head by means of pressurized argon gas supplied at constant flow rate of 0.5 Nl/min. The mass flow rate of the powder can be varied by changing the rotation of a shaft driven by a DC motor. The powder feeding system has capability to supply the deposition material having powder particle size in the range from 20 to 200 µm. It has capability to vary powder mass flow rate in the range from 0.6 to 14.2 g/min for Stellite 6 and 0.51 to 11.3 g/min for Ti-6Al-4V powder according to the experimentally determined relationship depicted in Fig. 3.7a and Fig 3.7b respectively. It can be observed from these graphs that there exists a threshold value of voltage for a non-zero value of powder mass flow rate.

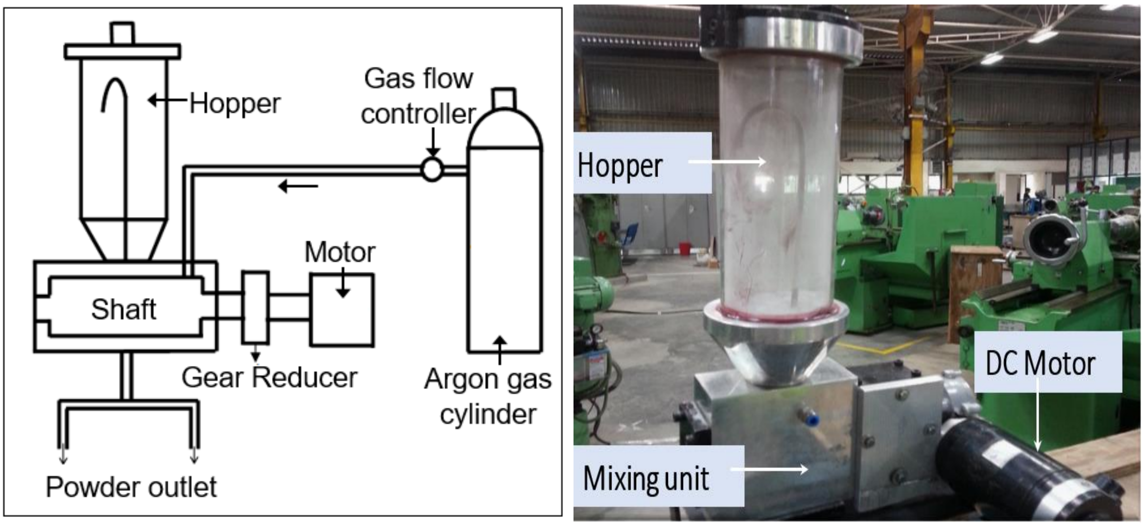

(a) **(b)**

Fig. 3.6: Second design of powder feeding system: (a) schematic view; and (b) photograph.

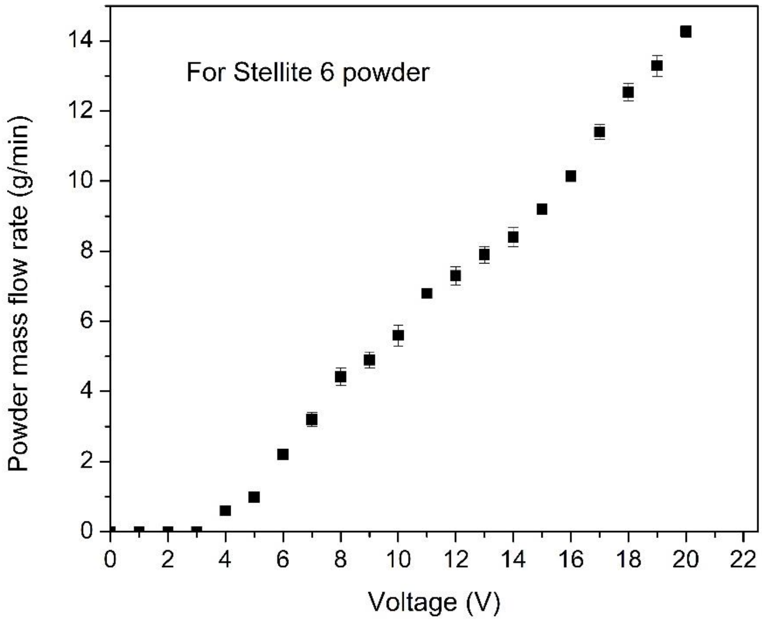

(a)

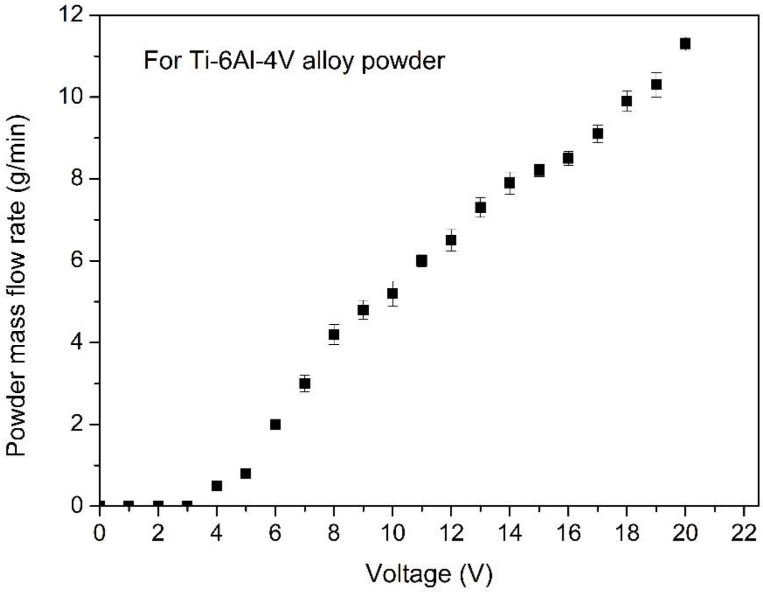

(b)

Fig. 3.7: Relationship between powder mass flow rate and voltage of the DC motor for: (a) Stellite 6 powder; and (b) Ti-6Al-4V alloy powder.

3.2.4 Manipulator System

During initial development of µ-PTAPD process, worktable of a precision knee-type milling horizontal milling machine (model *HF1* from *Bharat Fritz Werner Ltd. Bangalore*, shown in Fig. 3.8) was used for mounting and moving the substrate in X and Y directions. Use of this machine was a cost-effective alternative to computer numerical control (CNC) or robotic manipulators because this machine had capacity to provide discrete values of worktable travel speed as 40, 50, 63, 80, 100, 125, 160, 200, 250 mm/min in the automatic and vibration free mode. A mounting plate was attached to the dog-holes of its spindle to hold the micro-plasma torch with the help of a mounting bracket as shown in Fig. 3.8.

In order to have continuous and precise of the deposition head along X, Y and Z axes, a manipulator system (as shown in Fig. 3.9) was subsequently developed which was microcontroller programed. In this system, movement of the deposition head along the X, Y and Z directions were precisely controlled by one stepper motor for each axis with each stepper motor having minimum incremental motion of 0.1 mm. It has working area of 400 x 400 mm in X-Y directions and travel range from 0.1 to 200 mm in the Z direction. The electronics part of manipulator system has a CNC shield consisting of RAMPS 1.4 mounted on Arduino 2560 board. It can control the movement along the three axes independently or simultaneously. The open source software PRONTERFACE was used to generate deposition path in terms of G and M codes for each deposition layer according to the its height defined in the CAD model of the part to be manufactured. Accordingly, the deposition head moves to facilitate the layered deposition layer to the part.

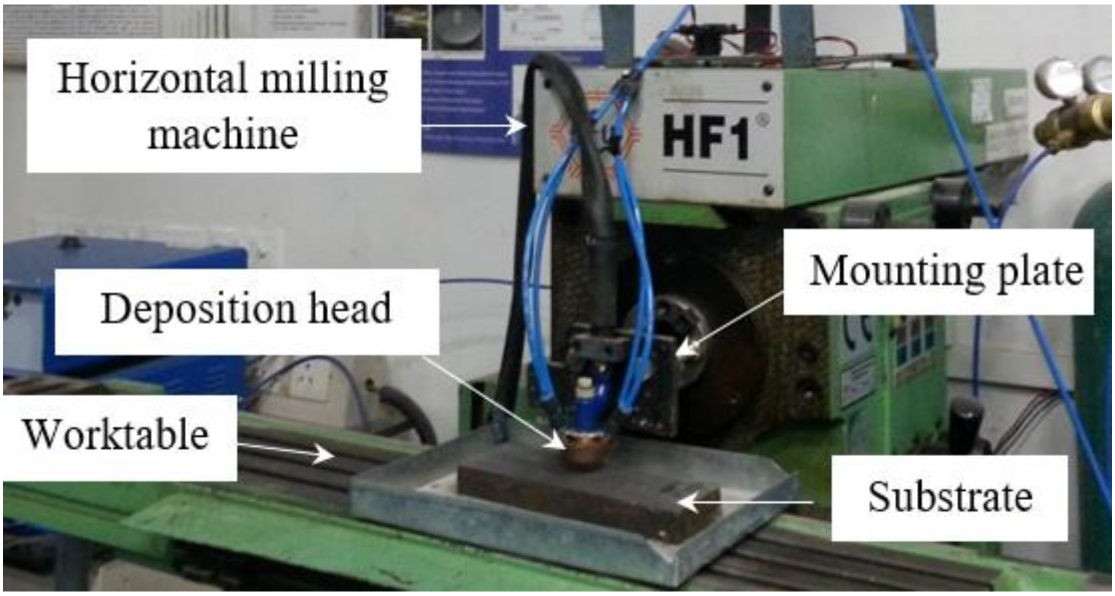

Fig: 3.8: Photograph of manipulator system for movement of the worktable along X and Y axes directions.

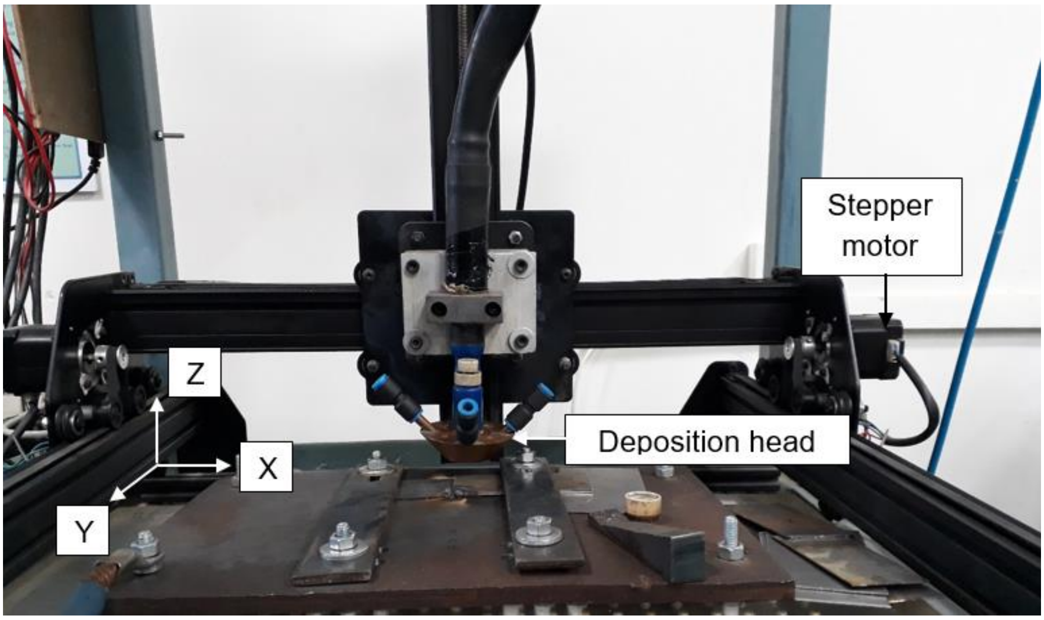

Fig. 3.9: Photograph of the microcontroller programmed manipulator system for movement of the deposition head along the X, Y, and Z axes.

3.3 Process Parameters of μ-PTA Powder Deposition Process

It is important to understand different process parameters and their respective functions during actual deposition in order to develop the process. Various process parameters related to micro-plasma power supply and deposition process affect the performance of the μ-PTAPD process. Figure 3.10 presents important process parameters of μ-PTAPD process and following paragraphs define them and describe their effect on the process performance.

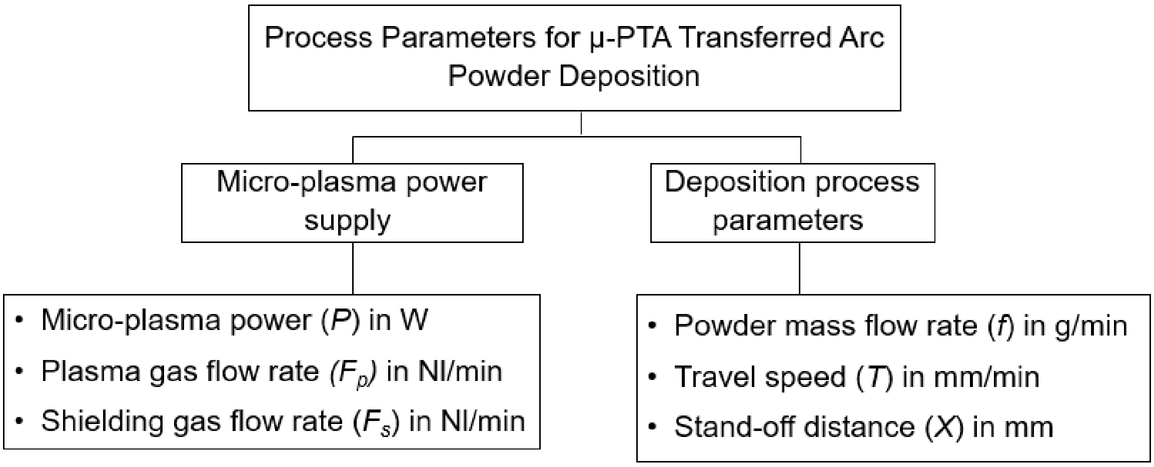

Fig. 3.10: Process parameters of μ-PTA powder deposition process.

Micro-plasma power '*P*' (*W*): It is product of the current and DC voltage supplied for the generation of the plasma. Higher micro-plasma power produces higher heat and melted larger portion of the substrate and deposition material and resulted in higher dilution and larger HAZ. Lower micro-plasma power can lead to partial melting of the powder and poor bonding of the deposition material with the substrate with very smaller dilution. Hence, selection of optimum micro-plasma power is important for continuous and uniform deposition.

Plasma gas flow rate 'F_p' (Normal liter per minute, Nl/min)**:** It is rate at which the plasma forming gas is supplied. Plasma gas helps to transfer the micro-plasma power towards the substrate and maintain a continuous directional flow of the plasma towards the substrate.

Shielding gas flow rate 'F_s' (Normal liter per minute, Nl/min)**:** It is rate at which shielding gas supplied to protect the melt pool from atmospheric contamination. Lower values of the shielding gas flow rate allow the atmospheric gases to react with the melt pool resulting in porous and uneven deposition and producing spatter during the deposition whereas, higher values result in the spread of the of melt pool generating dimple like impression over the top surface of the deposition.

Powder mass flow rate '*f*' (gram per minute): The rate at which powder deposition material is fed to the melt pool. It is an important parameter that determines addition of deposition mass per unit time. It affects the deposition height, dilution and the bonding between the deposited material and the substrate. Powder mass flow rate needs to be chosen in relation to micro-plasma power and relative speed between the deposition head and the substrate.

Travel speed '*T*' (mm/min)**:** It is the relative speed between the deposition head and the substrate material. Sometimes, deposition head is provided the required movement and the substrate remains stationary and, in some case, vice-versa. It decides the addition of deposition mass per unit length and input energy per unit length. It also governs the rate by which a particular deposition is taking place. The travel speed significantly affects the cooling rate and microstructure of the deposition.

Stand-off distance '*X*' (mm): It is the distance between exit of the deposition head and top surface of the substrate on which deposition is taking. It acts as a spark gap in μ-PTAPD process. Higher stand-off-distance (SOD) may discontinue discharge of the plasma-arc between the deposition head and the substrate whereas its lower value restrains furthermore addition of the deposition material.

The most important parameters of the μ-PTAPD process are micro-plasma power, powder mass flow rate and travel speed. Various combinations of these three process parameters produce various deposition rates and deposition tracks. A balanced combination of these parameters is required to obtain good quality of the deposition. In addition to this stand-off distance, plasma gas flow rate and shielding gas flow rate also affect the process performance. Optimized selection of these parameters is necessary in order to achieve continuous and uniform deposition.

3.4 Selection of Materials

Selection criteria and details of the deposition and substrate materials for the coating, additive manufacturing and texturing applications of μ-PTA powder deposition process are described in the following paragraphs.

3.4.1 For Coating by μ-PTAPD Process

Coatings play significant roles to improve performance and life of those parts which operate in adverse environments and require resistance to different types of wear such as fretting, surface fatigue, corrosion, erosion, abrasion, adhesion, and diffusion. Stellite is a cobalt-based alloy which exhibits very good resistance to erosive and corrosive wear particularly, at higher operating temperature due to intermetallic compounds and carbides formed in its coating (Luo et al., 2012). Therefore, Stellite 6 in the powdered form with particle size varying in the range from 50 to 106 μm was selected as the coating material for investigations on coating by μ-PTAPD process. AISI 4310 steel plate having dimensions as 100 mm x 100 mm x 20 mm was chosen as the substrate. It was ground and cleaned using acetone to remove residues before Stellite deposition over it. Table 3.1 presents chemical composition of the selected deposition material and the substrate material.

Table 3.1: Chemical composition (wt. %) of the coating (Stellite 6) and substrate (AISI 4130) material.

Elements	**C**	**Ni**	**Cr**	**Mo**	**V**	**W**	**Mn**	**Si**	**P**	**S**	**Fe**	**Co**
Substrate: AISI 4130 steel	0.3	0.5	0.8	0.15	0.1	-	0.6	0.15	0.04	0.04	Bal.	-
Coating material: Stellite 6	1.2	2.0	28.5	1.0	-	4.6	1.02	1.09	-	-	2.0	Bal.

3.4.2 For Additive Manufacturing by μ-PTAPD Process

Higher strength-to-weight ratio, fracture toughness, excellent biocompatibility, and corrosion resistance of titanium alloys have led to their extensive and varied applications in biomedical, aerospace, power generation, gas turbines, automotive applications (Mahamood and Akinlabi, 2017). Consequently, powder of Ti-6Al-4V having a particle size in the range from 45 to 105 μm was chosen for investigations on additive manufacturing by μ-PTAPD process. Plate made of the same material (Ti-6Al-4V) and having dimensions as 100 mm x 60 mm x 20 mm was chosen as the substrate. The substrate plate was ground and cleaned using acetone before starting deposition over it. Table 3.2 presents composition of the selected substrate and the deposition material used in investigations on the AM by μ-PTAPD process.

Table 3.2: Elemental composition (wt. %) for the substrate (Ti-6Al-4V) and deposition material (Ti-6Al-4V powder).

Elements	Al	V	C	O	N	H	Fe	Cu	Sn	Y	Ti
Substrate: Ti-6Al-4V	6.17	4.02	0.02	0.13	0.022	0.005	0.04	0.12	0.10	0.004	Bal.
Deposition material: Ti-6Al-4V powder	6.21	4.30	0.02	0.12	0.02	0.005	0.05	0.10	0.11	0.005	Bal.

3.4.3 Texturing of Machining Tool by μ-PTAPD Process

Machining of titanium alloys using high speed steel (HSS) tool is difficult due to their lower thermal conductivity which increases the temperature of the machining tool thus accelerating its wear. Texturing on rake face of a machining tool has recently emerged as a promising and environment friendly method to enhance removal of heat from the machining zone (Wei et al., 2017). Therefore, cutting tool made of HSS (grade T-42) was chosen for investigations on spot and dimple-textured by µ-PTAPD process. This tool material is commercially available from Miranda Tools as grade S400 HSS and has a hardness of 65-67 HRC. Stellite exhibits very good resistance to erosive and corrosive wear particularly at higher operating temperature. HSS tool material and Stellite 6 powder have almost similar melting temperature, i.e. 1422 ^oC and 1410 ^oC respectively. Hence, Powder of Stellite 6, having its particle size in a range from 50 to 106 µm, was chosen for spot-texturing of the HSS tool. Spot-textured and dimple-textured and non-textured HSS tools were used in turning of 40 mm diameter cylindrical bar made of Ti-6Al-4V. Table 3.3 presents chemical composition of T-42 grade HSS and Ti-6Al-4V.

Table 3.3: Chemical composition ofT-42 grade HSS tool and Ti-6Al-4V by wt.%.

Chemical composition of T-42 grade HSS tool (wt. %)												
Elements	Co	W	Cr	Mo	V	C	Ni	Si	Mn	P	S	Fe
Composition	9.15	8.68	4.1	3.23	3.12	1.35	0.36	0.22	0.2	0.3	0.35	Bal.
Chemical composition of Ti-6Al-4V (wt. %)												
Elements	Al	V	C	O	N	H	Fe	Cu	Sn	Y	Ti	
Composition	6.17	4.02	0.02	0.13	0.022	0.005	0.04	0.12	0.10	0.004	Bal.	

The ***next chapter*** presents planning and details of the experimental work, evaluation and characterization of the responses as well as results and analyses for the Stellite coating by µ-PTAPD process.

Chapter 4

Investigations on Stellite Coating

This chapter presents planning and details of the experimental work, evaluation and characterization of the responses as well as results and analyses for the Stellite coating. It describes the effect of travel speed of worktable on microstructure, secondary dendritic arm spacing, line scan analysis and microhardness of the Stellite coating. It also presents comparative evaluation of μ-PTAPD, PTAD and laser-based deposition processes in terms of morphology, wear characteristics, and microhardness of Stellite coating.

4.1 Planning and Details of Experimentation

The experimental investigations on Stellite coating were conducted in four stages using the research methodology shown in Fig. 2.4 with objectives to (i) identify optimum values of important parameters of μ-PTAPD process for single-layer multi-track coating of powdered Stellite 6 (with particle size ranging from 50 to 106 μm) on AISI 4130 steel substrate, and (ii) to compare its capabilities with laser-based and PTA-based deposition processes for Stellite coating in terms of dilution, deposition thickness, microstructure, secondary dendritic arm spacing (SDAS), micro-hardness and abrasive wear resistance. All the experiments of all four stages were conducted by mounting the substrate on worktable of a precision knee-type milling horizontal milling machine (model *HF1* from *Bharat Fritz Werner Ltd. Bangalore*) and moving the worktable in X and Y directions. In the 1st stage, pilot experiments were conducted varying six significant parameters of μ-PTAPD process namely micro-plasma power, travel speed of worktable, powder mass flow rate, shielding gas flow rate, plasma gas flow rate and stand-off distance to identify their values for the main experiments which will ensure continuous uniform single-layer single-track deposition of Stellite. The identified values for the main experiments were: 407; 418; and 429 W for micro-plasma power, 80; 100; and 125 mm/min for travel speed of worktable, 1.7; 2.9; and 3.5 g/min for powder mass flow rate, 3.5 Nl/min for shielding gas flow rate, 0.3 Nl/min for plasma gas flow rate and 8 mm for stand-off-distance. Twenty-seven main experiments were performed in the 2nd stage to identify optimum values of micro-plasma power (as 407 W), travel speed of worktable (as 125 mm/min), powder mass flow rate (as 3.5 g/min) using criteria of minimum energy consumption and dilution of single-layer single-track deposition of Stellite by μ-PTAPD process. Four experiments were conducted in the 3rd stage using 10%; 20%; 30%; and 40% overlapping between two successive tracks and using the identified optimum values from the main experiments in single-layer multi-track deposition of Stellite to identify optimum value of the overlapping considering minimum dilution and maximum deposition height as selection criteria. These experiments found 30% overlapping as the optimum value. These identified optimum values were used in 4^{th} stage experimentation to compare the considered characteristics of coatings of Stellite manufactured by µ-PTAPD, Nd-YAG laser-based, and PTA-based deposition processes.

4.1.1 Pilot Experiments for Single-layer Single-track Deposition

Pilot experiments were carried out depositing single-layer single-track of Stellite 6 on AISI 4130 steel substrate by varying the six most influential parameters of µ-PTAPD process namely micro-plasma power, powder mass flow rate, travel speed of the worktable, stand-off distance, plasma gas flow rate and shielding gas flow rate to identify their feasible values for the main experiments. Table 4.1 presents the ranges of the input parameters used in the pilot experiments along with the values identified for the main experiments. It was observed during the pilot experiments that a minimum 407 W of micro-plasma power was required to melt powder of Stellite 6 with a small portion of the substrate during µ-PTAPD process. Therefore, 407; 418; and 429 W (corresponding to current values of 18.5; 19 and 19.5 A) were identified values of micro-plasma power for the main experiments. Powder mass flow rate in the range of 1.7-3.5 g/min and the stand-off-distance (SOD) as 8 mm were identified for the main experiments because it allowed smooth powder feeding to the melt pool through the powder feed nozzle. Discontinuous tracks were observed for the travel speed of worktable more than 125 mm/min while excessive HAZ was observed for worktable travel speed less than 80 mm/min Therefore, 80-125 mm/min was identified for further experiments. Plasma gas flow rate of 0.3 Nl/min was found to be sufficient to transfer the micro-plasma arc toward the substrate, where the shielding gas flow rate of 3.5 Nl/min was found sufficient to protect the melt pool from atmospheric contamination. Based on the pilot experiments, micro-plasma power, powder mass flow rate and travel speed of worktable were identified as most important parameters for the main experiments for Stellite 6 coating on AISI 4130 steel by single-layer single-track deposition.

Table 4.1: Range of the input parameters used in the pilot experiments and identified feasible values for the main experiments on Stellite coating.

Parameters of μ-PTAPD process	Range used in the pilot experiments	Value identified for the main experiments
Micro-plasma power (W)	110 – 440	407; 418; 429
Powder mass flow rate (g/min)	0.6 – 5	1.7; 2.9; 3.5
Travel speed of worktable (mm/min)	40 – 200	80; 100; 125
Plasma gas flow rate (Nl/min)	0.1 – 0.5	0.3
Shielding gas flow rate (Nl/min)	3.0 – 8.0	3.5
Stand-off-distance (mm)	5 – 12	8

4.1.2 Main Experiments for Single-layer Single-track Deposition

Twenty-seven mains were planned and performed using the full factorial approach of a design of experiments depositing single-layer single-track of Stellite 6 on AISI 4130 steel substrate. In these experiments, micro-plasma power, powder mass flow rate and travel speed of the worktable was varied at three levels each while values of other three variables (i.e. plasma gas flow rate, shielding gas flow rate, and SOD) were kept constant using their values mentioned in Table 4.1. The objective was to study effects of the variable parameters on the measured responses (i.e. deposition height and width) and computed responses (i.e. dilution, energy consumption per unit traverse length and power consumption per unit powder mass flow rate). Table 4.2 presents results of main experiments. These experiments identified optimum values of micro-plasma power (as 407 W), travel speed of worktable (as 125 mm/min), and powder mass flow rate (as 3.5 g/min) using criteria of minimum dilution, energy consumption per unit traverse length 'E_l' and power consumption per unit powder mass flow rate 'P_f'.

4.1.3 Experiments for Single-layer Multi-track Deposition

Four experiments were conducted depositing single-layer multi-track (i.e. coating) of Stellite 6 on AISI 4130 steel substrate using 10%, 20%, 30% and 40% as overlapping of between the two successive tracks and using the optimum values of micro-plasma power, travel speed of worktable, and powder mass flow rate (identified from the main experiments). Objective was to identify optimum value of the overlapping using criteria of minimum dilution and maximum deposition height. These experiments identified optimum overlapping between two successive tracks as 30%. Subsequently, three more experiments were conducted to study effects of travel speed of the worktable on microstructure, SDAS, dilution, line scan analysis and microhardness of Stellite coating. In these experiments, travel speed of the worktable was varied at 125, 100, and 80 mm/min at constant values of micro-plasma power (as 407 W) and powder mass flow rate (as 3.5 g/min).

4.1.4 Experiments for Comparative Evaluation of μ-PTAPD process with PTAD and Laser-Based Deposition Processes

Optimum values of (i) plasma gas flow rate (as 0.3 Nl/min), shielding gas flow rate (as 3.5 Nl/min), and SOD (as 8 mm) identified from the pilot experiments, (ii) micro-plasma power (as 407 W), travel speed of worktable (as 125 mm/min), powder mass flow rate (as 3.5 g/min) identified from the main experiments, and (iii) overlapping between two successive tracks (as 30%) identified from the experiments on single-layer multi-track depositions, were used in comparative evaluation of μ-PTAPD process with Nd-YAG laser-based and PTA-based deposition processes terms of morphology, wear characteristics, and microhardness of the Stellite coatings manufactured by them. The parameters used in Nd-YAG laser-based deposition included: power: 2 kW, spot size: 4 mm, travel speed: 480 mm/min, powder mass flow rate: 11 g/min, and overlapping: 30%. The parameters used in PTA-based deposition were: current: 95 A, voltage: 22.5 V, travel speed: 180 mm/min, powder mass flow rate: 21 g/min; plasma gas (argon) flow rate: 2.1 Nl/min, shielding (argon) gas flow rate: 2.5 Nl/min, and overlapping: 30%.

4.2 Evaluation and Characterization of the Responses

Evaluation of various characteristics of the depositions produced by μ-PTAPD process is essential to quantify its performance. It also helps in evaluating the metallurgical relationship between substrate and the deposited material which varies with its parameters. Following paragraphs describe details of the evaluation and characterization of the different responses used in the experimental investigations on Stellite coating by μ-PTAPD process.

4.2.1 Evaluation of Deposition Geometry and Dilution

Samples of the single-layer single-track depositions of Stellite corresponding to 27 main experiments and the single-layer multi-track depositions of Stellite obtained in the comparative evaluation were cut transversely and prepared using the standard metallographic procedure for optical microscopy. Their deposition heights and deposition width were measured using the optical microscope (model Stereo EZ4HD from Leica Inc. Germany). AutoCAD software was used to measure the deposited area 'B' and dilution area 'A' separated by an imaginary fusion line on the deposition profile which was obtained from the optical microscope. Dilution was computed using the measured values of deposited area '*B*' and dilution area '*A*' in Eq. 4.1. Figure 4.1 schematically explains the concept of computation of % dilution for single-layer single-track deposition (Fig. 4.1a) in which entire width of the deposition 'W' was used and for single-layer multi-track deposition (Fig. 4.1b) in which dilution was calculated by taking average of % dilutions of four consecutive widths along the deposition tracks with each width having 5 mm dimension

$$\text{Percentage dilution } = \frac{\mathrm{A}}{(\mathrm{A}+\mathrm{B})} \times 100 \qquad (4.1)$$

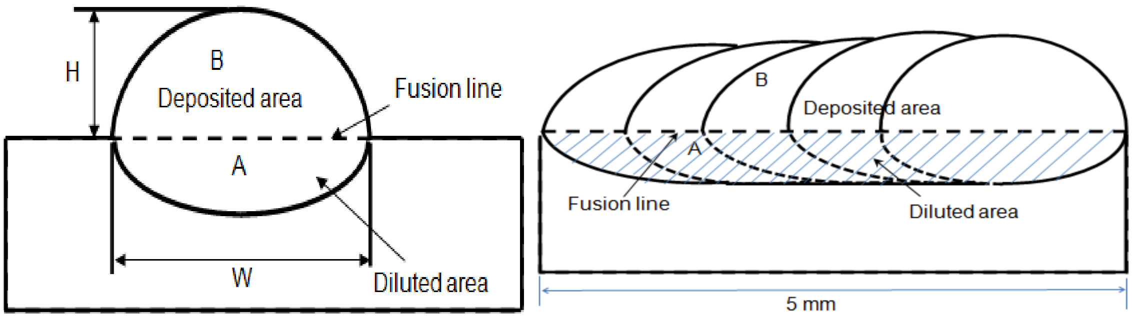

(a) **(b)**

Fig. 4.1: Schematic of concept of the deposited and diluted areas used in computation of percentage dilution for (a) single-layer single-track deposition; and (b) single-layer multi-track deposition.

4.2.2 Characterization of Microstructure and Phase Analysis

Samples of single-layer multi-track depositions (7 samples corresponding to single-layer multi-track deposition experiments and 3 corresponding to comparative evaluation) of Stellite were cut along their cross-section, polished and etched in a solution containing 50 ml water and 50 ml HCl at 70°C temperature for 30 minutes in accordance with the ASTM standard E340-00. The microstructures of some of the prepared samples (leaving the 4 samples corresponding to overlapping experiments) were observed using field emission scanning electron microscope (FE-SEM, Supra 55 from Carl Zeiss GmbH, Germany) and values of SDAS were measured at five different locations for the each sample. Chemical composition of different phases present in a sample was determined by energy dispersive X-ray spectroscopy (EDX). Different phases present in microstructure of Stellite coating and their crystal structure were determined using X-ray diffraction (XRD).

4.2.3 Evaluation of Microhardness

Samples of single-layer multi-track deposition (3 samples corresponding to single-layer multi-track depositions and 3 samples corresponding to comparative evaluation) were cut along their cross-section and then fine polished to measure their microhardness from the deposition to substrate at an interval of 0.1 mm on Vicker's microhardness tester (VMH-002 V from Walter UHL GmbH, Germany) according to the ASTM standard E92-82 using a load of 500 g for duration of 15 seconds.

4.2.4 Evaluation of Wear Characteristics

Micro-scale tribology, abrasion and friction wear properties of the Stellite coating samples (corresponding to comparative evaluation) at low contact stresses with respect to the hard surfaces were studied using pin-on-disk type wear testing machine (Ducom-TR20LE) using 5 mm diameter WC ball having a hardness of 950 HV under the dry condition. Typical applications of dry abrasive wear are: jackhammer, tungsten carbide (WC) cutting tools, down hole hammers, tunnel boring machines, raise boring and construction equipment. Dimensions of the three samples used in the wear tests were 51 mm x 51 mm x 8 mm. Each sample was polished so as to achieve their average surface roughness (R_a) less than 0.8 μm. The sample was rotated at 200 rpm within 15 mm radius thus giving sliding speed of 314 m/s under a normal load of 7 N at room temperature in accordance with the ASTM Standard G99-95a. Wear test for each sample was performed for sliding distance of 200 m; 400 m; and 600 m with three repetitions for each sliding distance wear test. Wear volume was determined by measuring the mass loss of the sample during the wear test using a weight balance having least count of 0.01 mg and dividing it by density of the coating material.

4.3 Results and Analyses

Following paragraphs describes the results obtained in each stage of experimental investigations on Stellite coating by μ-PTAPD process along with their interpretation, analysis and major conclusions.

4.3.1 Analysis of Single-layer Single-track Deposition

Deposition height and width, dilution, energy consumption per unit traverse length 'E_l' (Eq. 4.2) and power consumption per unit powder mass flow rate 'P_f' (Eq. 4.3) have been used to characterize the single-layer single-track depositions of Stellite 6 by conducting 27 full factorial experiments. Table 4.2 presents the measured responses (i.e. deposition height and width) and computed responses (i.e. dilution, energy consumption per unit traverse length and power consumption per unit powder mass flow rate) along with corresponding variable input parameters for all 27 experiments.

$$E_l = \frac{60\ P}{T} (J/mm) \qquad (4.2)$$

$$P_f = \frac{60\ P}{f}\ (J/g) \qquad (4.3)$$

Where, P is micro-plasma power (W); f is powder mass flow rate (g/min); and T is travel speed of worktable (mm/min). Following observations can be made from Table 4.2:

- Higher values of worktable travel speed (i.e. 125 mm/min) and powder mass flow rate (i.e. f = 3.5 g/min) for each value of micro-plasma power have given smaller values of 'E_l', 'P_f' and dilution value in a range of 6.3-7.8 % (experiment no. 9, 18 and 27) whereas their lower values (i.e. 80 mm/min and 1.7 g/min) have yielded larger values of 'E_l', 'P_f' and dilution in a range of 12.7-18.2 % (experiment no. 1, 10 and 19).
- Maximum values of 'E_l', 'P_f' and dilution were found to be 321.7 J/mm; 15,141.1 J/g; and 18.2% respectively in experiment no. 19 having P = 429 W; T = 80 mm/min; and f = 1.7 g/min. It yielded deposition width as 1.96 mm; deposition height as 1.25 mm; and aspect ratio as 1.568.
- Minimum values of 'E_l', 'P_f' and dilution were found to be 195.3 J/mm; 6977.1 J/g; and 6.3% respectively in experiment no. 9 having P = 407 W; T = 125 mm/min; and f = 3.5 g/min. It gave deposition width as 1.7 mm; deposition height as 0.89 mm; and aspect ratio as 1.91. Therefore, these values were identified as their optimum values for further experiments on single-layer multi-track deposition.

Table 4.2: Measured and computed responses for the main experiments along with corresponding variable input parameters.

Exp. No.	Variable input parameters			Measured responses		Computed responses		
	Micro-plasma Power 'P' (W)	Travel speed of worktable 'T' (mm/min)	Mass flow rate of the deposition material 'f' (g/min)	Deposition height (mm)	Deposition width (mm)	Dilution (%)	Energy consumption per unit traverse length (J/mm)	Power consumption per unit powder mass flow rate (J/g)
1	407	80	1.7	1.53	1.91	12.7	305.2	14,364.7
2	407	80	2.9	1.65	2.21	11.8	305.2	8,420.6
3	407	80	3.5	1.71	2.35	10.5	305.2	6,977.1
4	407	100	1.7	0.91	1.93	8.5	244.2	14,364.7
5	407	100	2.9	0.97	2.16	8.4	244.2	8,420.6
6	407	100	3.5	1.10	2.01	7.1	244.2	6,977.1
7	407	125	1.7	0.52	1.71	7.1	195.3	14,364.7
8	407	125	2.9	0.72	1.68	6.9	195.3	8,420.6
9	**407**	**125**	**3.5**	**0.89**	**1.7**	**6.3**	**195.3**	**6,977.1**
10	418	80	1.7	1.41	2.41	14.5	313.5	14,752.9
11	418	80	2.9	1.21	2.5	12.4	313.5	8,648.2
12	418	80	3.5	1.62	2.2	10.7	313.5	7,165.7
13	418	100	1.7	0.97	1.93	9.5	250.8	14,752.9

14	418	100	2.9	1.06	2.15	9.4	250.8	8,648.2
15	418	100	3.5	1.21	1.65	9.2	250.8	7,165.7
16	418	125	1.7	0.54	1.65	8.1	200.6	14,752.9
17	418	125	2.9	0.55	1.69	7.9	200.6	8,648.2
18	418	125	3.5	0.64	1.74	7.0	200.6	7,165.7
19	***429***	***80***	***1.7***	***1.25***	***1.96***	***18.2***	***321.7***	***15,141.1***
20	429	80	2.9	1.29	2.12	17.3	321.7	8,875.8
21	429	80	3.5	1.37	2.28	16.2	321.7	7,354.2
22	429	100	1.7	0.92	2.28	13.8	257.4	15,141.1
23	429	100	2.9	0.97	2.12	12.3	257.4	8,875.8
24	429	100	3.5	1.02	2.3	10.7	257.4	7,354.2
25	429	125	1.7	0.49	1.62	9.1	205.9	15,141.1
26	429	125	2.9	0.53	1.72	9.7	205.9	8,875.8
27	429	125	3.5	0.60	1.75	15.1	205.9	7,354.2

Figures 4.2a-4.2c depict the effect of micro-plasma power (Fig. 4.2a), travel speed of worktable (Fig. 4.2b) and powder mass flow rate (Fig. 4.2c) on the deposition height, deposition width and dilution of single-layer single-track deposition of Stellite. Figure 4.2a shows that increase in micro-plasma power increases the dilution at a faster rate, slightly increases the deposition width, and decreases the deposition height. This can be explained by the fact that an increase in micro-plasma power increases the heat input which increases molten amount of the substrate material consequently size of the melt pool. Figure 4.2b depicts that increase in travel speed of worktable decreases dilution, deposition height and deposition width due to reduction in heat input per unit travel length which consequently reduces the molten amount of the substrate material and size of the melt pool. It also decreases amount of the powder deposited per unit travel length reducing deposition height and deposition width. Figure 4.2c illustrates that deposition height and deposition width increases with increase in mass flow rate of the deposition material whereas dilution decreases with it. This is due to the fact that higher powder mass flow rate increases molten amount the deposition material which increases height and width of deposition but decreases the amount of the molten substrate material. This study concludes that travel speed of worktable is the most influential parameter that significantly affects the deposition height, deposition width and dilution (all three decreases with it) for the single-layer single-track depositions.

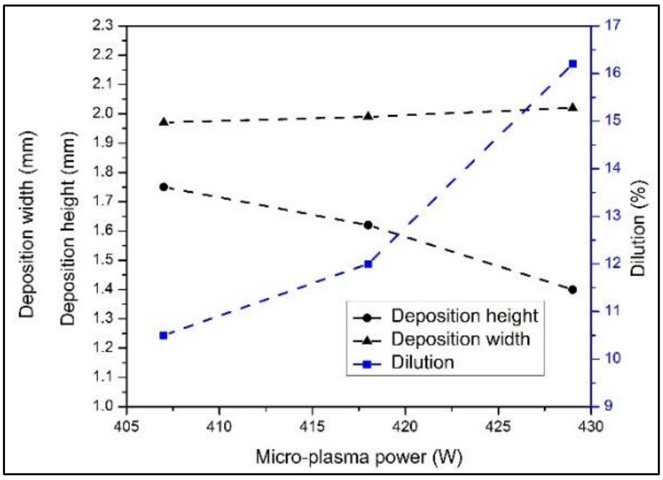

(a)

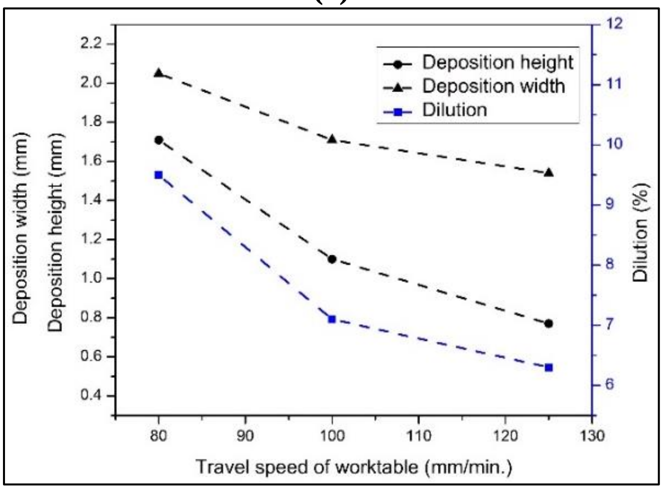

(b)

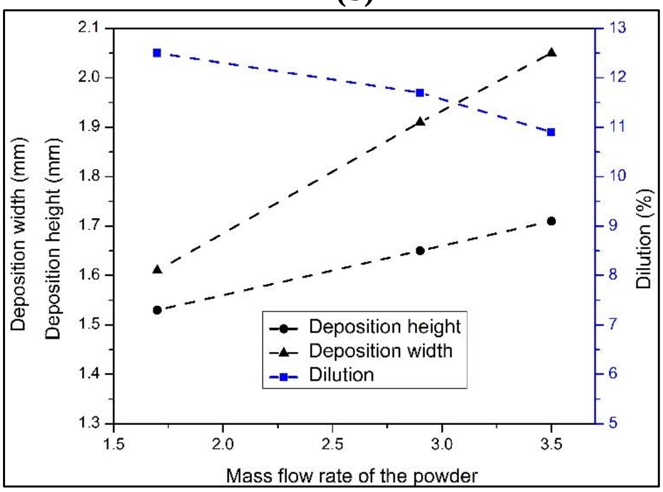

(c)

Fig. 4.2: Effect of (a) micro-plasma power; (b) travel speed of worktable; and (c) powder mass flow rate; on deposition height, deposition width and dilution for the single-layer single-track depositions of Stellite by μ-PTAPD process.

4.3.2 Analysis of Single-layer Multi-track Deposition

The effect of overlapping, microstructure and phase analysis as well as travel speed of work table on single-layer multi-track deposition were studied and discussed in following paragraphs.

4.3.2.1 Effect of Overlapping

Single-layer multi-track deposition involves certain overlapping between two successive tracks to ensure good quality of deposition. Single-layer multi-track depositions of Stellite were done using overlapping values of 10%, 20%, 30% and 40% and using the identified optimum values of *P*, *T* and *f* corresponding to experiment no. 9. Figure 4.3 shows effect of overlapping on the deposition height and dilution. It can be seen that deposition height increases with increase in overlapping whereas its dilution decreases with it. This can be explained by the fact that higher value of overlapping causes each succeeding track to overlap the previous track by higher amount which increases the height of the single-layer multi-track deposition but decreases molten amount of the substrate material thus reducing dilution. It can also be observed from Fig. 4.3 that overlapping values of 10% and 20% give dilution values around 10% and lower deposition height whereas, overlapping values of 30% and 40% give dilution approx. 6% and higher deposition height. Since, higher overlapping value increases the number of tracks to be deposited per unit width of the substrate material therefore, 30% overlapping was identified as its optimum value for further experiments on single-layer multi-track deposition of Stellite by μ-PTAPD process.

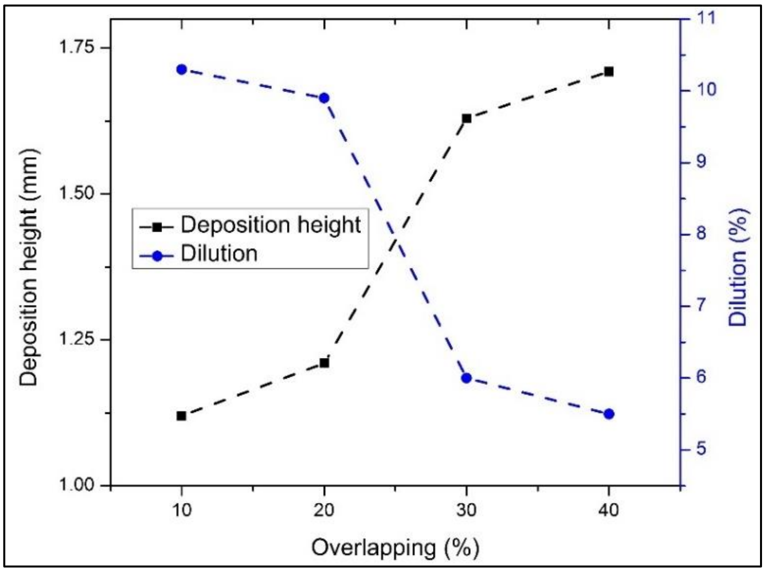

Fig. 4.3: Effect of overlapping on deposition height and dilution of single-layer multi-track deposition Stellite by μ-PTAPD process.

4.3.2.2 Microstructure and Phase Analysis

Microstructure of Stellite coating sample obtained using parameters of Exp. 9 of Table 4.2 and overlapping value 30% is shown in Fig. 4.4 in which presence of different phases and their crystal structure were determined using XRD (presented in Fig. 4.5) and their elemental composition using EDX (shown in Figures 4.6a to 4.6c).

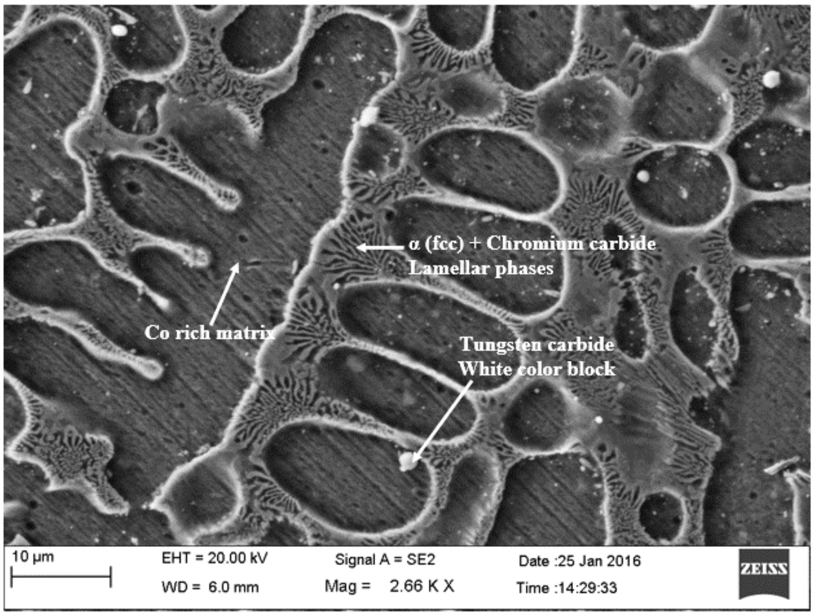

Fig. 4.4: Microstructure of the Stellite coating (obtained using identified optimum values of μ-PTAPD process parameters and overlapping value 30%) and the different phases identified from XRD.

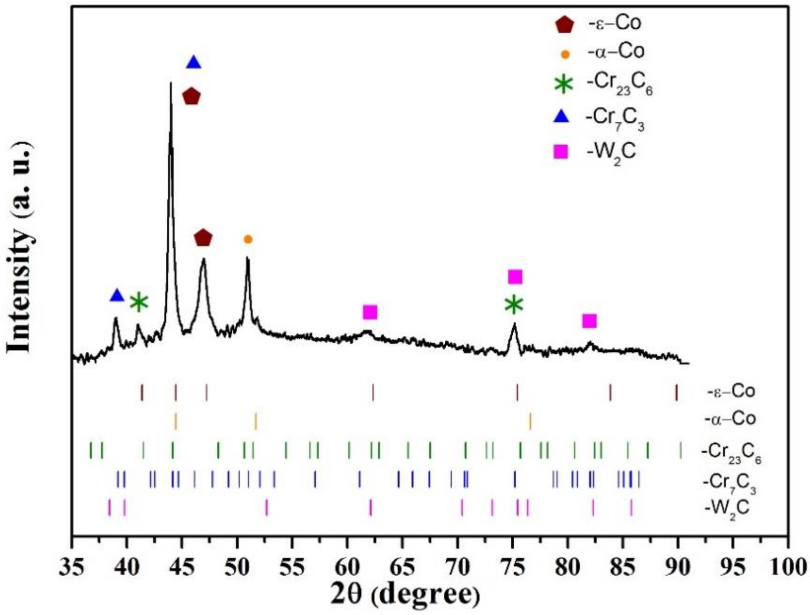

Fig. 4.5: XRD pattern showing different phase present in the Stellite coating ((obtained using identified optimum values of μ-PTAPD process parameters and overlapping value 30%).

Using results of XRD and EDX, it can be seen in Fig. 4.4 that microstructure of the Stellite coating consists of cobalt rich matrix (appearing in black colour) as primary phase formed during cooling of the molten Stellite along with carbides (seen as lamellar phases on the grain boundaries) and inter-dendritic phases (seen as white colour blocks). Fig. 4.5 shows XRD pattern and peak positions of different phases revealing that presence of ε-Co having hexagonal close-packed (HCP) crystal structure, α-Co having face centred cubic (FCC) crystal structure and carbides such as $Cr_{23}C_6$, Cr_7C_3 and W_2C. It can be observed in Fig. 4.6a that microstructure of black coloured matrix mainly consists of Co-rich solid solution which has very high wt. percentage of cobalt followed by chromium, tungsten, iron and silicon. The lamellar phases on the grain boundaries consist of relatively higher wt. percentage of chromium as shown in Fig. 4.6b. While, the phases appearing in white colour blocks had the highest wt. percentage of chromium followed by cobalt, tungsten and iron as depicted in Fig. 4.6c. Combining results of EDX and XRD helps in concluding that high concentration of cobalt rich matrix is related to peaks of ε-Co and α-Co phases which is due to alloying elements nickel and iron which decrease the transformation temperature and stabilize the FCC containing cobalt phase (i.e. α-Co), while molybdenum and tungsten tend to increase the transformation temperature of HCP crystal structure containing cobalt phase (i.e. ε-Co) (Motallebzadeh et al., 2015). Therefore, due to sluggish transformation during cooling, it consists of the mixture of (ε-Co) and metastable (α-Co) at room temperature. The peaks of $Cr_{23}C_6$ and Cr_7C_3 carbide are associated with lamellar phases of the microstructure while peaks of tungsten carbide (W_2C) are related to white colour blocks. The presence of carbide phases on grain boundaries imparts Stellite coating more resistant to wear and corrosion (Jeshvaghani et al., 2011).

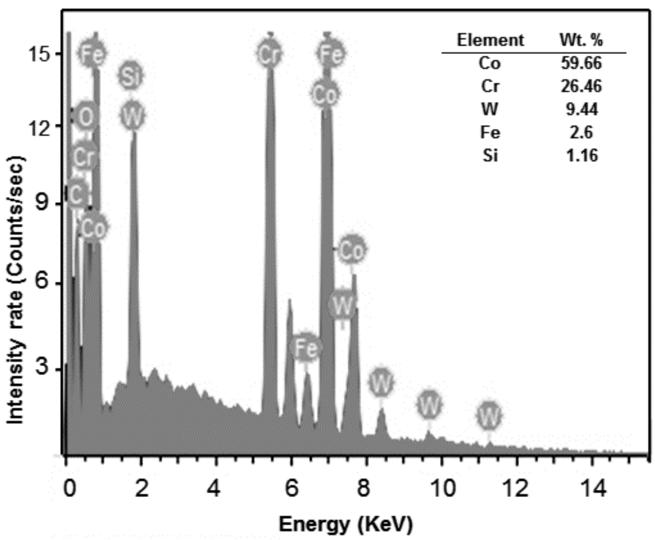

(a)

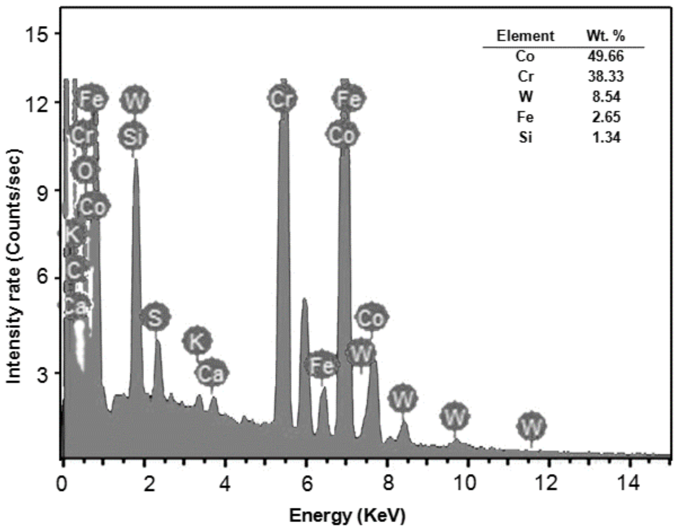

(b)

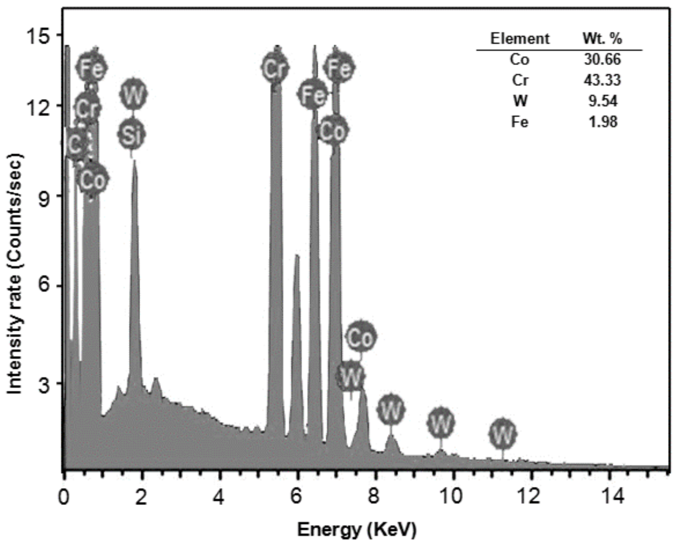

(c)

Fig. 4.6: EDX analysis of (a) black coloured matrix; (b) lamellar phases on the grain boundaries; and (c) phases appearing in white colour blocks, in in the Stellite coating (obtained using identified optimum values of μ-PTAPD process parameters and overlapping value 30%).

4.3.2.3 Effect of Travel Speed

Travel speed of worktable was found to be the most influential parameter affecting the characteristics of single-layer single-track depositions. It can also be observed from Table 4.2 that (i) minimum dilution of 6.3% is obtained in experiment no. 9 having plasma power as 407 W; worktable travel speed as 125 mm/min; and powder mass flow rate of 3.5 g/min; (ii) maximum deposition height is obtained in experiment no. 3 having plasma power as 407 W; worktable travel speed as 80 mm/min; and powder mass flow rate as 3.5 g/min; and (iii) average of maximum and minimum width is obtained in experiment no. 6

having plasma power as 407 W; worktable travel speed as 100 mm/min. Therefore, experiments 3, 6 and 9 having travel speeds as 80, 100 and 125 mm/min respectively with constant micro-plasma power and powder mass flow rate were selected to study effect of travel speed of the worktable on microstructure, SDAS, line scan analysis and microhardness of single-layer multi-track deposition of Stellite.

4.3.2.3.1 Microstructures of the Interface and SDAS

Figures 4.7a to 4.7c present microstructure of the interface between Stellite coating and AISI 4130 steel substrate obtained using travel speeds of worktable as 80, 100 and 125 mm/min respectively. These images reveal that coated layer formed an excellent metallurgical bond with the substrate free from defects such as cracks and porosity and having a uniform microstructure comprising of nearly vertical orientation of columnar dendrites which corresponds to the growth of crystal direction during solidification.

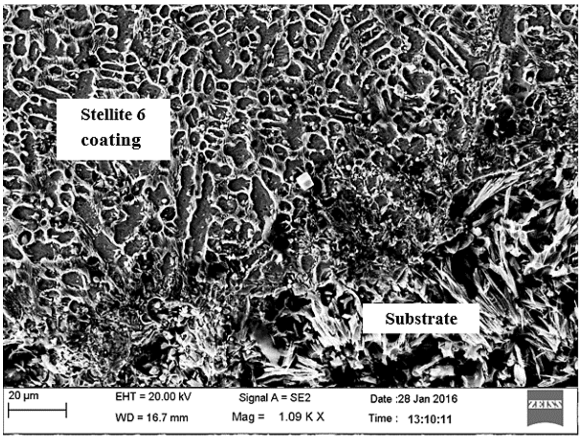

(a)

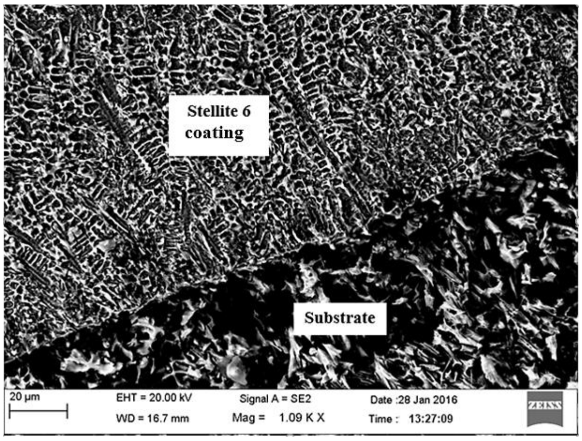

(b)

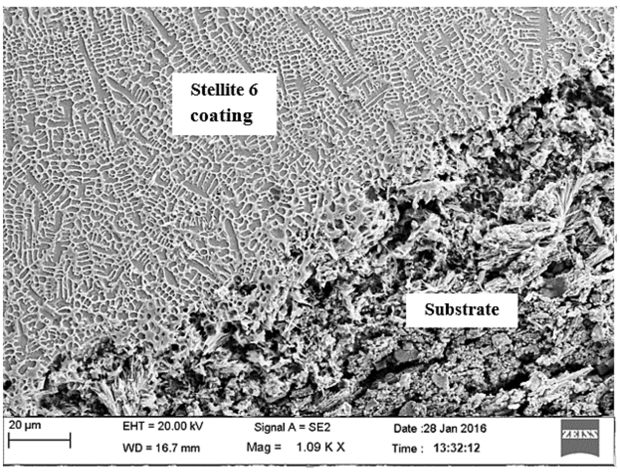

(c)

Fig. 4.7: Microstructures of interface between Stellite coating and AISI 4130 steel substrate at worktable travel speed of (a) 80 mm/min; (b) 100 mm/min; and (c) 125 mm/min.

Values of SDAS and cooling rate 'R' ($^oC/s$) computed using Eq. 4.4 (Zhong et al., 2002) also explain the observed dendritic structure of the different coatings obtained using different values of worktable travel speed. It can be observed from the values mentioned in Table 4.3 that (i) there is an inverse relationship between cooling rate of coating and SDAS, (ii) higher travel speed of worktable (i.e. 125 mm/min) produced smaller SDAS value (1.74 µm) resulting much finer carbide dispersion in dendrite due to higher cooling rate, and (iii) lower travel speed worktable (i.e. 80 mm/min) produced higher SDAS value (2.44 µm) resulting coarser dendritic structure due to higher heat input during deposition.

$$R = \left[\frac{32.8}{\lambda}\right]^3 \tag{4.4}$$

where, λ is secondary dendritic arm spacing (µm), R is Cooling rate ($^oC/s$).

Table 4.3: Mean values of secondary dendritic arm spacing (SDAS) for Stellite coating at different travel speed of worktable.

Travel speed of worktable (mm/min)	Mean value (standard deviation) of secondary dendritic arm spacing 'λ' (µm)	Cooling rate 'R' ($^oC/s$)
125	1.74 (0.079)	6.69×10^3
100	2.10 (0.16)	3.81×10^3
80	2.44 (0.32)	2.42×10^3

4.3.2.3.2 Line Scan Analysis

Line scan analysis was done to investigate change in wt.% of iron from the substrate to coating material at different values of worktable travel speed and its results are shown graphically in Fig. 4.8. It can be observed from this graph that (i) wt.% of iron decreases from substrate to coating for all the values of worktable travel speed confirming that wt.% of iron in substrate is barely transferred to the Stellite coating, (ii) higher worktable travel speed (i.e. 125 mm/min.) gave minimum wt.% of iron in the Stellite coating whereas it gave maximum iron content in the substrate, (iii) lower worktable travel speed (i.e. 80 mm/min.) gave maximum wt.% of iron in the Stellite coating whereas it gave minimum iron content in the substrate. This can be explained by the fact that lower travel speed of worktable increases heat input energy per unit length which increases stirring effect in the melt pool causing diffusion of iron from the substrate to the coating material. This reduces hardness, wear resistance and corrosion resistance of the Stellite coating (Liu et al., 2015). It is generally recommended to minimize the dilution in Stellite coatings because metallurgical bonding with minimum dilution helps in maintaining original properties of the coating material.

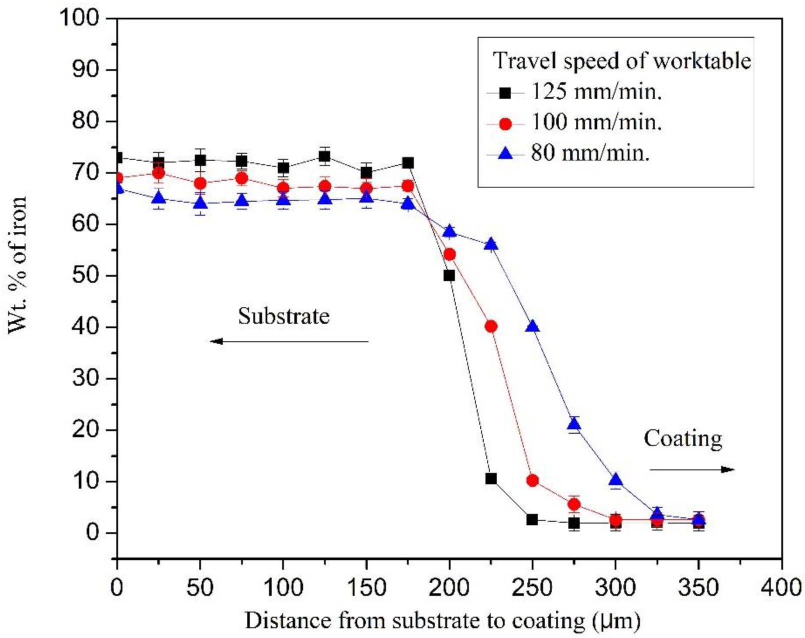

Fig. 4.8: Results of line scan analysis showing change in wt. % of iron from the substrate to Stellite coating at different values of travel speed of worktable.

4.3.2.3.3 Microhardness

Fig. 4.9 shows the microhardness profile of Stellite coatings at different values of the travel speed of worktable. It can be observed from this figure that (i) microhardness of Stellite coating is much higher than the substrate for all the values of worktable travel speed, (ii) higher travel speed of worktable (i.e. 125 mm/min) resulted in higher microhardness of Stellite coating and lower microhardness of substrate whereas opposite trend is obtained for lower travel speed of worktable (i.e. 80 mm/min), (iii) average values of microhardness of Stellite coating are 558 HV, 533 HV, and 513 HV at 125, 100, and 80 mm/min worktable travel speed respectively, and (iv) microhardness of coating at a particular value of worktable travel speed is almost constant confirming that the microstructure is uniform throughout the coating. These observations can be explained by the facts that (i) higher travel speed of worktable (i.e. 125 mm/min) results in minimum dilution (i.e. 6.3%) and finer carbides giving higher value of microhardness whereas lower travel speed of worktable (i.e. 80 mm/min) results in higher dilution (i.e. 10.5%) due to higher heat input causing formation of coarser carbides (ii) formation of very hard carbide phases such as $Cr_{23}C_7$, Cr_7C_3 and W_2C imparts higher microhardness to Stellite coating as compared to the substrate.

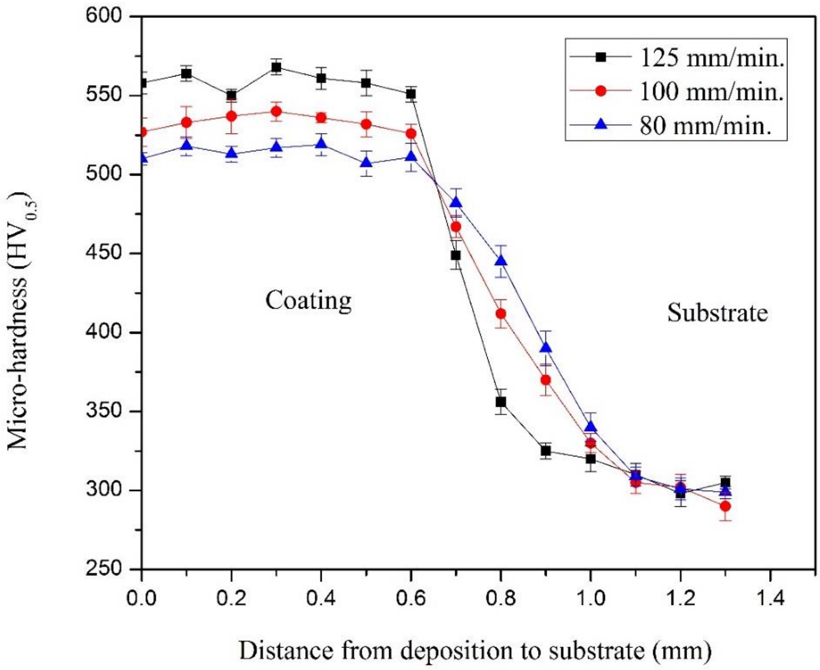

Fig. 4.9: Microhardness profile of Stellite coatings at different values of travel speed of worktable.

4.3.3 Concluding Remarks

Following concluding remarks can be made from the experimental investigations on single-layer single-track and single-layer multi-track depositions of Stellite by μ-PTAPD process:

- Micro-plasma power of 407 W; worktable travel speed of 125 mm/min.; and powder mass flow rate of 3.5 g/min gave minimum energy consumption per unit traverse length (195.3 J/mm), power consumption per unit powder mass flow rate (6977.1 J/g) and dilution (6.3%) in single-layer single-track deposition of Stellite. These were identified as their optimum values for further experiments on single-layer multi-track deposition of Stellite.
- For single-track deposition of Stellite (i) deposition height decreases with increase in micro-plasma power and worktable travel speed while increases with powder mass flow rate; (ii) deposition width decreases with increase in worktable travel speed, increases with powder mass flow rate and not affected by micro-plasma power; (iii) dilution increases with micro-plasma power and decreases with increase in worktable travel speed and powder mass flow rate.
- Deposition height of multi-track increases with overlapping but its dilution decreases with it. Overlapping value of 30% was found as optimum for multi-track deposition of Stellite.

- Phase analysis of Stellite coating revealed that primary phase consists of cobalt matrix consisting of ε-Co and α-Co having HCP and FCC crystal structure respectively mixed with chromium-rich carbides ($C_{r23}C_6$, $C_{r7}C_3$), and tungsten containing complex carbides (W_2C)
- Travel speed of worktable found to be the most important parameter affecting the characteristics of Stellite coating.
- Stellite coating using higher value of travel speed of worktable had smaller SDAS value, lower iron content and higher microhardness due to higher cooling rate and consequently formation of finer carbides.
- Stellite coating using lower travel speed of worktable yielded larger SDAS value, higher iron content and lower microhardness due to lower cooling rate and consequently formation of coarser carbides.

4.4 Comparative Evaluation of μ-PTAPD, PTAD and Laser-based Processes for Stellite Coating

The main objective of this comparative evaluation was to study capabilities of μ-PTAPD process, PTAD process, and Nd-YAG laser-based deposition process in terms of dilution, deposition thickness, microstructure, SDAS, micro-hardness and wear resistance for manufacturing Stellite coating for different wear resistant applications.

4.4.1 Morphology

Figure 4.10 presents the optical microscopic images of Stellite coating on AISI 4130 steel substrate manufactured by μ-PTAPD (Figure 4.10a), laser-based deposition (Figure 4.10b) and PTAD (Fig. 4.10c) in which microstructure of Stellite coating, heat affected zone (HAZ) and substrate material can be seen. The optical images of μ-PTAPD (Figure 4.10a) and laser-based deposition (Figure 4.10b) reveal that the Stellite coating has a good surface appearance, smaller HAZ, excellent metallurgical bond with the substrate and free from the defects such as cracks and porosity. In contrast, optical images of the Stellite coating by PTAD process (Figure 4.10c) shows presence of porosity and cracks in the coating which may be due to trapped gasses and varying contraction during the solidification. It also indicates larger HAZ which is caused by more amount of heat input used in PTAD process.

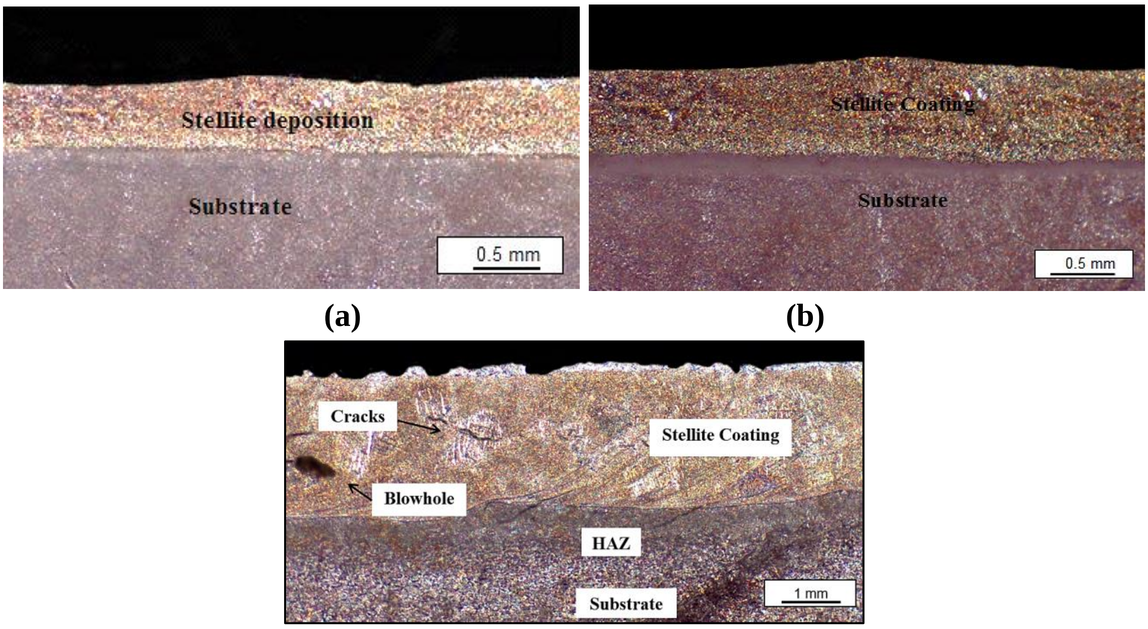

(c)

Fig.4.10: Optical micrographs showing cross-section of the coatings of Stellite6 manufactured by (a) μ-PTAPD; (b) laser-based deposition; and (c) PTAD processes.

Figures 4.11a-4.11c depict the SEM images of the Stellite coatings by the considered deposition processes showing microstructure of the interface between Stellite coating and AISI 4130 steel substrate. It can be observed from these figures that the Stellite coatings have a uniform dendritic microstructure consisting of nearly vertically oriented columnar dendrites which corresponds to growth of the crystal direction during the solidification process. Table 4.4 presents the SDAS values, cooling rates, dilutions and thickness of Stellite coatings manufactured by the considered deposition processes. Values of SDAS and cooling rate 'R' (^{o}C/s) also explain the observed dendritic structure of the Stellite coatings. It can be observed that SDAS value of the coating by μ-PTAPD process (1.74 μm) is almost same as that obtained by laser-based deposition process (1.72 μm) which is much smaller than that obtained by PTAD process (6.79 μm). Smaller SDAS values by laser-based deposition and μ-PTAPD processes result in finer dendritic structure than PTAD because of faster cooling rate in μ-PTAPD (6.69 x 10^3) and laser-based deposition (6.93 x 10^3) processes. Similar SDAS values for PTAD and laser-based deposition processes have also been presented by d'Oliveira et al. (2002). Comparison of dilution values shows that μ-PTAPD (6.3%) and laser-based deposition (5.8%) have very smaller dilution as compared to PTAD (21.5%). This can be explained by the fact that higher heat input in the PTAD increases amount of molten substrate material and consequently size of the melt pool which leads to higher distortion and higher HAZ. Thickness of Stellite coatings manufactured by µ-PTAPD (0.7 mm) and laser-based deposition (0.9 mm) processes are smaller than that given by PTAD process (2.6 mm). It shows that PTAD process has higher deposition efficiency but slows down the solidification rate leading to a less efficient heat flow through the substrate. Higher thickness of coating increases the coating cost in wear and corrosion resistant applications where strong bond of thin coating with the substrate is required.

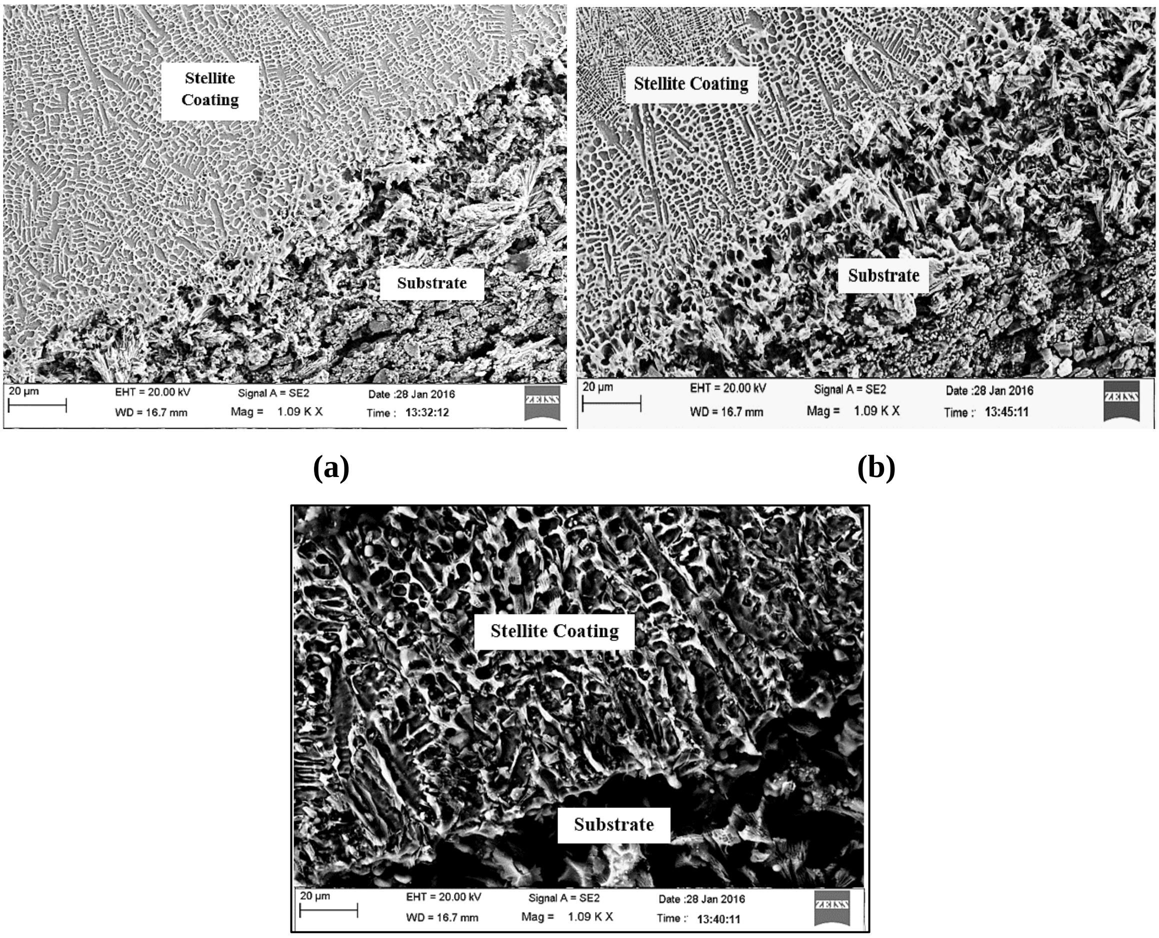

(a) **(b)**

(c)

Fig. 4.11: SEM images showing microstructures of the interface between the AISI 4130 steel substrate and coatings of Stellite 6 manufactured by (a) µ-PTAPD; (b) laser-based deposition; and (c) PTAD processes.

Table 4.4: Mean values of SDAS, cooling rate, dilution and coating thickness for different processes of Stellite coating.

Process name	Mean value (standard deviation) of SDAS 'λ' (µm)	Cooling rate 'R' (^{0}C/s)	Dilution (%)	Mean value of the coating thickness (mm)
µ-PTAPD	1.74 (0.074)	6.69×10^3	6.3	0.7
Laser-based deposition	1.72 (0.069)	6.93×10^3	5.8	0.9
PTAD	6.79 (0.097)	1.12×10^2	21.5	2.6

4.4.2 Microhardness

Figure 4.12 shows the microhardness profile of Stellite coatings obtained by µ-PTA powder deposition, laser deposition and PTAD processes. Microhardness profile can be divided into three regions: Stellite coating, interface and substrate. It can be observed from this figure that average values of microhardness of Stellite coating are 553 HV, 551 HV and 501 HV for µ-PTAPD, laser-based deposition and PTAD processes respectively. It means that the Stellite coatings by µ-PTAPD and laser-based deposition processes have an almost similar value of microhardness which is much higher than that of the coating manufactured by PTAD process. These observations can be explained by the fact that higher cooling rate in µ-PTAPD and laser-based deposition processes results in minimum dilution and finer carbides giving higher values of microhardness whereas lower cooling rate due to higher heat input in the PTAD process which results in higher dilution (i.e. 21.5%) and formation of coarser carbides. It can also be observed from Fig. 4.12 that there is a significant improvement in Stellite coating as compared to the substrate due to formation of very hard carbide phases such as $Cr_{23}C_7$, Cr_7C_3 and W_2C which impart higher hardness. Microhardness profile also shows that there is a sharp decrease in microhardness at interface of Stellite coatings manufactured by µ-PTAPD and laser-based deposition processes as compared to coating manufactured by PTAD process which implies existence of small diluted region at the interface of coating and substrate in the Stellite coatings manufactured by µ-PTAPD and laser-based deposition processes.

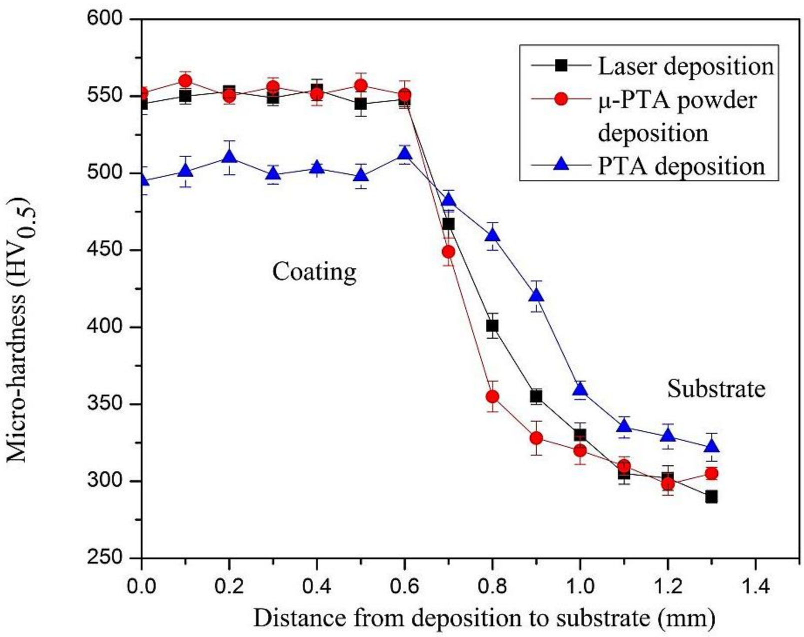

Fig. 4.12: Microhardness profile of the coatings of Stellite 6 manufactured by µ-PTA powder deposition, laser-based deposition and PTAD processes.

4.4.3 Wear Characteristics

Two-body and three-body wear causes different wear mechanisms such as micro-cutting, micro-ploughing, micro-cracking or micro-fatigue in the abrasive wear of the coatings. It is a complex phenomenon and depends on many factors including hardness, cyclic stress and surface topography of the coating material. Figures 4.13a-4.13c and 4.14a-4.14c present variation of wear volume and coefficient of friction respectively with the sliding distance and Figs. 4.15a-4.15c depict SEM images showing wear mechanism for the coatings of Stellite 6 manufactured by μ-PTAPD, laser-based deposition and PTAD processes. Following observations can be made from these figures:

- Coatings manufactured by laser-based deposition and μ-PTAPD processes have lower wear volume than the coating manufactured by PTAD process for all the values of the sliding distance (Fig. 4.13). This result can be correlated to the results of microstructure (Fig. 4.11), dilution (Table 4.4) and microhardness (Fig. 4.12). It shows that formation finer carbides, lower dilution and higher micro-hardness of Stellite coatings exhibit lower wear volume.
- Wear volume of the coating manufactured by PTAD process increases drastically after 400 m sliding distance due to extensive ploughing of the coating material (Fig. 4.15c).
- It can be seen from the graphs of coefficient of friction for the coatings manufactured by μ-PTAPD (Fig. 4.14a) and laser-based deposition (Fig. 4.14b) processes that their values of coefficient of friction remain constant in range 0.25-0.35 with minor variations over the entire sliding distance. This will result in less frictional resistance by the coatings and smooth motion of any surface against them. The SEM images shown in Figs. 4.15a and 4.15b indicate that wear of Stellite coatings manufactured by these processes takes place by micro-ploughing which forms very shallow grooves and brittle micro-cutting (only in case of μ-PTAPD) leading to very less wear debris which implies better wear resistance of the coatings.
- Graph of coefficient of friction for the PTAD manufactured coating (Fig. 4.14c) shows many irregular fluctuations with comparatively very high mean value of coefficient of friction and its wear shown in Fig. 4.15c indicates formation of deep grooves by repetitive ploughing and eventually breaking of these edges during the wear test. This is suggestive of three-body abrasive wear during relative motion of any surface against this coating by entrapment of some wear debris.

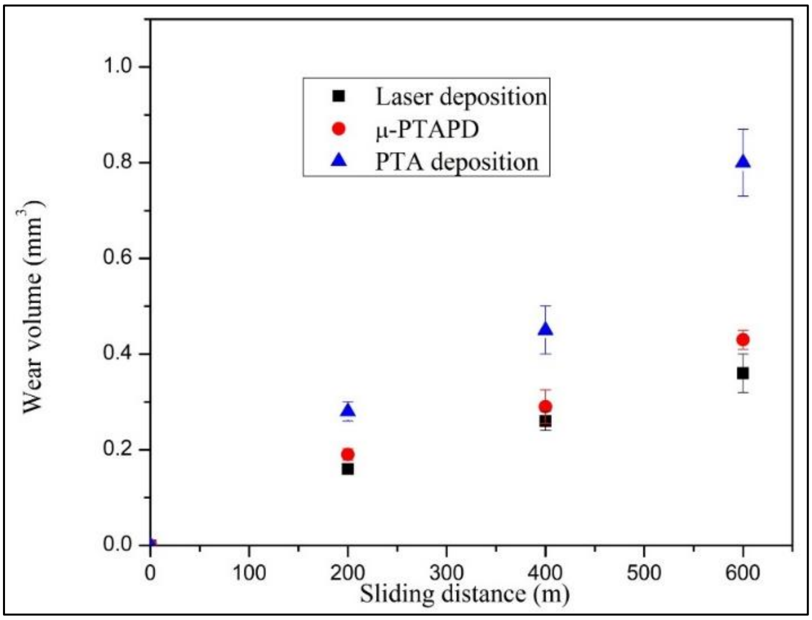

Fig. 4.13: Variation of wear volume with the sliding distance for the coatings of Stellite 6 manufactured by μ-PTAPD, laser deposition and PTAD processes.

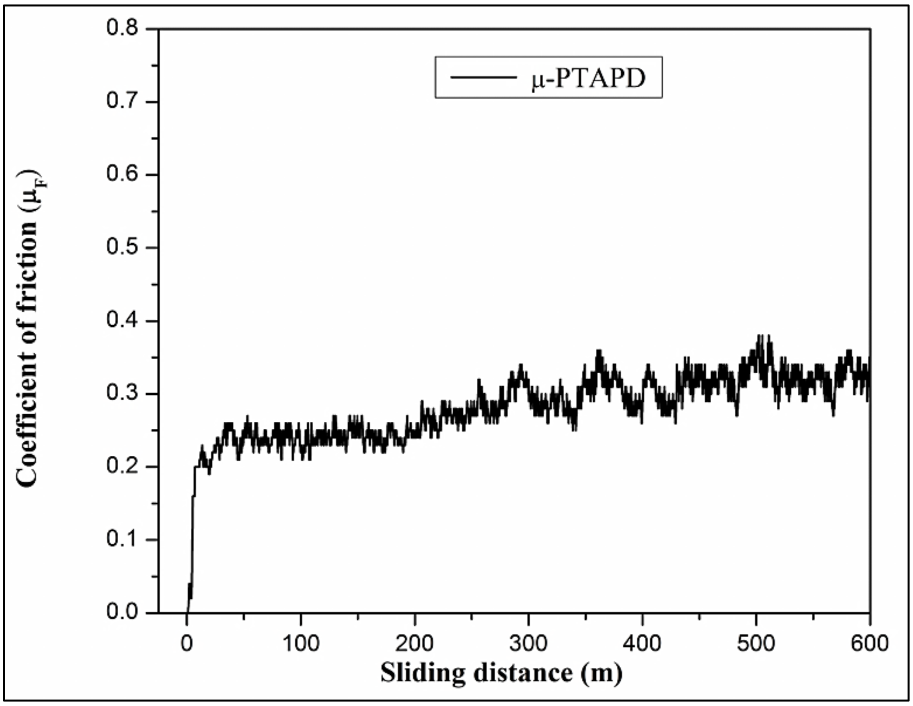

(a)

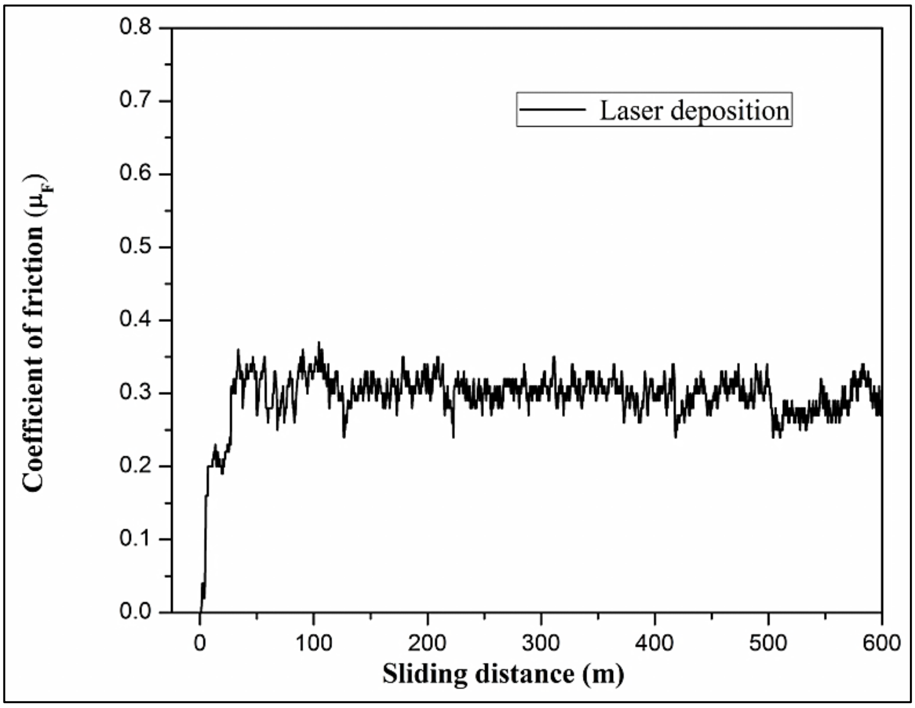

(b)

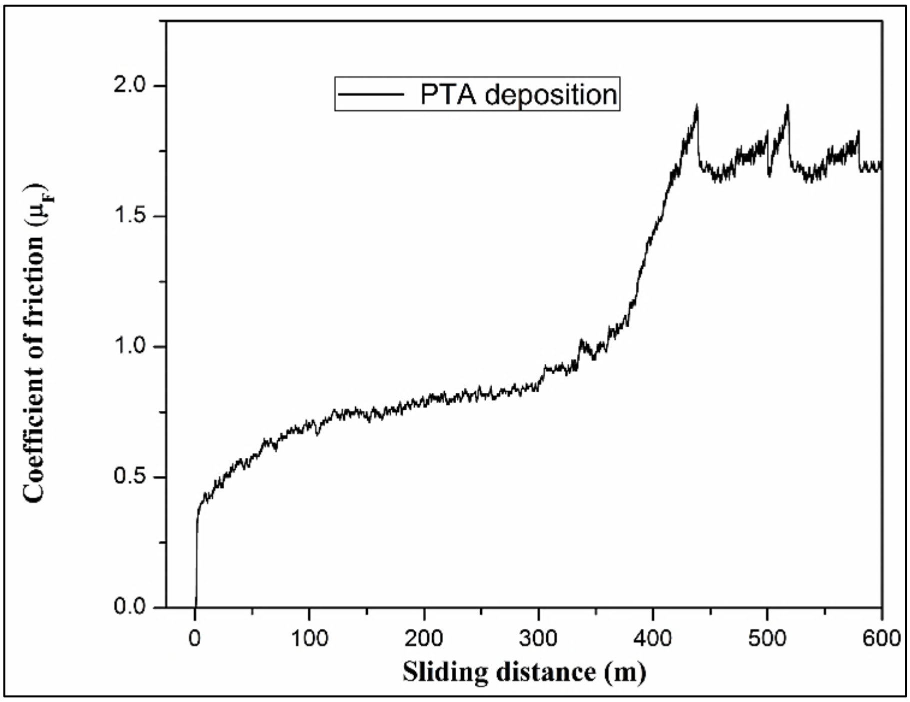

(c)

Fig. 4.14: Variation of coefficient of friction with sliding distance for Stellite 6 coatings manufactured by (a) μ-PTAPD; (b) laser-based deposition; and (c) PTAD processes.

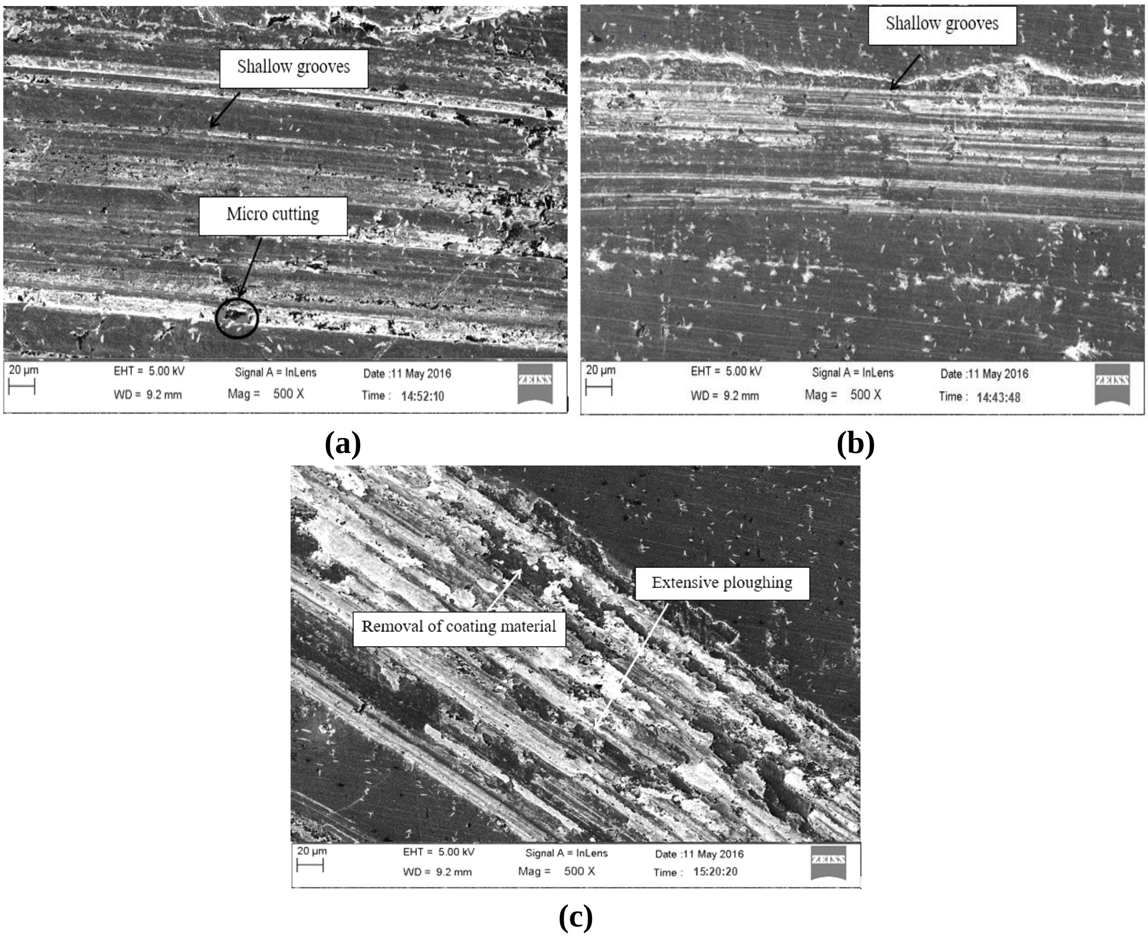

Fig. 4.15: SEM images showing wear mechanism of various Stellite coatings manufactured by (a) µ-PTAPD; (b) laser-based deposition; and (c) PTAD processes.

Figures 4.16a, 4.16b and 4.16c present the 3D surface profiles of the wear tracks on the Stellite coatings manufactured by µ-PTAPD, laser-based deposition and PTAD processes respectively. These images help to understand those aspects of wear of the coatings which cannot be indicated by 2D microscopic images of top surfaces of the wear tracks. Wear tracks on the coatings manufactured by µ-PTAPD (Fig.4.16a) and laser-based deposition (Fig.4.16b) are smaller and shallower (having depths of approximately 5 µm and 4.8 µm respectively which is shown along the vertical axis). It signifies less loss of coating material due to abrasive wear which implies harder coating. Wear track on Stellite coating manufactured by PTAD process (Fig. 4.16c) is longer and deeper (depth approximate 9 µm) indicating more loss of coating material by abrasive wear which means softer coating.

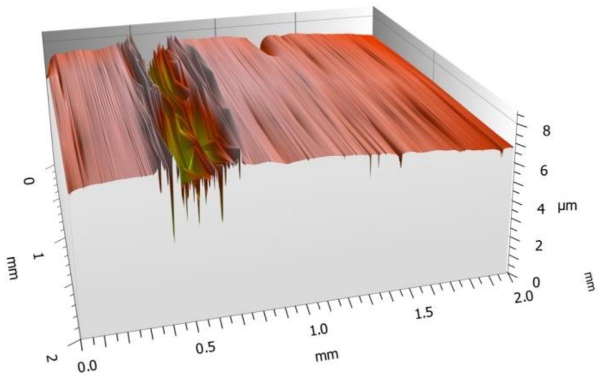

(a)

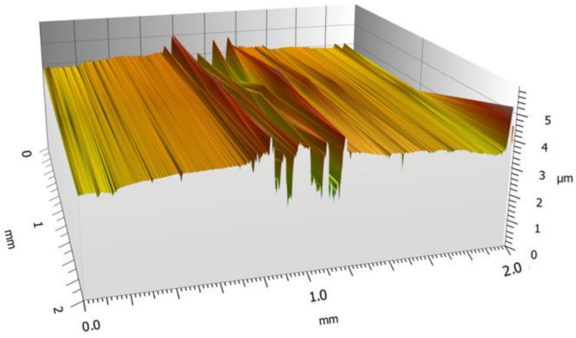

(b)

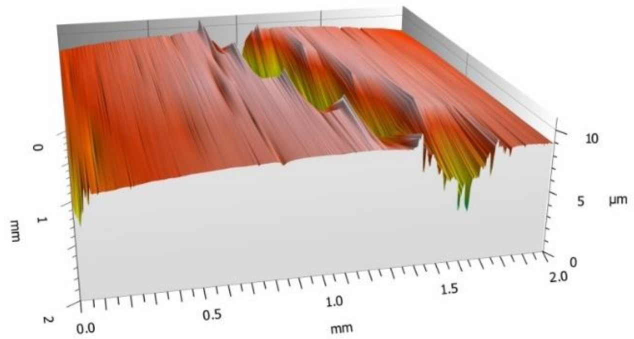

(c)

Fig. 4.16: Three-dimensional surface profiles of the wear tracks formed during abrasive wear test on the Stellite coatings manufactured by (a) μ-PTAPD; (b) laser-based deposition; and (c) PTAD processes.

4.4.4 Concluding Remarks

Following concluding remarks can be made from comparative evaluation of μ-PTAPD, laser-based deposition; PTAD processes for Stellite coating:

- Stellite coating manufactured by μ-PTAPD and laser-based deposition processes had smaller HAZ, absence of defects and finer dendritic structure with smaller SDAS value than the coating manufactured by PTA deposition.
- μ-PTAPD and laser-based deposition processes are capable of manufacturing thin coatings of less than 1 mm with lower dilution. It is suitable for wear and corrosion resistant applications where strong bond of thin coating with the substrate material is required.
- Stellite coating manufactured by μ-PTAPD process had almost similar value of average microhardness (553 HV) that manufactured by laser-based deposition (551 HV) and much higher than the coating manufactured by PTAD process (501 HV).

- Stellite coating by μ-PTAPD and laser-based deposition result in a relatively stable coefficient of friction with considerably minor variations and wear of Stellite coating by very shallow grooves while PTAD shows irregular fluctuations with higher coefficient of friction and wear of coating material by extensive ploughing.
- Stellite coating by μ-PTAPD and laser-based deposition processes exhibited lower wear volume than PTA deposition.
- This proves that μ-PTAPD process has the capability to provide advantages of the laser-based deposition for Stellite coating at much lower cost and higher energy and material efficiency.

The ***next chapter*** presents planning and details of the experimental work, evaluation and characterization of the responses as well as results and analyses for the additive manufacturing of titanium alloy by μ-PTAPD process.

Chapter 5

Investigations on AM of Titanium Alloy Component

This chapter presents planning and details of the experimental investigations, evaluation and characterization of the responses as well as results and analyses for the additive manufacturing of titanium alloy by μ-PTAPD process. It describes the effect of input process parameters on single-layer single-track deposition characteristics such as deposition height, deposition width, power consumption per unit mass flow rate of powder and energy consumption per unit traverse length. It also presents details of the characterization and analyses of multi-layer single-track deposition of Ti-6Al-4V by continuous and dwell modes. It ends with comparison of performance of μ-PTAPD with other existing AM processes.

5.1 Planning and Details of Experimentation

The experimental investigations on additive manufacturing of Ti-6Al-4V by μ-PTAPD process was conducted in three stages using the research methodology shown in Fig. 2.5 with objectives to (i) to identify optimum values of six influential parameters of μ-PTAPD process (i.e. micro-plasma power, travel speed of deposition head, powder mass flow rate, shielding gas flow rate, plasma gas flow rate and stand-off-distance) for multi-layer single-track deposition of Ti-6Al-4V on substrate of the same material, and (ii) to study their effects on deposition characteristics, tensile properties, microstructure evolution, microhardness, and wear characteristics. All the experiments of all three stages were conducted using the microcontroller programed manipulator system (as shown in Fig. 3.9) in which deposition head of μ-PTAPD process was provided precisely controlled movement along the X, Y and Z directions using stepper motor for each axis. Pilot experiments were conducted in the 1st stage to identify those feasible values of six considered parameters of μ-PTAPD process for the main experiments which ensured continuous single-layer single-track deposition of Ti-6Al-4V powder on substrate of the same material. The identified values for the main experiments were: 418; 429; and 440 W for micro-plasma power, 52; 57; and 62 mm/min for travel speed of the deposition head, 1.5; 2.1; and 2.7 g/min for Ti-6Al-4V powder mass flow rate, 5 Nl/min for shielding gas (i.e. argon) flow rate, 0.3 Nl/min for plasma gas (i.e. argon) flow rate and 10 mm for stand-off-distance. Twenty-seven full factorial main experiments were conducted in the 2nd stage by varying micro-plasma power, powder mass flow rate and travel speed of the deposition head to identify their optimum values considering minimum energy consumption aspects. Identified optimum values were: micro-plasma power as 418 W; powder mass flow rate as 2.7 g/min; and travel speed of deposition head as 62 mm/min. In the 3rd stage of experimentation, thin wall structures of Ti-6Al-4V were made by moving the deposition head in following two ways for its multi-layer single-track deposition by μ-PTAPD process using the optimum values identified from the main experiments: (i) continuous deposition, and (ii) dwell-time deposition.

5.1.1 Pilot Experiments for Single-layer Single-track Deposition

Pilot experiments were conducted to identify feasible values of six significant parameters of μ-PTAPD process namely plasma gas flow rate, stand-off-distance, micro-plasma power, powder mass flow rate, travel speed of deposition head, and shielding gas flow rate by depositing single-layer single-track of Ti-6Al-4V. Table 5.1 presents the ranges of these parameters used in the pilot experiments along with their identified feasible values for the main experiments. Pilot experiments were conducted by varying six significant parameters of μ-PTAPD process (namely flow rate of plasma gas, stand-off distance, micro-plasma power, flow rate of powder, travel speed of the deposition head, and flow rate of shielding gas) using one-factor-at-time experimental design approach and keeping other parameters fixed at their minimum values in their respective ranges

During the pilot experiments, flow rate of the plasma gas was varied in the range from 0.1 to 0.5 Nl/min and it was observed that minimum flow rate of the plasma gas required to form the micro-plasma and transfer it to the substrate was 0.3 Nl/min. Its higher values resulted in spread of the of melt pool generating dimple like impression over top surface of the deposition. The stand-off-distance (SOD) between the deposition head and the substrate was varied from 4 to 12 mm and using 0.3 Nl/min as the plasma gas flow rate. It was found that 10 mm was sufficient SOD to ensure supply of the powdered material to the center of the melt pool. Values of SOD less and more than 10 mm resulted in wastage of the powdered deposition material. Minimum micro-plasma power of 418 W was required to melt powder of Ti-6Al-4V therefore, 418; 429; and 440 W were identified value for the further experiments. Discontinuous single-layers were generated for travel speed of deposition head being greater than 62 mm/min whereas, its value smaller than 52 mm/min resulted in a higher heat affected zone therefore 52, 57, and 62 mm/min were identified for the main experiments. Flow rate of powder more than 1.5 g/min allowed smooth powder feeding and uniform deposition for Ti-6Al-4V whereas its value more than

2.7 g/min gave non-uniform and partially melted powder deposition therefore, values of 1.5; 2.1; and 2.7 g/min were bracketed for the main experiments. Flow rate of shielding gas 5 Nl/min was found satisfactory to protect the molten pool from the atmospheric contamination whereas, its higher values resulted in spread of the of melt pool generating dimple like impression over top surface of the deposition. Flow rate of powder, micro-plasma power, and travel speed of deposition head were found to be the most significant parameters affecting the quality of single-layer deposition. Therefore, these parameters were identified as variables in the next stage of experimental investigations.

Table 5.1: Range of the process parameters used in the pilot experiments and identified values for the main experiments for investigations on additive manufacturing of Ti-6Al-4V alloy by μ-PTAPD process.

Process parameters	Range used in the pilot experiments	Value identified for the main experiments
Plasma gas flow rate (Nl/min)	0.1 - 0.5	0.3
Stand-off-distance (mm)	4 -12	10
Micro-plasma power (W)	242 - 440	418; 429; 440
Powder mass flow rate (g/min)	0.5 -12.0	1.5; 2.1; 2.7
Travel speed of deposition head (mm/min)	30 -150	52; 57; 62
Shielding gas flow rate (Nl/min)	2.0 -9.0	5

5.1.2 Main Experiments for Single-layer Single-track Deposition

Twenty-seven mains were planned and performed using the full factorial approach of a design of experiments depositing single-layer single-track of Ti-6Al-4V alloy on substrate of the same material. In these experiments, micro-plasma power, powder mass flow rate and travel speed of the deposition head was varied at three levels each while values of other three variables (i.e. plasma gas flow rate, shielding gas flow rate, and SOD) were kept constant using their values mentioned in Table 5.1. Out of twenty-seven main experiments, ten parametric combinations which produced continuous and uniform single-layer single-track deposition of Ti-6Al-4V on substrate of the same materials along with their measured (i.e. deposition width and height) and computed responses (i.e. energy consumption per unit traverse length and power consumption per unit powder mass flow rate) are presented in Table 5.2. These experiments identified optimum values of micro-plasma power (as 418 W), powder mass flow rate (as 2.7 g/min), and travel speed of the deposition head (as 62 mm/min) using criteria of minimum energy and power consumption aspects for further experimental investigations.

5.1.3 Experiments for Multi-layer Single-track Deposition

Identified optimum values of micro-plasma power, powder mass flow rate, and travel speed of deposition head as mentioned above were used for multi-layer single-track (thin wall structures) deposition of Ti-6Al-4V alloy on substrate of the same material by moving the deposition head in following two ways: (i) **continuous deposition:** depositing the successive layers both in forward and backward direction movement of the deposition head; (ii) **dwell-time deposition:** depositing the successive layers only in the forward direction movement of the deposition head only when the previously deposited layer cools down to 100°C with temperature being monitored by an infrared pyrometer. This was decided based upon observations of the five experiments conducted keeping temperature of the previously deposited layer as 500 °C, 400 °C, 300 °C, 200 °C and 100°C during deposition of the next layer. Small debonding or spallation of layer with the substrate at starting point was observed when temperature of the previously deposited layer was kept more than 100°C. Therefore, temperature of the previously deposited layer was kept as 100 °C in the dwell-time multi-layer deposition. Ti-6Al-4V has relatively poor thermal conductivity (7.2 W/mK) as compared to other metals therefore, its dwell-time multi-layer deposition can significantly affect its microstructure and mechanical properties (Martina et al., 2012)

5.2 Evaluation and Characterization of the Responses

Evaluation of various characteristics of Ti-6Al-4V depositions manufactured by μ-PTAPD process is essential to quantify its performance. It also helps in evaluating and characterizing the morphology and mechanical properties of the responses. Following paragraphs describe details of the evaluation and characterization of the different responses used in the experimental investigations on Ti-6Al-4V depositions by μ-PTAPD process.

5.2.1 Evaluation of Deposition Geometry

Samples of the single-layer single-track depositions of Ti-6Al-4V corresponding to 10 main experiments and the six samples of multi-layer single-track depositions of Ti-6Al-4V were cut transversely and prepared using the standard metallographic procedure for optical microscopy. The deposition heights and deposition width of single-layer single-track depositions of Ti-6Al-4V corresponding to 10 main experiments were measured using the optical microscope. Optical micrographs of multi-layer single-track depositions of six samples were analyzed with the help of AutoCAD software to measure the total wall width (TWW), effective wall width (EWW) and different deposition areas as depicted in Fig. 5.1. These parameters were used to compute the deposition efficiency (DE) and deposition waviness (DW) of continuous and dwell-time mode depositions of Ti-6Al-4V.

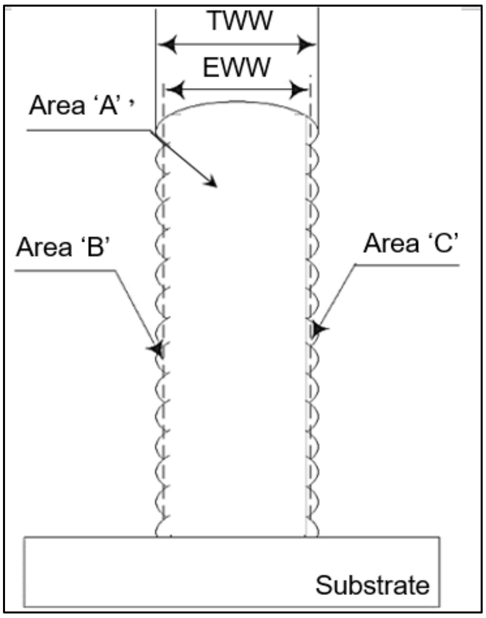

Fig. 5.1. Geometry of a typical multi-layer deposition.

5.2.2 Characterization of Microstructure

Samples of multi-layer single-track depositions (3 samples corresponding to continuous deposition and 3 samples corresponding to dwell-time deposition) of Ti-6Al-4V were prepared by cutting the depositions along the deposition height on the computer numerically controlled (CNC) wire electric discharge machining (WEDM) machine. Subsequently, these samples were polished and etched in a solution of Kroll's reagent containing 3 ml HF, 6 ml HNO_3 and 92 ml water in accordance with the ASTM standard E407. The microstructures of prepared samples were observed using FE-SEM and values of lamellae widths were measured from the top of the multi-layer single-track deposition to the substrate at an interval of 1 mm.

5.2.3 Evaluation of Tensile Properties

Specimens of 25 mm gauge length and 6 mm width (3 samples of continuous deposition of Ti-6Al-4V, 3 samples of dwell-time deposition of Ti-6Al-4V, and 3 samples of Ti-6Al-4V substrate) were cut on the CNC-WEDM machine for evaluation of their tensile properties. These specimens were ground and polished to dimensions as per the requirements of ASTM specifications E8. Figure 5.2 shows photographs of multi-layer single-track deposition and substrate samples prepared for tensile testing. The tensile test was conducted on the prepared specimens using a universal tensile testing machine (model

H50KL from Tinius Olsen USA) loading it at a displacement rate of 0.25 mm/min. Mean values of yield strength, ultimate strength, and % elongation for continuous deposition, dwell-time deposition, and substrate of Ti-6Al-4V were computed by taking average of values of the corresponding samples.

Fig. 5.2: Photographs of the samples prepared for tensile testing.

5.2.4 Evaluation of Microhardness

Samples of multi-layer single-track deposition (3 samples corresponding to continuous deposition and 3 samples corresponding to dwell-time deposition) were cut along their cross-section on the CNC WEDM machine and then fine polished to measure their microhardness from the deposition to substrate at an interval of 1 mm on Vicker's microhardness tester according to the ASTM standard E92-82 using a load of 500 g for duration of 15 seconds.

5.2.5 Evaluation of Wear Characteristics

Wear characteristics of continuous and dwell-time depositions of Ti-6Al-4V at low contact stresses with respect to the hard surfaces were studied using linear reciprocating type wear testing machine (model CM9104 from Ducom USA). This is important because titanium alloys are widely used in biomedical applications such as knee implants, hip joints, surgical devices, bone screws, bone plates, dental implants and industrial applications of compressor blades, fan blades, hubs and discs where wear resistance is extremely important requirement. Three samples of dimension 15 mm x 15 mm x 4 mm were cut to test their wear resistance in accordance with the ASTM Standard G133. These samples were tested using 5 mm diameter tungsten carbide ball under dry conditions at 5Hz, 10 Hz and 15Hz frequency for 15 min time under a load of 15 N. Each wear test was repeated three times. Wear volume was determined by measuring the mass loss of the sample during the wear test using a weight balance having least count of 0.01 mg and dividing it by density of the deposition material.

5.3 Results and Analyses

Following paragraphs describes the results obtained in each stage of experimental investigations on Ti-6Al-4V depositions by µ-PTAPD process along with their interpretation, analysis and main concluding remarks.

5.3.1 Analysis of Single-layer Single-track Deposition

Table 5.2 presents the parametric combinations used in 27 main experiments along with the corresponding measured responses, computed responses (i.e. 'E_l' using Eq. 4.1 and 'P_f' using Eq. 4.2) and observed response (i.e. quality of deposition).

Following observations can be made from Table 5.2:

- Only ten (corresponding to exp. no. 2, 7, 8, 9, 13, 14, 18, 19, 26, and 27) out of the 27 main experiments yielded continuous and uniform single-layer deposition.
- The values of the height and width of deposited layer for these parametric combinations is obtained in the range of 1.52 to 2.35 mm and 2.68 to 3.37 mm respectively.
- Higher flow rate of powder and travel speed have resulted in smaller values of 'E_l' and 'P_f' whereas their lower values have yielded larger values of 'E_l' and 'P_f'.
- Maximum values of 'E_l' and 'P_f' were found to be 507.6 J/mm and 17,600 J/g respectively in experiment no. 19 having µ-plasma power as 440 W; flow rate of powder as 1.5 g/min; and travel speed of deposition head as 52 mm/min. It produced deposition height as 2.02 mm and deposition width as 3.3 mm.
- Minimum values of 'E_l' and 'P_f' were found to be 404.5 J/mm and 9288.8 J/g respectively in experiment no. 9 having µ-plasma power as 418 W; flow rate of powder as 2.7 g/min; and travel speed of deposition head as 62 mm/min. It produced deposition height as 1.89 mm and deposition width as 2.7 mm and their optical image of cross- sectional profile is shown in Fig. 4. It shows that smaller contact angle (Θ) between deposition and fusion line due to interfacial surface tension force which produces good wetting between the deposition and the substrate.

Table 5.2: Parametric combinations used in 27 main experiments along with corresponding measured, computed and observed responses.

Exp. No.	Variable input parameters			Measured responses		Computed responses		Observed response
	μ-plasma power *'P'* (W)	Flow rate of powder *'f'* (g/min)	Travel speed of deposition head *'T'* (mm/min)	Deposition width (mm)	Deposition height (mm)	'P_f' (J/g)	'E_l' (J/mm)	Quality of deposition*
1.	418	1.5	52	2.79	2.14	16720	482.3	NUD
2.	418	2.1	52	2.81	2.31	11942.8	482.3	CUD
3.	418	2.7	52	2.89	2.35	9288.8	482.3	NUD
4.	418	1.5	57	2.69	2.03	16720	440	NUD
5.	418	2.1	57	2.72	2.10	11942.8	440	NUD
6.	418	2.7	57	2.78	2.13	9288.8	440	NUD
7.	418	1.5	62	2.66	1.52	16720	404.5	CUD
8.	418	2.1	62	2.68	1.72	11942.8	404.5	CUD
9.	*418*	*2.7*	*62*	*2.70*	*1.89*	*9288.8*	*404.5*	*CUD*
10.	429	1.5	52	2.95	1.82	17160	495	NUD
11.	429	2.1	52	2.99	1.86	12257.1	495	NUD
12.	429	2.7	52	3.11	1.95	9533.3	495	NUD
13.	429	1.5	57	2.93	1.97	17160	451.5	CUD
14.	429	2.1	57	3.15	2.06	12257.1	451.5	CUD
15.	429	2.7	57	2.85	2.10	9533.3	451.5	NUD
16.	429	1.5	62	2.84	1.96	17160	415.1	NUD
17.	429	2.1	62	2.88	1.99	12257.1	415.1	NUD
18.	429	2.7	62	2.74	1.64	9533.3	415.1	CUD
19.	440	1.5	52	3.30	2.02	17600	507.6	CUD
20.	440	2.1	52	3.34	2.09	12571.4	507.6	NUD
21.	440	2.7	52	3.37	2.3	9777.7	507.6	NUD
22.	440	1.5	57	2.94	1.65	17600	463.1	NUD
23.	440	2.1	57	2.96	1.76	12571.4	463.1	NUD
24.	440	2.7	57	2.99	2.00	9777.7	463.1	NUD
25.	440	1.5	62	2.89	1.42	17600	425.8	NUD
26.	440	2.1	62	3.12	1.53	12571.4	425.8	CUD
27.	440	2.7	62	3.10	1.60	9777.7	425.8	CUD

* *NUD: non-uniform deposition; CUD: continuous and uniform deposition*

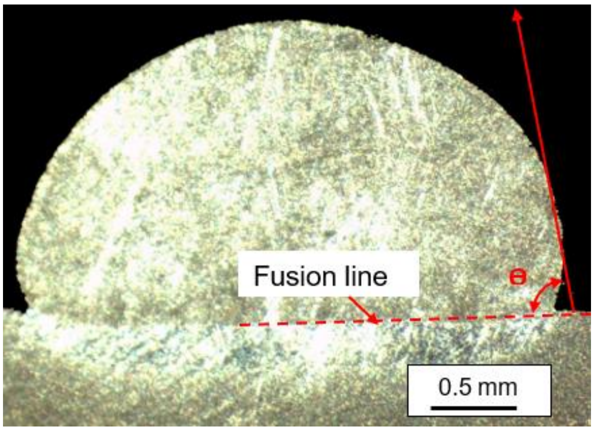

Fig. 5.3: Optical micrograph of continuous single-layer deposition of Ti-6Al-4V corresponding to exp. no. 9.

5.3.2 Analysis of Multi-layer Single-track Deposition

The parametric combination corresponding to exp. no. 4 in Table 5.2 (which resulted in minimum 'E_l' and 'P_f') was used for multi-layer single-track depositions in continuous and dwell-time modes producing a 100 mm long straight wall consisting of 20 deposition layers of Ti-6Al-4V.

5.3.2.1 Deposition Characteristics

Figures 5.4 and 5.5 present the optical micrograph of cross-section and photograph of multi-layer single-track deposition of Ti-6Al-4V in continuous and dwell-time mode on substrate of the same material respectively. Micrograph of the continuous deposition (Fig. 5.3a) shows inter-layer cracks and voids which may be formed due to non-uniform thermal expansion during the solidification process. It indicates weak bonding between different deposition layers and between the deposition and substrate because continuous deposition produces higher heat which causes thermal gradient between the deposition and substrate. In contrast, dwell-time deposition of Ti-6Al-4V (Fig. 5.4a) depicts that there is no inter-layer cracks and voids and has very good metallurgical bonding between the deposition layers and between the deposition and substrate. The multi-layer single-track depositions were further analyzed for measuring TWW and EWW and calculating DE using Eq. 5.1 and DW using Eq. 5.2 (Martina et al. 2012). Table 5.3 presents their results. It can be observed that continuous deposition of Ti-6Al-4V has higher deposition waviness and lower deposition efficiency than that of the dwell-time deposition. This implies that a component manufactured using continuous deposition will require more amount of finishing which will increase cost and wastage of the deposition material.

$$Deposition\ effeciency = \frac{Area\ 'A'}{Area'A' + Area'B' + Area\ 'C'} \times 100 \qquad (5.1)$$

$$Deposition\ waviness = \frac{TWW - EWW}{2} \qquad (5.2)$$

(a) **(b)**

Fig. 5.4: Multi-layer single-track deposition of Ti-6Al-4V in continuous mode by μ-PTAPD process (a) optical micrograph of cross-section; and (b) photograph.

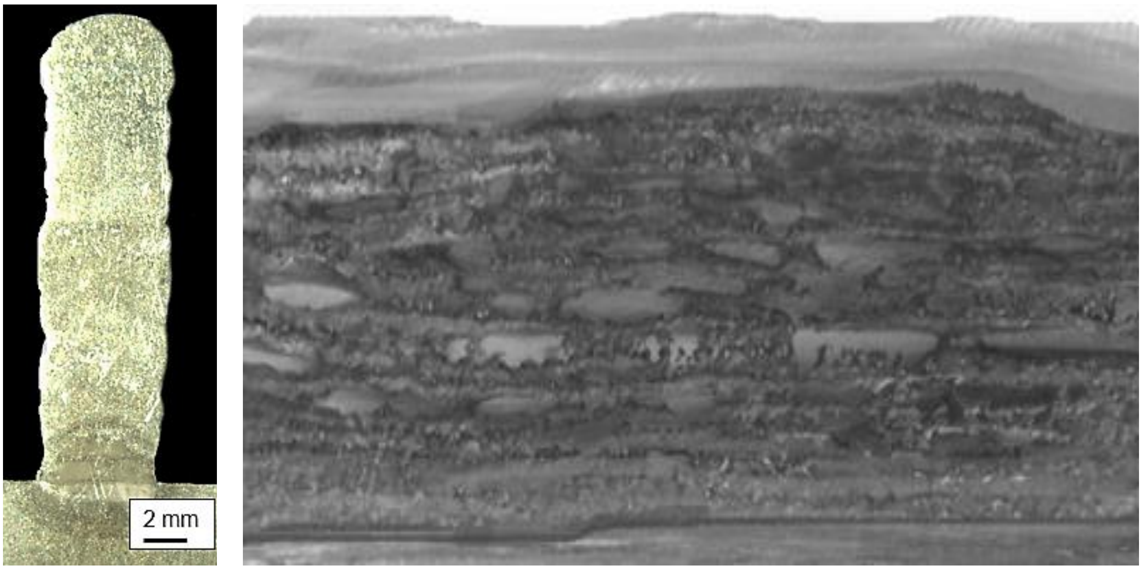

(a) **(b)**

Fig. 5.5: Multi-layer single-track deposition of Ti-6Al-4V in dwell-time mode by μ-PTAPD process (a) optical micrograph of cross-section; and (b) photograph.

Table 5.3: Mean values of total wall width, effective wall width, deposition efficiency and surface straightness for continuous and dwell-time depositions of Ti-6Al-4V.

Deposition type	Total wall width (mm)	Effective wall width (mm)	Deposition efficiency (%)	Deposition waviness (mm)
Continuous depositions	4.1	3.32	77.2	0.39

Dwell-time depositions	3.73	3.51	89.5	0.11

5.3.2.2 Microstructure

Figures 5.6a-5.6f present microstructure of continuous (Fig. 5.6a-5.6c) and dwell-time (Fig. 5.6d-5.6f) depositions of Ti-6Al-4V by μ-PTAPD processes near the top, middle and bottom positions along the deposition height. The microstructures of continuous deposition of Ti-6Al-4V shown in Figs. 5.6a and 5.6b at top and middle positions along the deposition height respectively depict coarse grained microstructure having colonies of lamellar α and β phases placed within the boundaries of the big grains. This is due to slowing down of the solidification process by higher heat content in continuous depositions of Ti-6Al-4V which causes larger melt pool. When the molten material is cooled at sufficiently slow rates from the β-phase into the α-β phase region then α-phase lamellae nucleate preferentially at β grain boundaries leading to continuous α-layer along β-grain boundaries. These α-lamellae continue to grow until they reach to other α-colonies nucleated at other grain boundaries. The individual α-lamellae are separated within α-colonies by the retained β-matrix. The bimodal microstructure also observed near the bottom region of the continuous deposition (Fig. 5.6c) which consists of equi-axed α-phase in coarse α-β lamellar structure due to very slow cooling and recrystallization. Top region of the dwell-time deposition of Ti-6Al-4V (Fig. 5.6d) exhibits needle like microstructure suggesting formation of martensite consisting of α'-phase. Providing dwell-time between deposition of two successive layers of Ti-6Al-4V increases cooling rate which helps in martensitic transformation directly from the β-phase. Lin et al. (2016) reported that minimum cooling rate of 20 ^{o}C per second is essential for the formation of martensitic phases and if cooling rate is more than 410^{0}C per second then entire microstructure can transform to as acicular martensite. Baufeld et al. (2011) mentioned that martensite with extremely fine acicular structure exhibits high strength and hardness but relatively low toughness and ductility. The middle region of dwell-time deposition (Fig. 5.6e) depicts fine basket-weave microstructure which is generally produced by faster cooling rate from β-transition temperature which reduces both α-lamellae thickness and α-colony size. Additionally, new α-lamellae nucleated at other grain boundaries grow perpendicularly to the existing lamellae. This leads to formation of the basket-weave microstructure. Bottom region of dwell-time deposition (Fig. 5.6f) shows the fine lamellar structure also known as Widmanstätten microstructure which is typically consequence of multiple thermal cycles. Deposition of new layer on the previously deposited layer affects the microstructure of previous layer by possible re-melting and reheating in the β or (α-β) phase field.

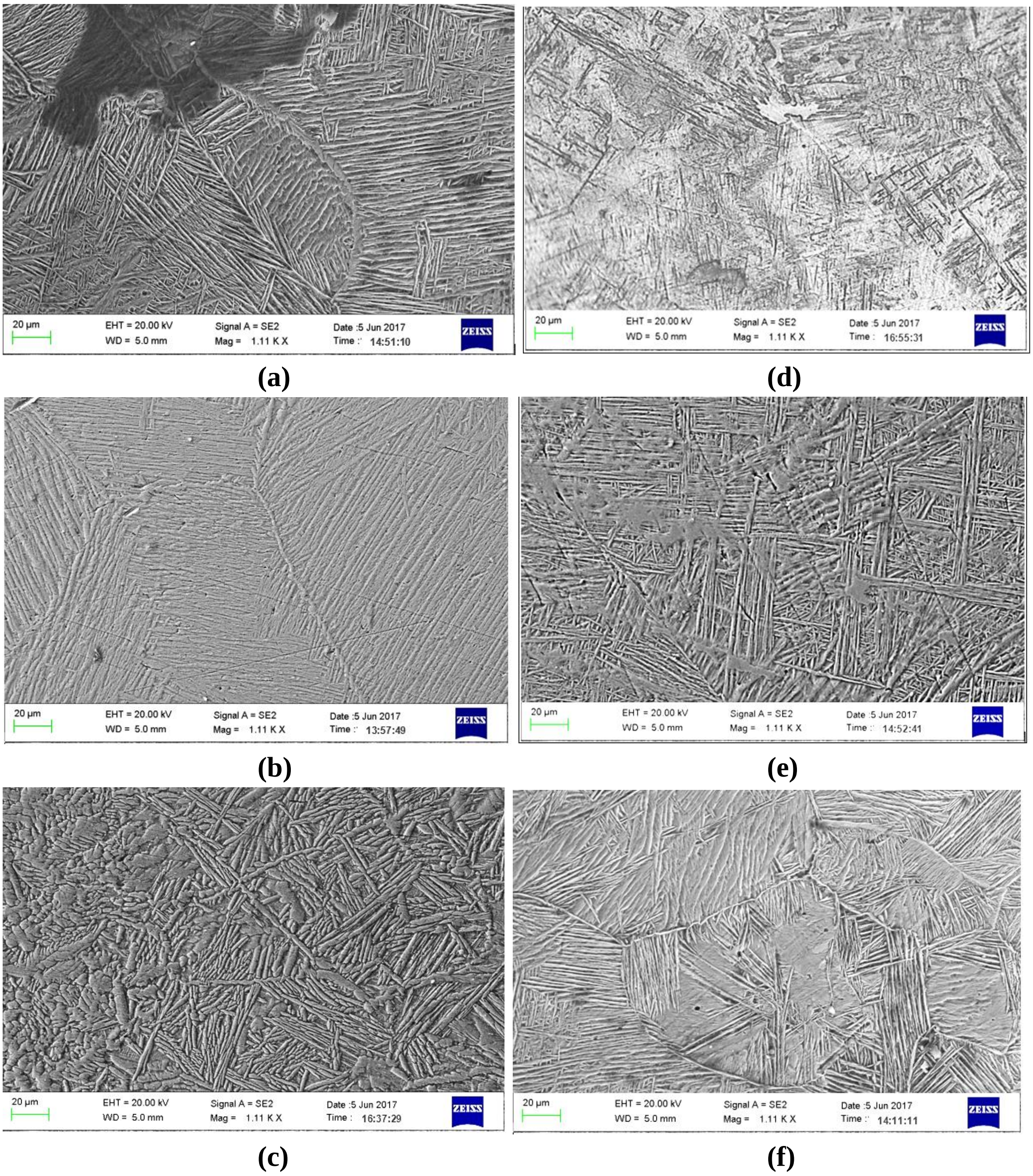

Fig. 5.6: Microstructure of continuous deposition of Ti-6Al-4V (a, b and c) and dwell-time deposition of Ti-6Al-4V (d, e and f): (a) and (d) top position; (b) and (e) middle position; and (c) and (f) bottom position along the deposition height.

Figure 5.7 shows lamellae widths measured from the microstructures of continuous and dwell-time depositions of Ti-6Al-4V. It can be observed from this figure that (i) both continuous and dwell-time depositions exhibit smaller width of lamellae in the top region than that in the bottom region, (ii) lamellae widths of dwell-time deposition are smaller than that of continuous deposition. Therefore, it can conclude that faster cooling rate in dwell-time deposition decreases lamellae width and results in the finer microstructure.

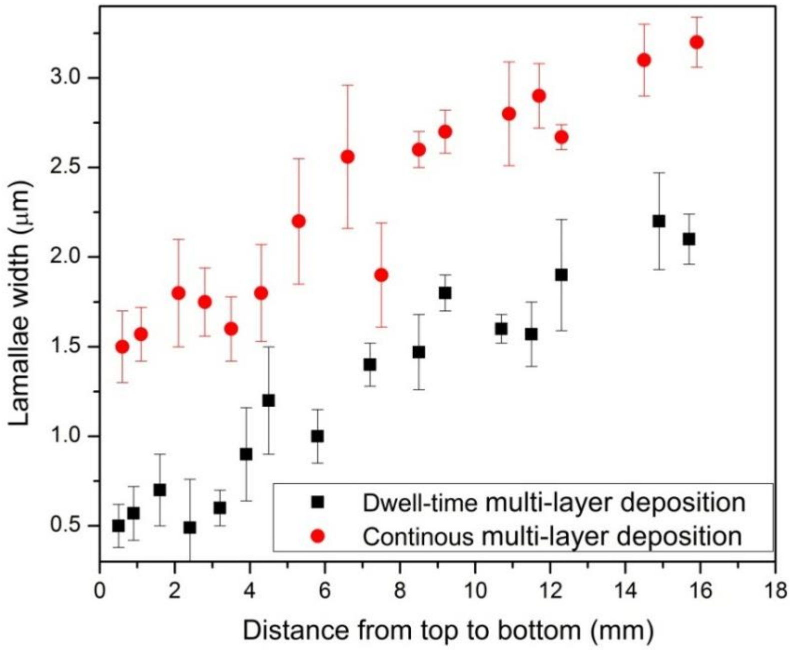

Fig. 5.7: Lamellae widths for continuous and dwell-time depositions of Ti-6Al-4V.

5.3.2.3 Tensile properties

Table 5.4 presents mean values of the ultimate strength, yield strength and % elongation for continuous and dwell-time multi-layer single-track deposition of Ti-6Al-4V by μ-PTAPD process. It can be observed that dwell-time deposition has a much higher ultimate strength (930.3 MPa) and yield strength (890 MPa) than that of continuous deposition and Ti-6Al-4V substrate. But, continuous deposition exhibits higher % elongation (18.2 %) and ductility than the dwell-time deposition and Ti-6Al-4V substrate. This can be explained by fact that rapid solidification of dwell-time deposition of Ti-6Al-4V restrains the growth of lamellar structure results in the fine microstructure. The fine microstructure of partial acicular martensite and basket-weave structure imparts higher yield and ultimate strength.

Table 5.4: Mean values of the yield strength, ultimate strength and strain for continuous and dwell-time depositions of Ti-6Al-4V.

Specimens	Mean value of yield strength (MPa)	Mean value of ultimate strength (MPa)	Mean value of elongation (%)
Continuous deposition	754	788	18.2
Dwell-time deposition	890	930.3	13.2
Ti-6Al-4V substrate	785	805.6	17.3

Figure 5.8 depicts fractography of the tensile specimen of the multi-payer depositions of Ti-6Al-4V by μ-PTAPD process. Tensile specimen fractured surface of dwell-time deposition (Fig. 5.8a) exhibits fine dimple rupture while that of continuous deposition (Fig. 5.8b) shows occurrence of tear ridges or elongated regions due to coarse lamellar microstructure which imparts the ductility to it. These results can be correlated to the lamellae width (Fig. 5.7) thus relating microstructure refinement with mechanical properties. It means that ductility increases with increase in lamellae width but ultimate and yield strength decreases. These results suggest that dwell-time deposition provides combination of good strength and good ductility which satisfy the ASTM F1108 specifications.

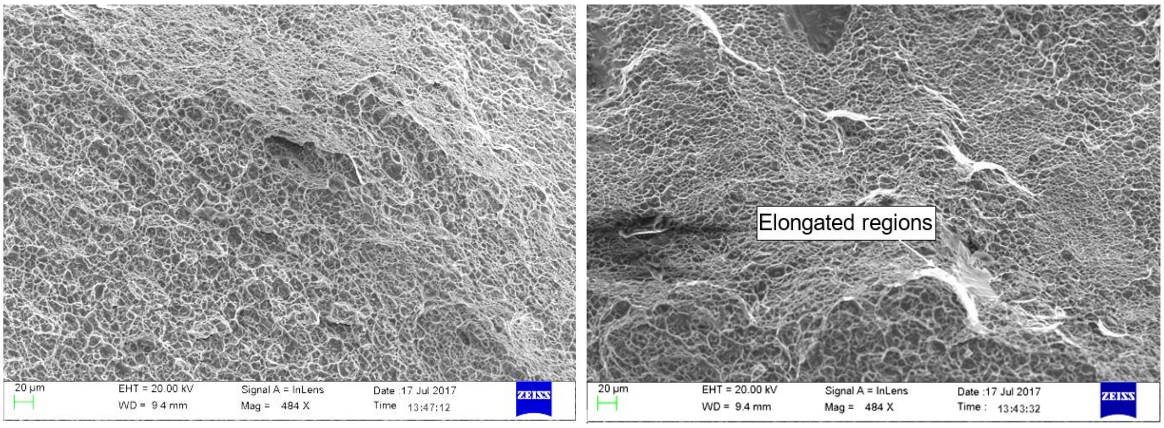

(a) **(b)**

Fig. 5.8: Fractography of tensile specimen of (a) dwell-time; and (b) continuous depositions of Ti-6Al-4V.

5.3.2.4 Microhardness

Figure 5.9 presents microhardness profile for continuous and dwell-time depositions of Ti-6Al-4V by μ-PTAPD process. It can be observed from this figure that (i) microhardness of dwell-time deposition of Ti-6Al-4V is much higher than the continuous deposition due to its rapid cooling which leads to formation of finer microstructure; (ii) higher microhardness near top region and slight increase in microhardness near HAZ in both continuous and dwell-time depositions of Ti-6Al-4V due to formation of harder martensitic α’-phase near the top region. This proves that mechanical properties of the Ti-6Al-4V depositions are significantly affected by the thermal cycle and the developed microstructures.

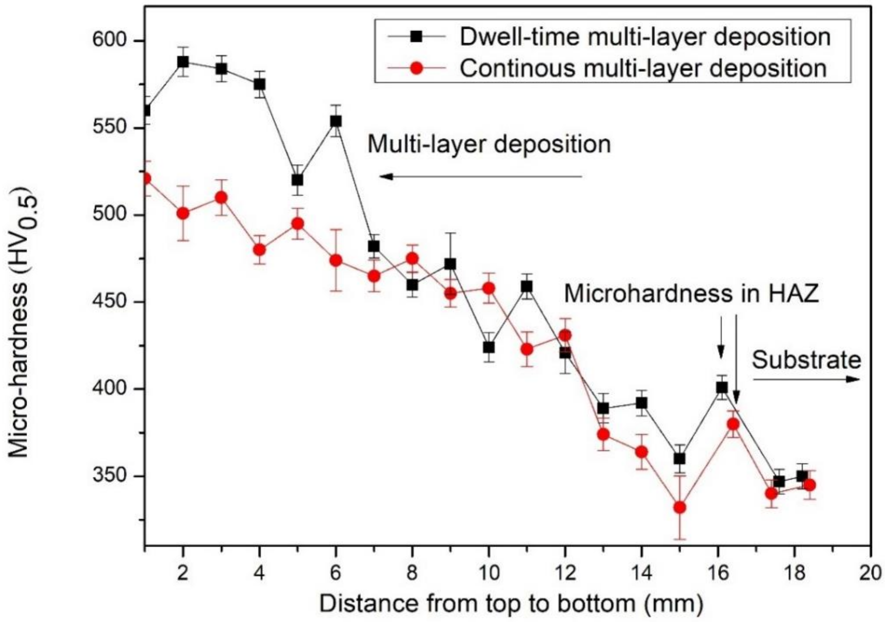

Fig. 5.9: Microhardness profile for the continuous and dwell-time depositions of Ti-6Al-4V alloy.

5.3.2.5 Wear Characteristics

Wear is a complicated phenomenon and it depends on many factors including hardness, morphology, surface topography and cyclic stress. Two-body and three-body abrasive wear appear in different forms such as micro-ploughing, micro-cracking, micro-cutting or micro-fatigue. Figure 5.10 present variation of wear volume with frequency for continuous and dwell-time depositions of Ti-6Al-4V by µ-PTAPD process. Figures 5.11a-5.11c show variation of coefficient of friction with the time for three frequency values and Figs. 5.12a and 5.12b illustrate wear mechanism for dwell-time and continuous depositions of Ti-6Al-4V respectively. Following inferences can be made from these figures:

- Dwell-time deposition has lower wear volume than continuous deposition of Ti-6Al-4V for all values of frequency (Fig. 5.10). Wear volume of continuous deposition increases drastically at 15 Hz frequency due to extensive ploughing and micro-cutting of the deposition. This result can be correlated to the results of microstructure (Fig. 5.6) and microhardness (Fig. 5.9). It shows that formation finer partial martensite and basket-weave microstructure and higher microhardness of dwell-time deposition of Ti-6Al-4V help it in exhibiting lower wear volume.
- Coefficient of friction for dwell-time deposition of Ti-6Al-4V is smaller than that of continuous deposition at all values of frequency (Figs. 5.11a-5.11c). Figure 5.11a shows that values of coefficient of friction for dwell-time deposition at 5 Hz frequency

remain vary in a very narrow range (0.002-0.012) which will result in less frictional resistance. SEM image of its worn surface (Fig. 5.12a) indicate that its wear takes place by micro-ploughing which forms very shallow grooves and micro-cutting resulting in very less wear debris i.e. better wear resistance.

- Coefficient of friction for continuous deposition of Ti-6Al-4V shows many irregular fluctuations at higher frequency (Figs. 5.11b and 5.11c) with comparatively higher mean value of coefficient of friction. SEM image of worn surfaces of continuous deposition (Fig. 5.12b) indicates formation of deep grooves by repetitive ploughing and eventually breaking of grooves' edges. This is suggestive of three-body abrasive wear during relative motion of any surface against this surface by entrapment of some wear debris.

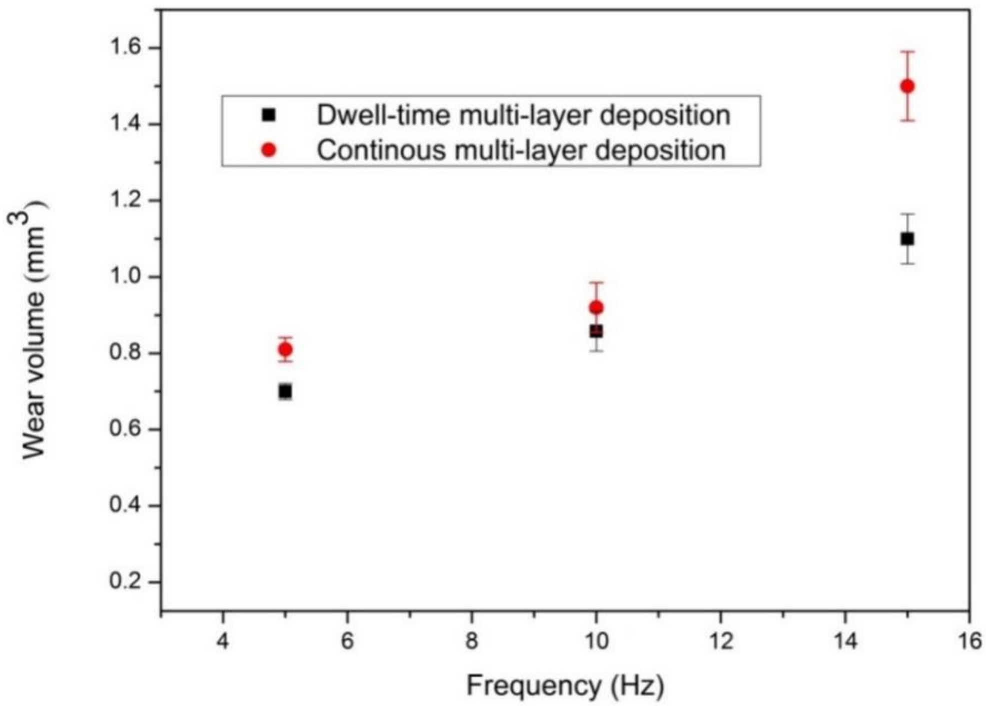

Fig. 5.10: Variation of wear volume with frequency for continuous and dwell-time depositions of Ti-6Al-4V.

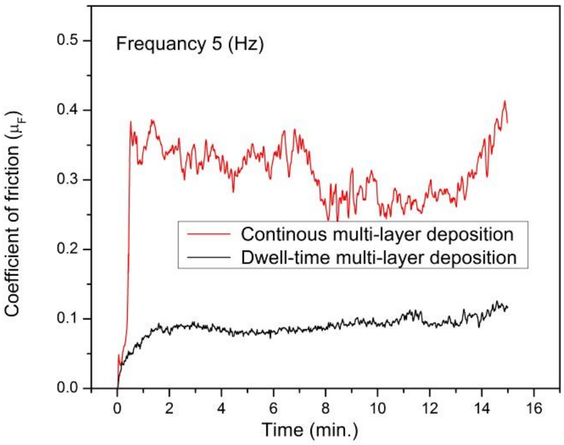

(a)

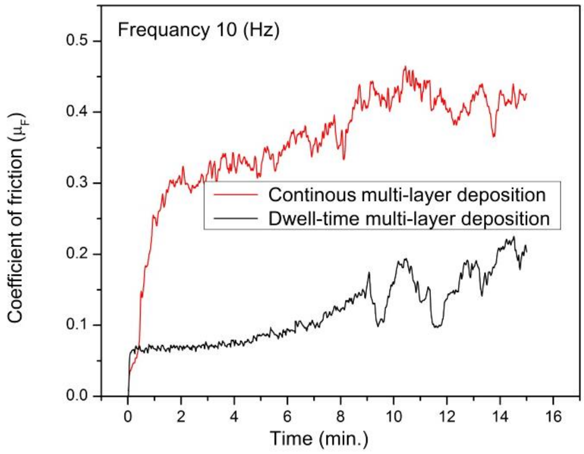

(b)

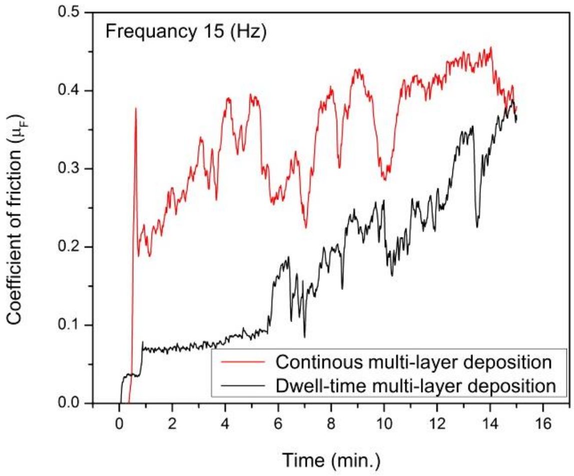

(c)

Fig. 5.11: Variation of coefficient of friction with time for continuous and dwell-time depositions of Ti-6Al-4V at different frequency: (a) 5 Hz; (b) 10 Hz; and (c) 15 Hz.

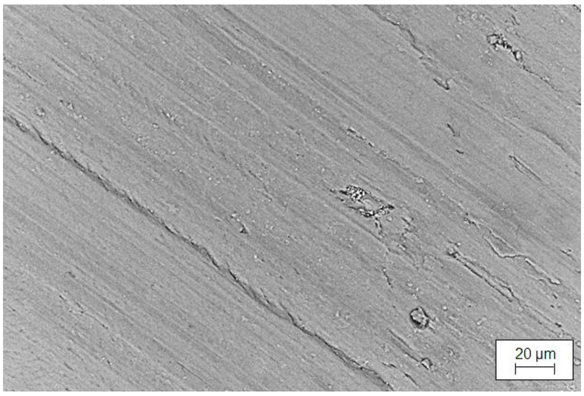

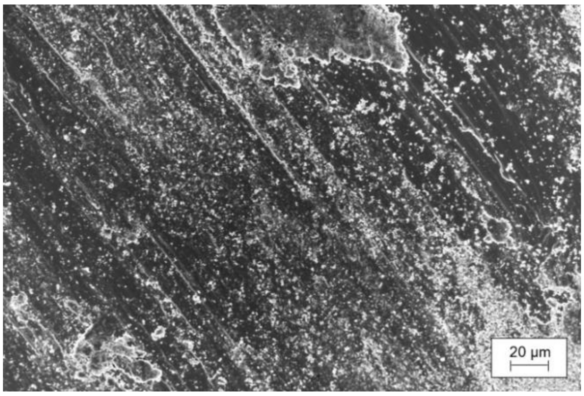

(a) **(b)**

Fig. 5.12: SEM images showing wear mechanism of (a) dwell-time; and (b) continuous depositions of Ti-6Al-4V.

5.3.2.6 Comparison of Dwell-time Deposition by μ-PTAPD Process with the Existing Processes for Ti-6Al-4V Deposition

Table 5.5 presents comparison of dwell-time deposition with the existing processes for multi-layer single-track deposition of Ti-6Al-4V in terms of 'P_f', 'E_l', ultimate tensile strength, strain, microhardness and cost.

Table 5.5: Comparison of dwell-time μ-PTAPD process with the existing processes for multi-layer single-track deposition of Ti-6Al-4V.

Authors (Year)	Type of energy source	Power consumption per unit powder mass flow rate (J/g)	Energy consumption per unit traverse length (J/mm)	Ultimate tensile strength (MPa)	Strain (%)	Average value of microhardness (HV)	Cost of operation and power supply
Baufeld et al. (2011)	Nd:YAG laser	Not applicable (used wire)	88	980-1,140	3.5-6	450	Higher
Brandle et al. (2011)	Nd:YAG laser	Not applicable (used wire)	350	925	12	Not available	Higher
Gharbi et al. (2013)	Yb:YAG laser	19,200-30,000	50-192	Not available			Higher
Mahamood et al. (2017)	Nd:YAG laser	27,777-2,50,000	50	Not available		391	Higher
Lin et al. (2016)	Pulsed plasma arc	Not applicable (used wire)	519-823	988	7	360	Low
Present work	μ-PTAPD	9,288	404	930	13.2	504	Medium

This comparative evaluation confirms that dwell-time μ-PTAPD process is cost-effective than laser-based deposition processes and energy efficient than pulsed plasma arc. It requires lower power consumption per unit mass flow rate of powder and gives higher microhardness of multi-layer single-track deposition which results in lower wear volume.

5.4 Additive Manufacturing of Typical Components of Ti-6Al-4V

The dwell-time μ-PTAPD process was further employed to additively manufacture complex geometry components such as hollow cylindrical and hollow rectangular shapes as depicted in Fig. 5.13.

(a) **(b)**

Fig. 5.13: Photograph of typical components of Ti-6Al-4V manufactured by μ-PTAPD process (a) cylindrical, and (b) rectangular.

5.5 Concluding Remarks

Following concluding remarks can be made from the experimental investigations on additive manufacturing of Ti-6Al-4V alloy by μ-PTAPD process:

- Single-layer single-track deposition of Ti-6Al-4V by μ-PTAPD process has deposition height and width in the range of 1.52 to 2.3 mm and 2.68 to 3.3 mm respectively. Higher powder mass flow rate and travel speed of deposition head result in smaller values of energy consumption per unit traverse length and power consumption per unit mass flow rate of powder and vice-versa.
- Identified optimum values of micro-plasma power, powder mass flow rate and travel speed of deposition head corresponding to minimum values of power consumption per unit mass flow rate of powder (9,288.8 J/g) and energy consumption per unit traverse length (404.5 J/mm) are 418 W; 2.7 g/min; and 62 mm/min respectively. These were used in continuous and dwell-time depositions of Ti-6Al-4V by μ-PTAPD process.
- Dwell-time deposition of Ti-6Al-4V yielded higher deposition efficiency and lower deposition waviness than continuous deposition i.e. continuous deposition will require more finishing which increases cost and wastage of the deposition material.
- Dwell-time deposition had good deposition quality with fine partial martensite and basket-weave microstructure while continuous deposition has cracks, weak bonding and coarser lamellar microstructure.

- Both continuous and dwell-time depositions of Ti-6Al-4V have smaller lamellae widths in the top region than that in the bottom region. Lamellae widths of dwell-time deposition are smaller than that of continuous deposition. Faster cooling rate in dwell-time deposition decreases lamellae width and results in the finer microstructure. Ductility increases with increase in lamellae width but ultimate and yield strength decreases.
- Dwell-time deposition of Ti-6Al-4V has higher yield and ultimate strength. Tensile specimen fractured surface of dwell-time deposition exhibits fine dimple rupture while that of continuous deposition shows occurrence of tear ridges or elongated regions.
- Dwell-time deposition of Ti-6Al-4V has higher microhardness, lower wear volume, lower friction coefficient than continuous deposition. This is important because titanium alloys are widely used in biomedical applications such as knee implants, hip joints, surgical devices, bone screws, bone plates, dental implants and industrial applications of compressor blades, fan blades, hubs and discs where wear resistance is extremely important requirement.
- Wear of dwell-time deposition takes place by micro-ploughing which forms very shallow grooves and micro-cutting resulting in very less wear debris. While that of continuous deposition takes place by formation of deep grooves by repetitive ploughing and eventually breaking of grooves' edges.
- Comparative evaluation confirms that dwell-time µ-PTAPD process for Ti-6Al-4V deposition has higher efficiency in power consumption and cost-effective than laser-based deposition processes and yields higher microhardness which will result in smaller wear volume.

The ***next chapter*** presents planning and details of the experimental work, evaluation and characterization of the responses as well as results and analyses for the texturing of HSS tool by µ-PTAPD process.

Chapter 6

Investigations on Texturing of HSS Tool

This chapter presents planning and details of the experimental investigations, evaluation and characterization of the responses along with the results and their analyses for the texturing of the HSS tool by μ-PTAPD process with an objective to improve performance of material removal process of titanium alloys. It presents the effect of μ-PTAPD process parameters on dilution of the spot textures as well as on diameter, depth, and aspect ratio of dimple textures. It also compares the performance of textured HSS tools with non-textured high speed steel (HSS) tool in terms of machining forces, temperature and wear of the tool, chip formation, and surface roughness of titanium alloy (i.e. Ti-6Al-4V) workpiece.

6.1 Planning and Details of Experimentation

The experimental investigations for dimple and spot texturing of single edge HSS machining tool by μ-PTAPD process were conducted in the following four stages using the research methodology shown in Fig. 2.6:

- **Stage-1:** Pilot experiments were conducted to identify feasible values of the variable parameters of μ-PTAPD process (i.e. micro-plasma power and exposure time for the dimple texturing and micro-plasma power, exposure time and mass flow rate of powder of Stellite 6 for the spot texturing) producing single texture on shank of the HSS machining tool in each experiment. The identified values for the main experiments were: 246.4; 264; and 281.6 W for micro-plasma power and 15; 30; and 45 seconds for exposure time for use in dimple texturing, and 264; 286; and 316 W for micro-plasma power; 6; 10; and 14 seconds for exposure time, 1.45; 1.76; and 2.10 g/min for powder mass flow rate for use in the spot texturing.
- **Stage-2:** Nine main experiments were conducted to identify those optimum values of the considered variable parameters which will maximize aspect ratio (i.e. ratio of depth to diameter) of the dimple textures and dilution of the spot textures by varying them at the pilot experiments identified values to manufacture single texture on shank of the HSS machining tool in each experiment. Full factorial experimental design was used for dimple texturing and Taguchi's L_9 orthogonal array was used for spot texturing. The identified optimum values for further experiments were: 264 W for micro-plasma power and 45 seconds for exposure time for use in the dimple texturing, and 316 W for

micro-plasma power; 14 seconds for exposure time, and 1.76 g/min for powder mass flow rate for use in the spot texturing.

- **Stage-3:** Arrays of 12 spot and 12 dimple textures on the rake face of HSS machining tool (as shown in Fig. 6.1) were produced using the identified optimum values of the considered variable parameters. The spot-textures were ground to make their sizes uniform.
- **Stage-4:** Performance of the dimple-textured, spot-textured and non-textured HSS machining tools was compared in terms of machining forces, temperature and flank wear of the tool, chip formation, and surface roughness of the machined workpiece while turning Ti-6Al-4V cylindrical bar under flooded type coolant system. Single cutting edge HSS machining tools were made from 13 mm square bar by imparting 10^{o} as back rake angle; 4.4 side rake angle; 15^{o} as end relief angle; zero degree as side relief angle; 12^{o} end cutting edge angle; 5^{o} side cutting edge angle as per machine tool reference (MTR) system nomenclature. Other parameters selected for turning of Ti-6Al-4V bar were: 45 and 105 m/min as cutting speed; 0.1 mm/revolution as feed rate; and 1 mm as depth of cut (da Silva et al. 2013). Each turning experiment was repeated four times each for dimple-textured, spot-textured and non-textured HSS tool.

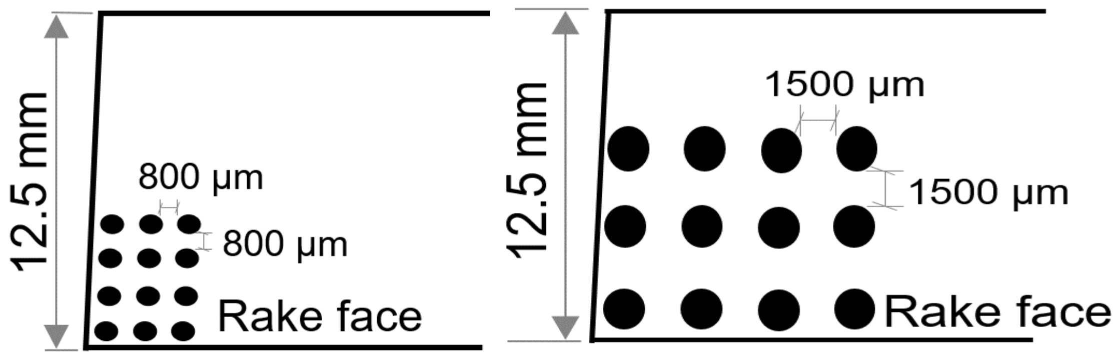

(a) (b)

Fig. 6.1: Schematic of array of the (a) dimple textures and (b) spot textures on rake face of the HSS cutting tool.

6.1.1 Dimple Texturing of HSS Tool

During pilot experiments of dimple texturing, it was observed that plasma gas flow rate as 0.3 Nl/min and stand-off-distance as 10 mm were sufficient to maintain continuous micro-plasma arc and transfer the required heating power towards the substrate. Minimum micro-plasma power of 246.4 W and exposure time as 15 s were required to melt the surface of HSS machining tool and to create a visible dimple whereas micro-plasma power more than 281.6 W and exposure time of 45 seconds resulted in excessive heating and melting. Therefore, 246.4; 264; and 281.6 W of micro-plasma power and 15; 30; and 45 seconds of exposure time were identified value to conduct 9 full factorial main experiments (details given in Table 6.1) to study their effects on diameter, depth and aspect ratio of the dimple textures. From the main experiments, micro-plasma power as 264 W and exposure time as 45 seconds were identified as optimum values to obtain dimple texture having higher aspect ratio and approximately circular shape. They were used for manufacturing an array of 12 dimples on the rake face of the HSS tool.

6.1.2 Spot Texturing of HSS Tool

During pilot experiments of spot texturing, it was observed that plasma gas flow rate as 0.3 Nl/min and stand-off-distance as 10 mm were sufficient to maintain continuous micro-plasma arc and transfer the required heating power towards the substrate. Minimum micro-plasma power of 264 W; exposure time of 6 second; and powder mass flow rate of 1.45 g/min were required to melt powder of Stellite 6. Powder mass flow rate more than 2.10 g/min gave partially melted powder deposition whereas exposure time more than 14 s gave excessive HAZ. Consequently, 264; 286; and 316 W for micro-plasma power; 6; 10; and 14 s for exposure time, 1.45; 1.76; and 2.10 g/min for powder mass flow rate were identified values to conduct nine main experiments designed using Taguchi's L_9 orthogonal array (details are given in Table 6.1) to study their effects on dilution of the spot textures. From the main experiments, micro-plasma power as 316 W; exposure time as 14 s; and powder flow rate as 1.76 g/min were identified as optimum values to achieve approximately sphere-shaped spot textures having high dilution ratio and minimum attachment of the unmolten particles. These values were used to manufacture an array of 12 spot textures on the rake face of the HSS tool.

Table 6.1: Experimental designs for dimple and spot texturing of HSS tool.

Exp. No.	Dimple texturing (Full factorial)		Spot texturing (Taguchi's L_9 orthogonal array)		
	μ-plasma power (W)	Exposure time (s)	μ-plasma power (W)	Exposure time (s)	Powder mass flow rate (g/min)
1.	246.4	15	264	6	1.45
2.	246.4	30	264	10	1.76
3.	246.4	45	264	14	2.10
4.	264	15	286	6	1.76
5.	264	30	286	10	2.10
6.	264	45	286	14	1.45
7.	281.6	15	316	6	2.10
8.	281.6	30	316	10	1.45
9.	281.6	45	316	14	1.76

6.2 Characterization and Measurements

Approximate diameter and depth of nine dimples were measured using surface profilometer (MarSurf LD130, from Mahr, Germany). Nine samples of spot-textured HSS tools were cut transversely and prepared using the standard metallographic procedure for optical microscopy. Percentage dilution of a spot-textured sample was calculated using Eq. 4.1. Three samples of dimples and 3 samples of spots were characterized using FE-SEM. Machining forces and temperature of the textured and non-textured HSS machining tools during turning of Ti-6Al-4V were measured using 3-axis Kistler dynamometer (Fig. 6.2a) and K type thermocouple (Fig. 6.2b) respectively.

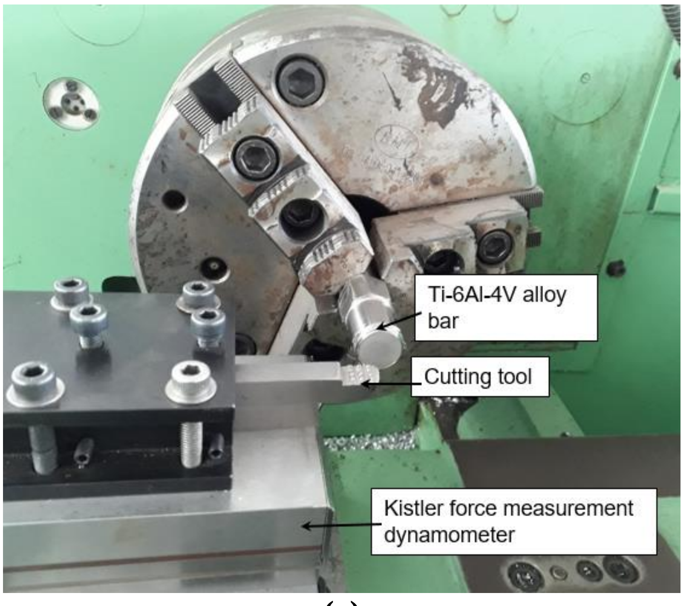

(a)

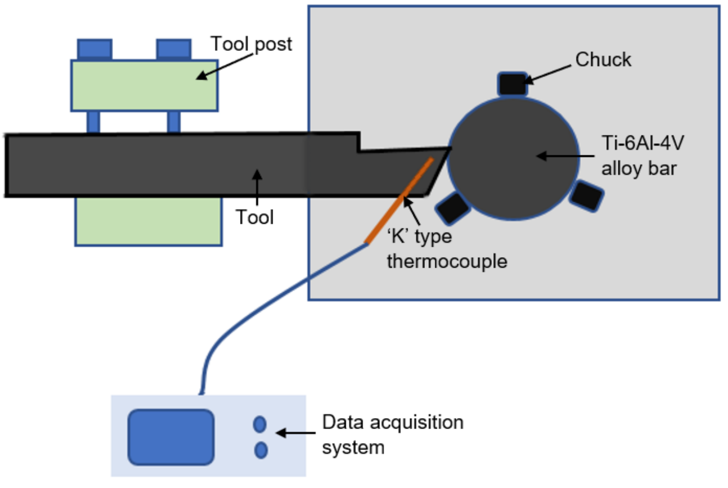

(b)

Fig. 6.2: Turning of Ti-6Al-4V by the textured HSS machining tool: (a) arrangement for measurement of machining forces; and (b) schematic of arrangement for measurement of temperature of the HSS tool.

6.3 Results and Analyses

Following paragraphs describes the results obtained in each stage of experimental investigations on texturing of HSS tool by μ-PTAPD process and performance comparison of textured and non-textured tool along with their interpretation and analysis.

6.3.1 Study and Analysis of Dimple Texturing

Figure 6.3 presents diameters, depths and aspect ratios of the dimples produced on HSS tool by μ-PTAPD process for nine combinations of micro-plasma power and exposure time as mentioned in Table 6.1 during main experiment. It can be seen from this figure that (i) the dimples produced by micro-plasma power at 281.6 W have shallow depths and large diameters resulting lower aspect ratio whose value increases from 0.17 to 0.25 as exposure time increases from 15 to 45 s; (ii) the dimples produced by micro-plasma power at 246.4 W have very small depth. Maximum depth achieved is 0.19 mm for exposure time of 45 s; (iii) the dimples produced using micro-plasma power of 264 W have higher values of the aspect ratios than those produced using micro-plasma power of 281.6 W and 246.4 W; and (iv) for each value of micro-plasma power, exposure time of 45 s results in highest aspect ratio. Therefore, SEM images of three dimples (presented in Figs.6.4a-6.4c) manufactured using 45 seconds of exposure time for three different values of micro-plasma power were obtained and analyzed.

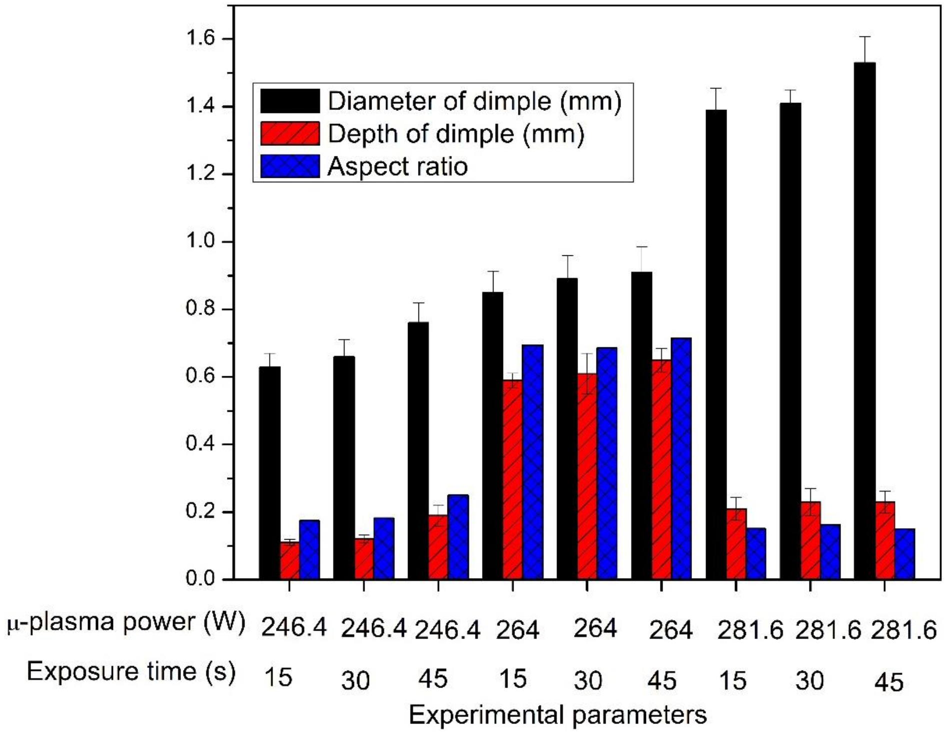

Fig. 6.3: Diameter, depth and aspect ratio of the dimple textures produced by μ-PTAPD process for different combinations of parameters.

It can be observed from the SEM image shown in Fig. 6.4a that the material from the tool surface is melted and re-deposited which leads to porous and rough surface and uneven size of the dimple. This is due to higher power of micro-plasma of 281.6 W which melts larger area from surface of HSS tool and produces significant undulations due to re-deposition of the molten material. This leads to higher surface roughness within the dimple. It can be seen from SEM image depicted in Fig. 6.4b that 246.4 W of micro-plasma power is not sufficient for considerable melting of material from surface of the HSS tool. Whereas, SEM image of Fig. 6.4c shows use of micro-plasma power of 264 W results in a dimple which nearly circular shaped with very less deposition of the molten material around its circumference. This is due to fact that the material expelled out of a dimple depends on micro-plasma power and pressure generated by it. It has also highest aspect ratio as shown in Fig. 6.3. Consequently, an array of 12 dimples was made on rake face of the HSS tool using micro-plasma power as 264 W and exposure time as 45 seconds. Its optical image and photograph are shown in Figs. 6.5a and 6.5b respectively.

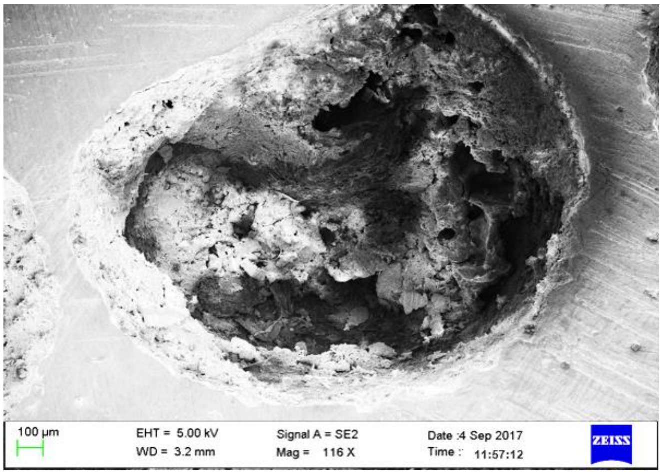

(a)

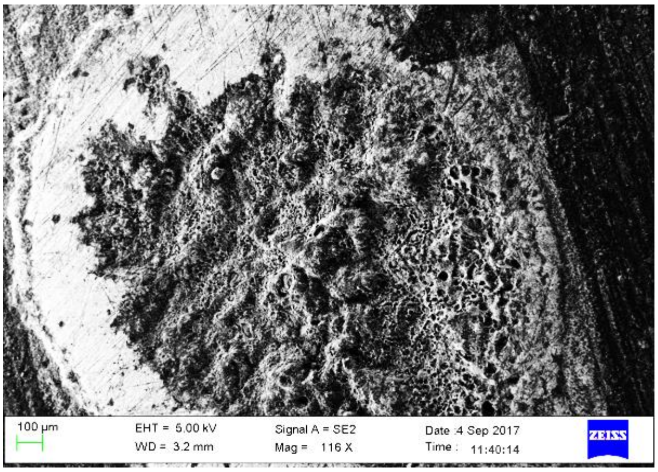

(b)

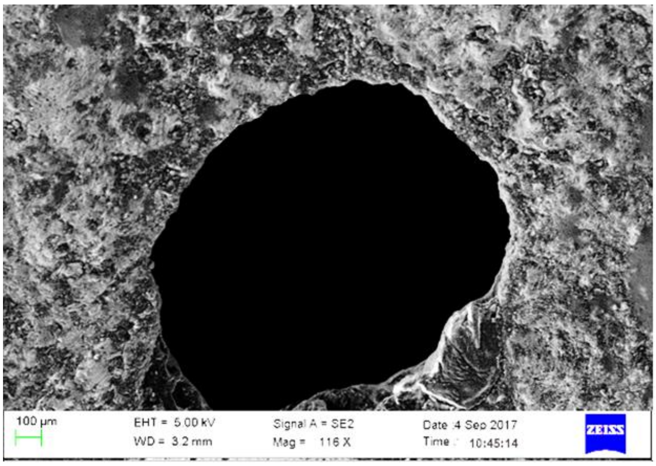

(c)

Fig. 6.4: SEM images of three dimples textures manufactured using 45 seconds of exposure time and micro-plasma power as (a) 281.6 W; (b) 246.4 W; and (c) 264 W.

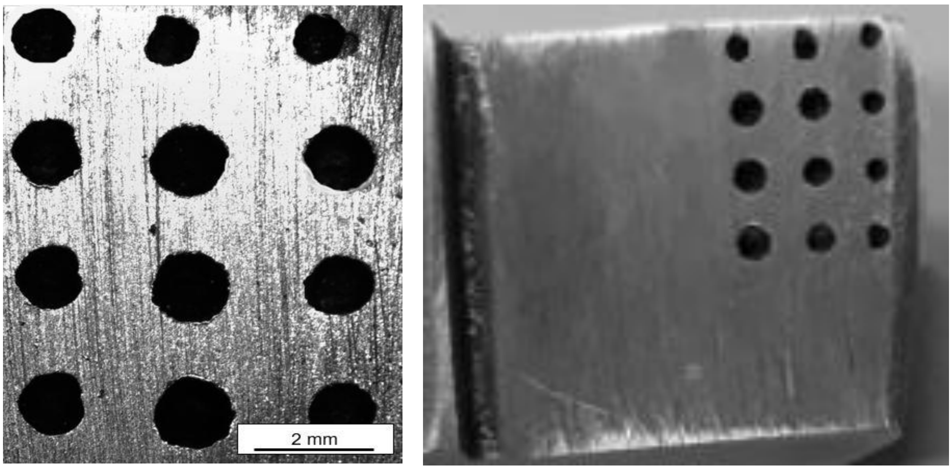

(a) **(b)**

Fig. 6.5: Array of the dimple textures produced by µ-PTAPD process on the rake face of the HSS tool using micro-plasma power as 264 W and exposure time as 45 seconds: (a) optical image; and (b) photograph.

6.3.2 Study and Analysis of Spot Texturing

Figure 6.6 presents dilution of the spot textures produced by depositing powder of Stellite 6 on the HSS tool by µ-PTAPD process for nine combinations of micro-plasma power, exposure time and powder mass flow rate as per Taguchi's L_9 orthogonal array (details given in Table 6.1). It can be observed from this figure that (i) spots produced by micro-plasma power of 264 W have small values of dilution ranging from 5.5 to 5.8% for exposure time from 6 to 14 seconds. This is due to insufficient heat produced by this micro-plasma power which melts smaller amount of HSS tool material. Smaller dilution produces weaker bond between the spot texture and HSS tool substrate, (ii) use of 286 W as micro-plasma power increases dilutions of the spot textures in the range from 9.5 to

10.2% for exposure time ranging from 6 to 14 seconds, (iii) the spot textures produced using micro-plasma power of 316 W have the highest values of the dilutions than those produced using 286 W and 264 W, and (iv) for each value of micro-plasma power, exposure time of 14 seconds results in highest value of dilution. Therefore, SEM images of three spots (presented in Fig 6.7a-6.7c) manufactured using 14 seconds of exposure time for three different combinations of micro-plasma power and powder mass flow rate were obtained and analyzed. It can be observed from the SEM image shown in Fig. 6.7a that 264 W of micro-plasma power is not sufficient enough for complete melting and depositing spot of Stellite 6 powder fed at mass flow rate of 2.1 g/min. The SEM image of Fig. 6.7b depicting the spot manufactured using 286 W micro-plasma power and 2.1 g/min powder mass flow rate shows some unmolten particles in the spot and spatter around it. The SEM image of the spot (Fig.6.7c) manufactured using 316 W micro-plasma power and 1.7 g/min as Stellite powder mass flow rate shows that its shape is nearly spherical, and it has sound deposition quality with very few unmolten particles. Therefore, an array of 12 spot was made on rake face of the HSS tool using micro-plasma power as 316 W; exposure time as 14 seconds; and powder mass flow rate as 1.7 g/min. The spots were ground to make their sizes uniform. Its optical image and photograph are shown in Figs. 6.8a and 6.8b respectively.

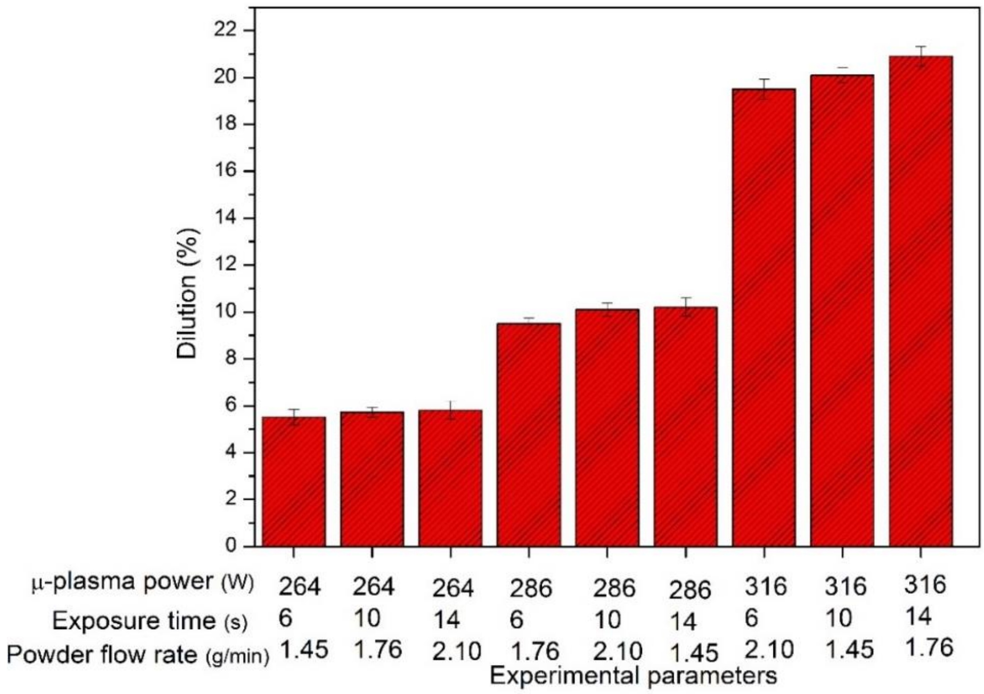

Fig. 6.6: Dilutions of the spot textures produced by μ-PTAPD process for different combinations of micro-plasma power, exposure time and powder mass flow rate.

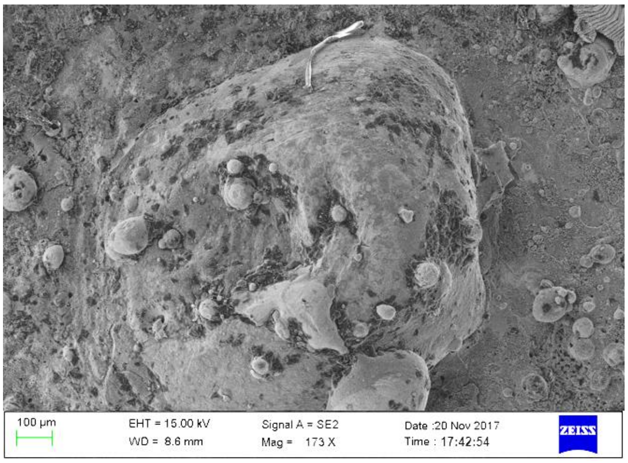

(a)

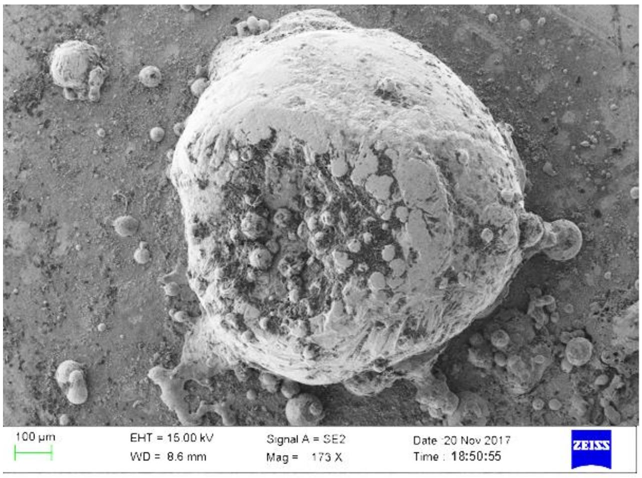

(b)

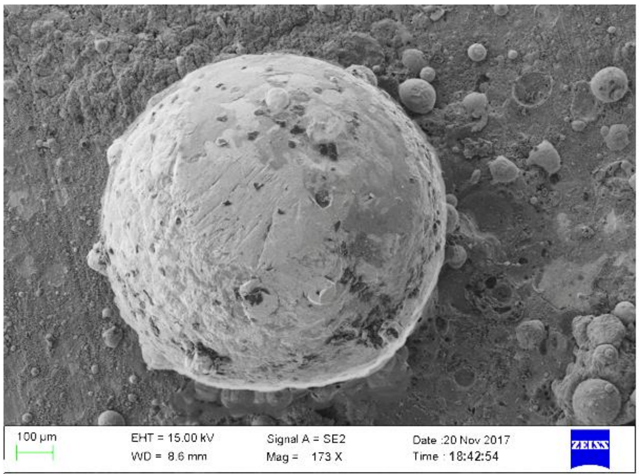

(c)

Fig. 6.7: SEM images of the spot textures manufactured using 14 seconds of exposure time and micro-plasma power and powder mass flow rate as (a) 264 W and 2.10 g/min; (b) 286 W and 2.10 g/min; and (c) 316 W and 1.76 g/min.

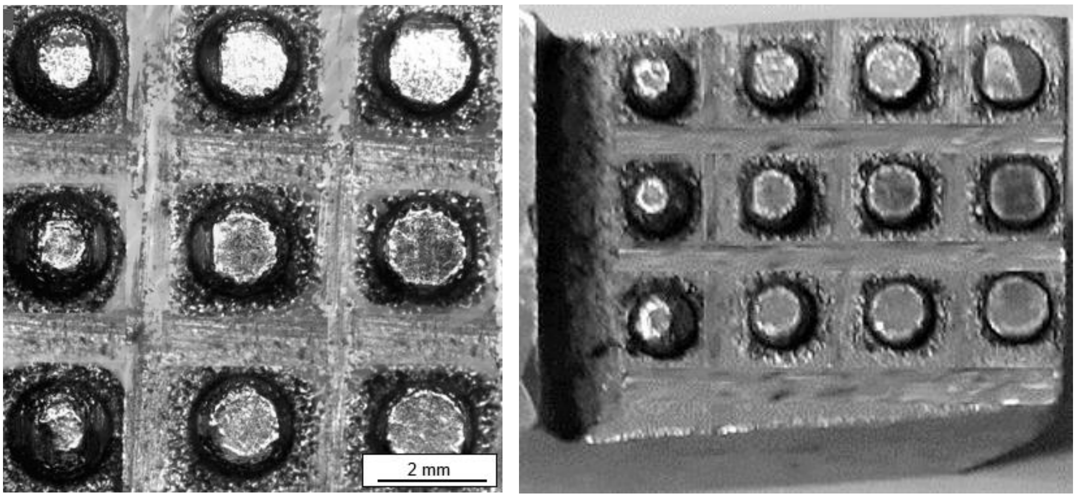

(a) **(b)**

Fig. 6.8: Array of the spot textures produced by µ-PTAPD process on the rake face of the HSS tool: (a) optical image and; (b) photograph.

6.3.3 Performance Comparison of Textured and Non-Textured Tool

Following paragraphs describe results of the comparative study between the textured HSS machining tools with the non-textured HSS tool in terms of machining forces, tool temperature, tool wear, chip formation, and surface roughness of the machined workpiece while cylindrical turning of Ti-6Al-4V alloy workpiece using these machining tools.

6.3.3.1 Cutting and thrust forces and coefficient of friction

Figure 6.9 presents variation of average cutting force (Fig. 6.9a) and thrust force (Fig. 6.9b) with cutting speed during cylindrical turning of Ti-6Al-4V alloy workpiece by the spot-textured and dimple-textured HSS machining tools by µ-PTAPD process and the non-textured HSS machining tool. It can be observed from these figures that (i) cutting and thrust forces increase with cutting speed for the spot, dimple and non-textured HSS tools; (ii) spot-textured HSS tool results in minimum values of cutting and thrust forces while non-textured tool gives their maximum values at both the cutting speeds. Values for the dimple-textured HSS tool are in between them; (iii) cutting force for the spot-textured HSS tool was nearly 14.12 % and 13.73 % less than the non-textured HSS tool and 5.33 % and 7.56 % less than dimple-textured HSS tool at 45 m/min and 105 m/min cutting speed respectively; and (iv) thrust force for the spot-textured HSS tool was nearly 19.93 % and 20.74 % less than the non-textured HSS tool and 8.24 % and 12.32 % less than dimple-textured HSS tool at 45 m/min and 105 m/min cutting speed respectively. These observations can be explained with the help of schematic Fig. 6.10, it shows that flow of chips over the spot-textured HSS tool which increases rake angle and reduces chip curl radius. Increase in rake angle reduces the cutting force (Gunay et al., 2005) whereas reduction in the chip curl radius helps in chip breaking which aids in reduction of thrust force (Yilmaz et al. 2018).

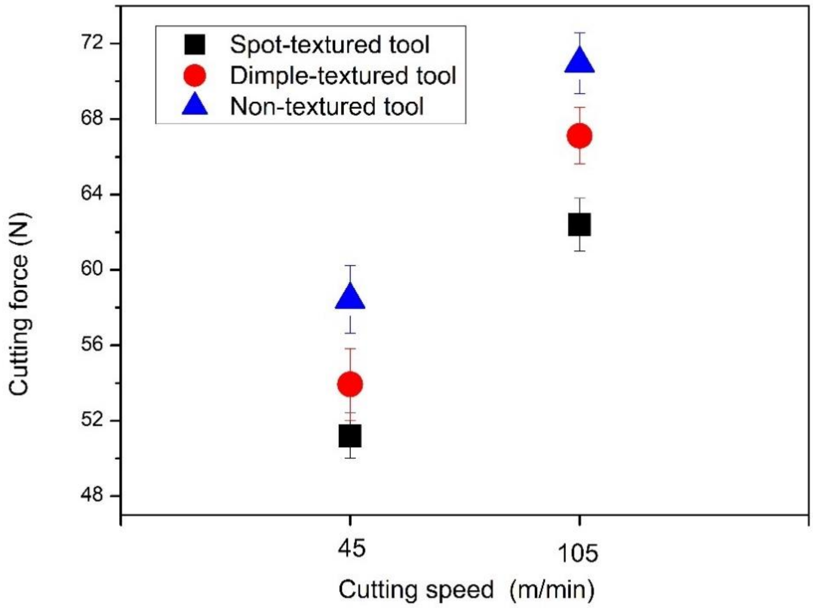

(a)

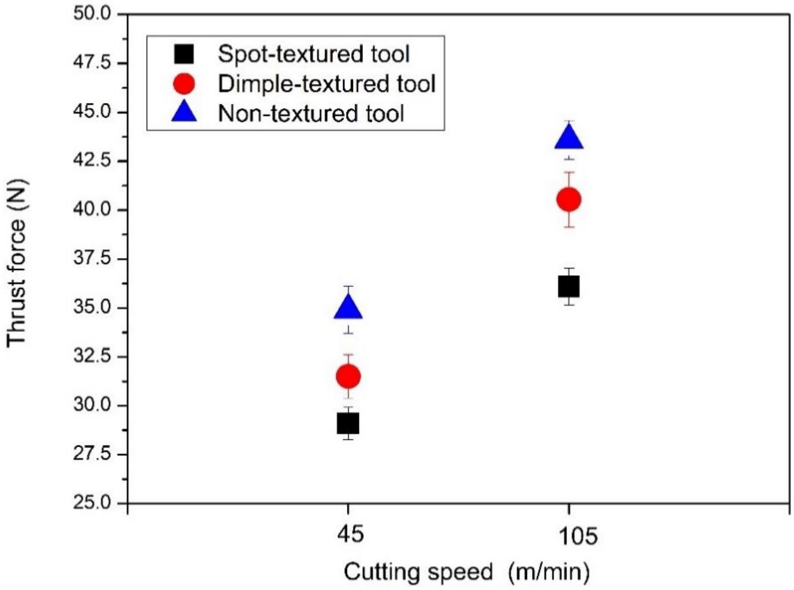

(b)

Fig. 6.9: Variation of (a) Cutting force; and (b) thrust force, with the cutting speed during cylindrical turning of Ti-6Al-4V alloy workpiece by the spot-textured, dimple-textured and non-textured HSS machining tools.

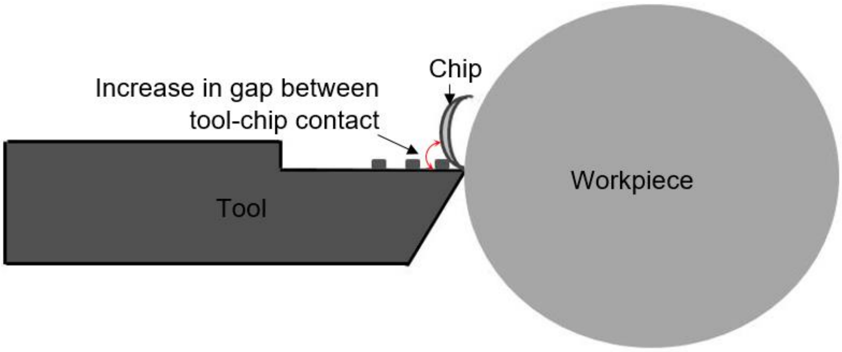

Fig. 6.10: Schematic of chip flow over the rake face of the spot-textured HSS machining tool during cylindrical turning of Ti-6Al-4V alloy workpiece.

The coefficient of friction was calculated using Eq. 6.1 (Hao et al., 2018) and their results are shown in the Fig. 6.11.

$$\mu = \frac{(F_t + F_c\ tan\alpha)}{(F_c - F_t\ tan\alpha)} \qquad (6.1)$$

Where, μ is friction coefficient, F_c is cutting force; F_t is thrust force; and α is the rake angle of the cutting tool. It can be observed from this that (i) coefficient of friction increases with cutting speed for the spot, dimple and non-textured HSS tools; (ii) At both the cutting speeds, the spot-textured HSS tool results in minimum values of the coefficient of friction and non-textured HSS tool gives maximum values of the coefficient of friction; and (iii) coefficient of friction for the spot-textured HSS tool was nearly 3.40 % and 4.23 % less than the non-textured HSS tool and 1.92 % and 3.07 % less than dimple-textured HSS tool at 45 m/min and 105 m/min cutting speed respectively. These observations can be explained by the fact that the spots on the rake face of HSS tools helps in enhancing supply of the machining fluid to the tool-chip interface which reduces the friction tool-chip interface. Flow of chips over the dimple-textures increases the gap between the rake face of the tool and chip and enhances supply of machining fluid as compared to the non-textured HSS tool which reduces the friction at the tool-chip interface.

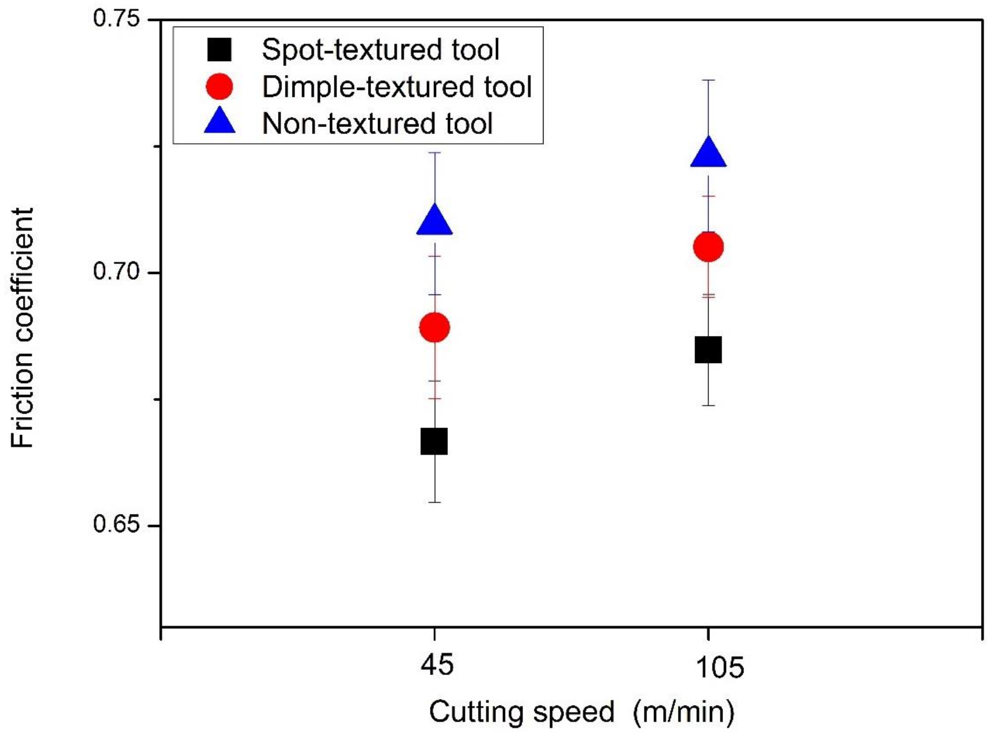

Fig. 6.11: Coefficient of friction at different cutting speed during turning of Ti-6Al-4V using spot-textured, dimple-textured and non-textured HSS tool.

6.3.3.2 Temperature of the Tool

Figure 6.12 depicts temperature of the spot-textured, dimple-textured and non-textured HSS machining tools during turning of Ti-6Al-4V alloy at different cutting speed. It can be observed from this figure that (i) cutting tool temperature for the textured and non-textured HSS tool increases with increase in the cutting speed; (ii) temperature of the spot-textured HSS tool is minimum at both the cutting speeds, followed by that of dimple-textured and non-textured HSS tool. Temperature of spot-textured HSS tool was 11.32% and 12.92% less than the non-textured tool and 3.85% and 5.60% less than the dimple-textured tool at 45 m/min and 105 m/min cutting speed respectively. This is due to early separation of Ti-6Al-4V chips from rake face of the spot-textured tool which reduces the contact length and friction at the tool-chip interface, and consequently reducing the temperature of the spot-textured tool (Yilmaz et al. 2018). Additionally, spots act as fins which enhances the heat loss to the machining environment by increasing the surface area of rake face of the spot-textured tool thus helping in further reduction of its temperature (Cengel, 2002).

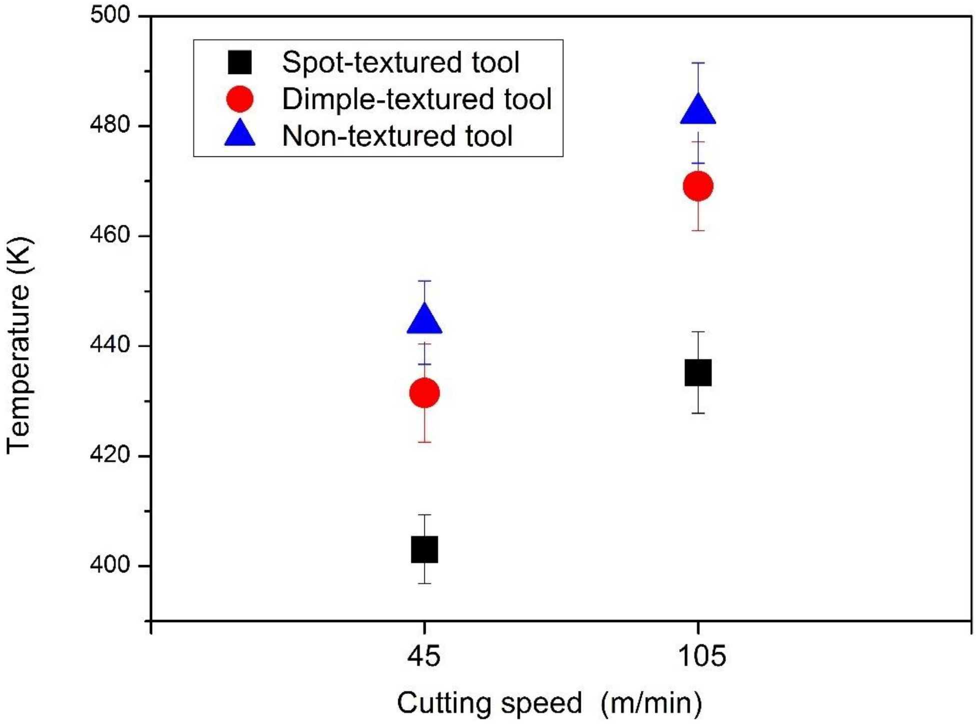

Fig. 6.12. Temperature of the spot-textured, dimple-textured and non-textured HSS machining tools during cylindrical turning of Ti-6Al-4V alloy at different cutting speeds.

6.*3.3.3 Flank Wear of the Tool*

Figure 6.13 presents values of the average flank wear (VB_B) of the spot-textured, dimple-textured and non-textured cutting tools during turning of Ti-6Al-4V at different cutting speed. It can be observed from this figure (i) average flank wear of the textured and non-textured HSS tools increases with increase in the cutting speed; (ii) average flank wear of the spot-textured HSS tool is minimum at both the cutting speeds, followed by that of dimple-textured and non-textured HSS tool. Average flank wear of spot-textured HSS tool is 9.2 % and 9.97% less than the non-textured HSS tool and 6.4 % and 7.18 % less than the dimple-textured HSS tool at 45 m/min and 105 m/min cutting speed respectively. These observations can be explained with help of the optical images of the flank wear of the non-textured (Fig. 6.14a), dimple-textured (Fig. 6.14b) and the spot-textured (Fig. 6.14c) HSS tools and the SEM images showing adhesion of the workpiece material to them (Figs. 6.15a-c). These images reveal that the spot-textured HSS tool exhibits least amount of flank wear (Fig. 6.14c) and adhesion of the least amount of workpiece material to it (Fig. 6.15c) than the dimple-textured and non-textured HSS tools. The adhered material is easier to tear off under the combination of higher temperature, pressure and cutting speed which accelerates their flank wear (Sun et al., 2015). Higher temperature of the dimple and non-textured HSS cutting tools (Fig. 6.12) also reduces their hardness causing further wear of their flank surfaces (Zheng et al. 2018).

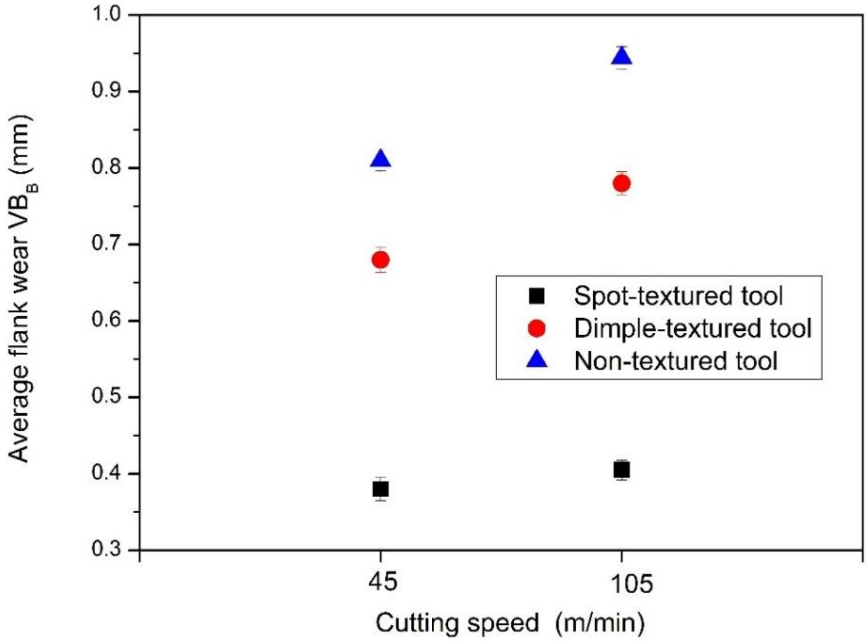

Fig. 6.13: Average flank wear at different cutting speed during turning of Ti-6Al-4V using spot-textured, dimple-textured and non-textured HSS tool.

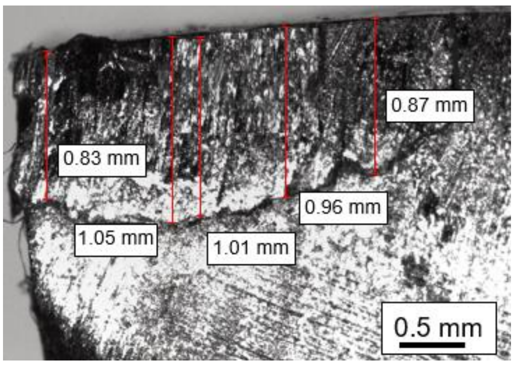

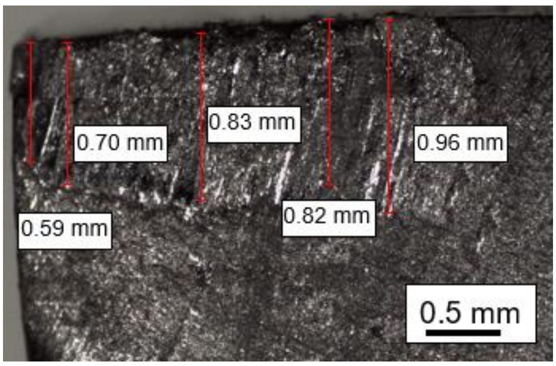

(a) (b)

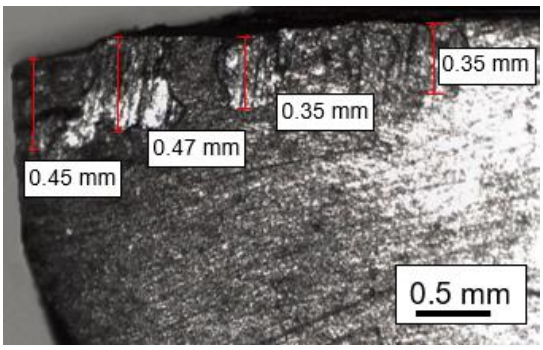

(c)

Fig. 6.14: Optical images showing flank wear of the HSS tool: (a) non-textured; (b) dimple-textured; and (c) spot-textured.

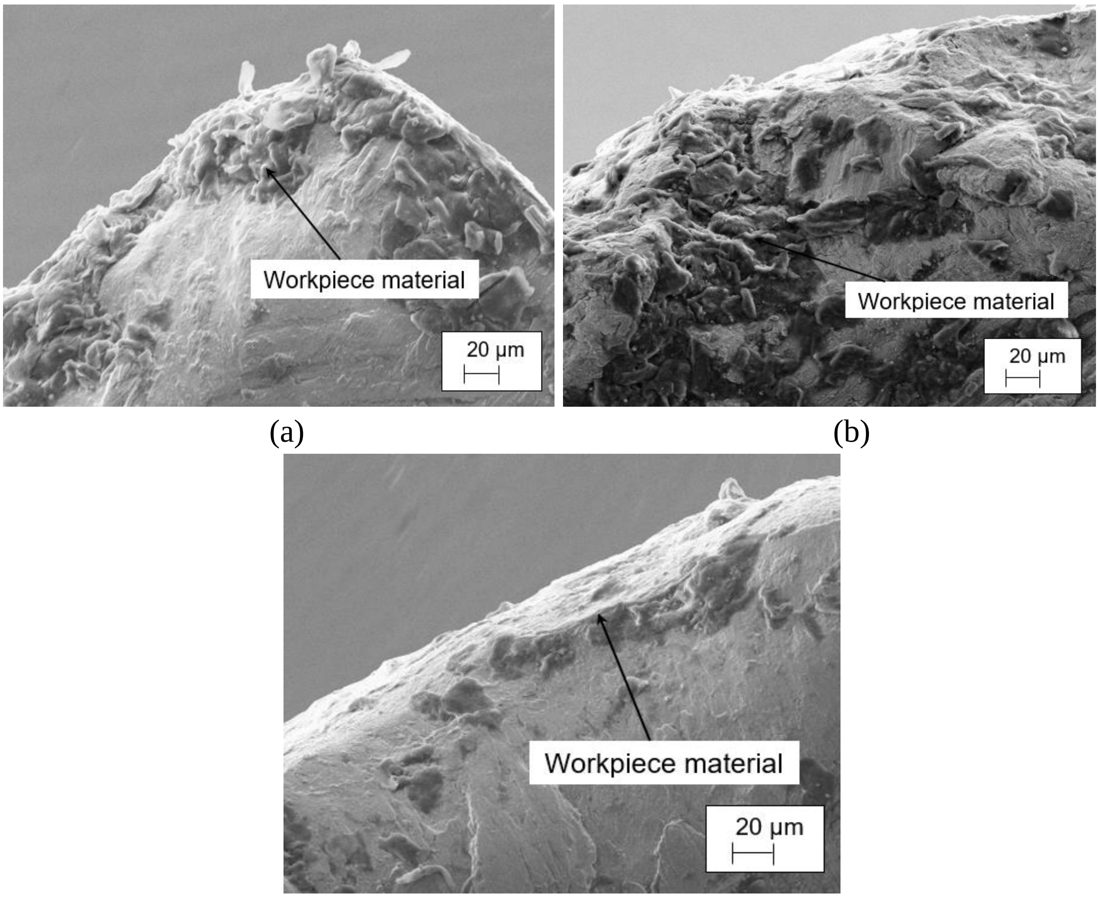

(a) (b)

(c)

Fig. 6.15: SEM images depicting adhesion of the workpiece material to the HSS tool: (a) non-textured; (b) dimple-textured; and (c) spot-textured.

6.3.3.4 Chip shapes

Figure 6.16 shows photographs of the chips formed by non-textured tool (Fig. 6.16a1 and 6.16a2); dimple-textured tool (Fig. 6.16b1 and 6.16b2); and spot-textured tool (Fig. 6.16c1 and 6.16c2) during turning of Ti-6Al-4V at cutting speeds of 105 and 45 m/min respectively and compared with standard chip form (ISO 3685:1993). It can be observed from these photographs that the (i) non-textured HSS tool produced long snarled ribbon type unbroken chips at both the cutting speed of 105 m/min (Fig. 6.16a1) and 45 m/min (Fig. 6.16a2); (ii) dimple-textured HSS tool yielded snarled washer type helical chips at the cutting speed of 105 m/min (Fig. 6.16b1) and short washer type helical broken chips at 45 m/min cutting speed (Fig. 6.16b2); and (iii) spot-textured HSS tool resulted in formation of arc type broken chips at both the cutting speed of 105 m/min (Fig. 6.16c1) and 45 m/min (Fig. 6.16c2).

Arc type broken chips and short washer type helical chips help in reducing the heat transferred to the textured HSS tools and thus increasing their life. But, continuously snarled ribbon-like and snarled washer type helical chips are undesirable because they obstruct supply of machining fluid to the machining zone, further continuation of the machining process, and clear viewing of the machining zone. They also increase tool-chip contact length leading to transfer of more amount of heat to the cutting tool thus adversely affecting its life and surface roughness of the machined surface. Moreover, such types of chips necessitate intermittent stopping of the machining process for their removal and to avoid their entanglement.

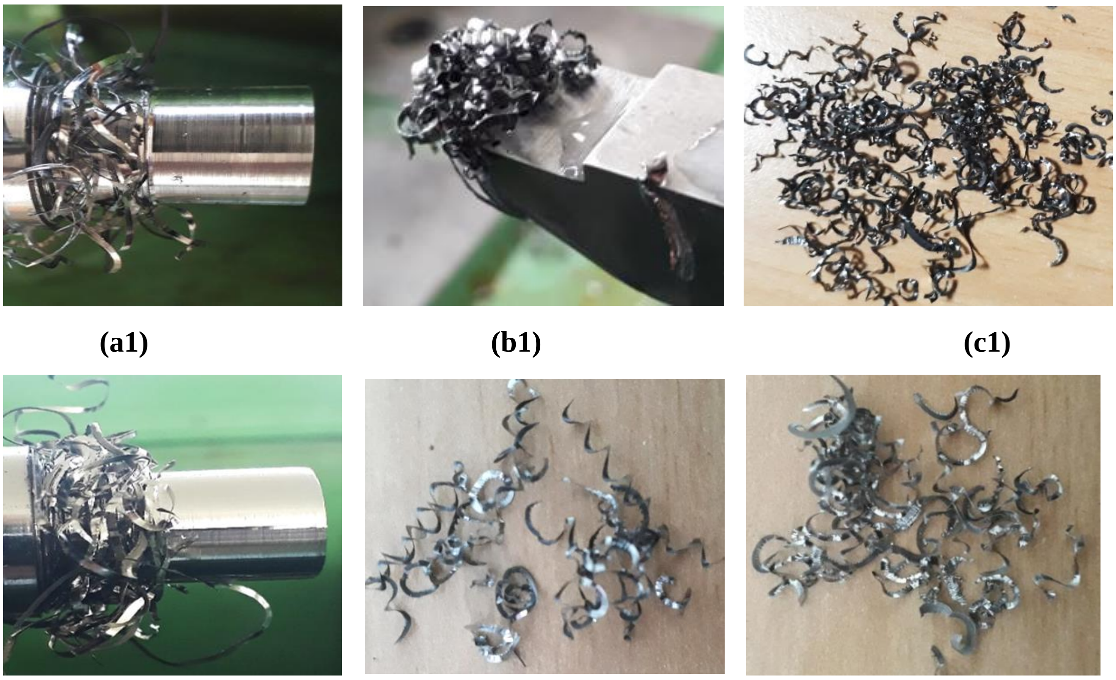

(a1) **(b1)** **(c1)**

(a2) **(b2)** **(c2)**

Fig. 6.16: Photographs of the chips formed during turning of Ti-6Al-4V at the cutting speed of 105 m/min (a1, b1, and c1) and 45 m/min (a2, b2, and c2) using (a1 and a2) non-textured HSS tool; (b1 and b2) dimple-textured HSS tool; and (c1 and c2) spot-textured HSS tool.

6.3.3.5 Surface Roughness of the Machined Workpiece

Figure 6.17 presents average surface roughness of the turned Ti-6Al-4V workpiece using dimple-textured, spot-textured and non-textured HSS tools at different cutting speeds. It can be observed from this figure that (i) spot-textured and non-textured HSS tools respectively yielded minimum and maximum values of average surface roughness 'R_a' of the turned Ti-6Al-4V workpiece at both the cutting speeds; (ii) R_a value decreases considerably and slightly with increase in cutting speed for the spot-textured and dimple-textured tools respectively. But, there is no significant change in R_a value for the non-textured tool in fact error bar shows that in some cases it may increase with cutting speed.

These observations can be explained with help of the fact that spot texturing increases the gap between the chip and rake face of the HSS tool which enhances supply of the machining fluid. This increases heat dissipation from the cutting tool reducing its wear. This leads to lesser temperature rise (Fig. 14) and flank wear (Fig. 15) of the spot-textured tool which results in the better surface finish (Zheng et al. 2018).

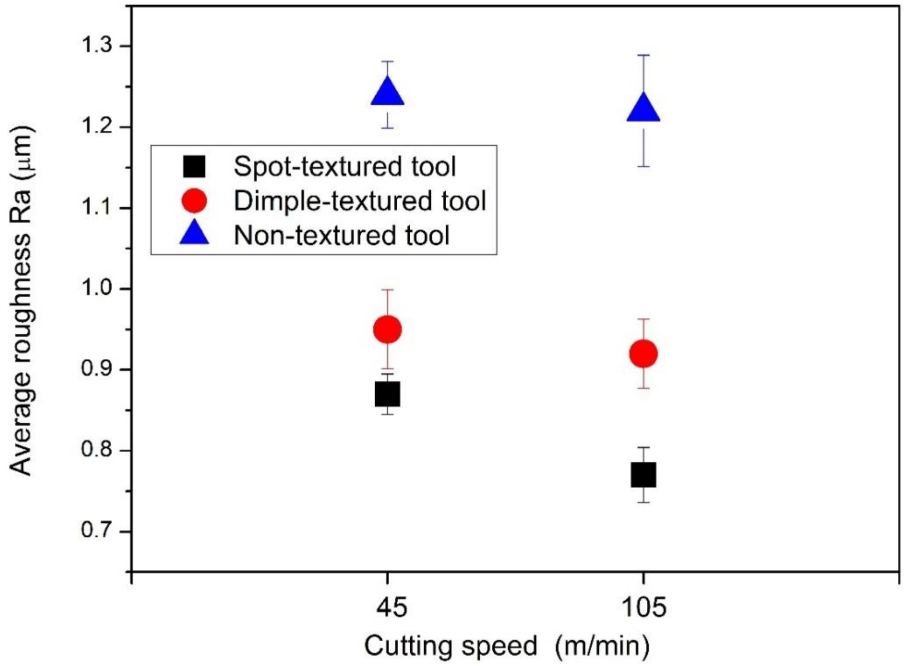

Fig. 6.17: Average surface roughness of the turned Ti-6Al-4V alloy workpiece using the dimple-textured, spot-textured and non-textured HSS machining tools.

6.4 Concluding Remarks

Following concluding remarks can be made from the investigations on texturing of the HSS tool by μ-PTAPD process and comparative study of the textured and non-textured HSS machining tools during cylindrical turning of the Ti-6Al-4V alloy workpiece by them:

- Use of spot-textured HSS machining tool in cylindrical turning of Ti-6Al-4V alloy workpiece resulted in least values of cutting force, thrust force, tool temperature, flank wear and average surface roughness value of the turned workpiece than the dimple-textured and non-textured HSS machining tools at different cutting speed. Performance of the dimple-textured HSS tool was better than the non-textured tool in these aspects.
- At higher cutting speed (i.e. 105 m/min), only spot-textured HSS tool resulted in formation of segmented chips during turning of Ti-6Al-4V whereas dimple-textured and non-textured HSS tools gave long continuously curling ribbon-like chips. But, at lower cutting speed (i.e. 45 m/min), both the spot-textured and dimple-textured HSS

tools resulted in formation of segmented chips whereas non-textured tool formed long continuously curling ribbon-like chips. Spot-textured HSS tool also showed adhesion of least amount of workpiece material to the tool than the dimple-textured and non-textured tools.

- By virtue of their shapes, spots act as fins which enhance convective heat transfer to the machining fluid or the surroundings. It helps in improving life of the HSS tools during machining of Ti-6Al-4V.
- This study proves that spot texturing of rake face of HSS machining tools by μ-PTAPD process is an economical, effective and environment friendly method to improve machining of titanium alloys.

The ***next chapter*** presents development of the generic mathematical model to predict dilution of single-layer single-track deposition by μ-PTAPD process and its experimental validation.

Chapter 7

Modeling of Dilution

Characteristics of single-layer single-track deposition by μ-PTAPD process depend on micro-plasma power, travel speed of the deposition head, powder mass flow rate, and thermal properties of the deposition and substrate materials. Dilution of single-layer single-track deposition can be predicted using fundamental principles of energy balance equation. This requirement can be met by developing a mathematical model in terms of process efficiency, parameters of μ-PTAPD process and material properties of the substrate and deposition materials. Such model should be generic in the sense that its applicability should be independent of combination of the deposition and substrate materials. This chapter describes the development of a generic mathematical model to predict dilution of single-layer single-track deposition by μ-PTAPD process along with its experimental validation.

7.1 Process Efficiency

Understanding and use of different efficiencies relevant to an additive manufacturing process such as energy transfer efficiency, melting efficiency and deposition efficiency are required to develop a generic model between dilution of the deposition and μ-PTAPD process parameters. Following paragraphs describe details of these efficiencies.

7.1.1 Energy Transfer Efficiency

The energy transfer efficiency 'η_a' represents fraction of the input energy transferred to the substrate material. It is ratio of energy transferred to the substrate to energy supplied to heat source.

$$\eta_a = \frac{Energy\ transferred\ to\ the\ substrate}{Energy\ supplied\ to\ the\ heat\ source} \tag{7.1}$$

7.1.2 Melting Efficiency

The melting efficiency 'η_m' represents the fraction of the absorbed energy which is actually utilized for the melting. The melting efficiency depends on the AM process parameters and the material properties. It is defined as the ratio between the energy used for melting the deposition and the substrate materials and the energy transferred to the substrate material.

$$\eta_m = \frac{Energy\ used\ for\ melting\ the\ deposition\ and\ the\ substrate\ materials}{Energy\ transferred\ to\ the\ substrate} \tag{7.2}$$

The melting efficiency can also be calculated by the following equation which is given by Okada (1977).

$$\eta_m = exp^{-\left(1+\frac{\alpha_s^2 \Delta H_s \rho_s}{1.14\eta_a PT}\right)} \qquad (7.3)$$

Where, α_s is thermal diffusivity of the substrate material (m^2/s); ΔH_s is change in enthalpy of the substrate material (J/kg); ρ_s is density of the substrate material (kg/m^3); P is micro-plasma power (W); T is the relative speed between the worktable and the deposition head (m/s); and η_a is the energy transfer efficiency (%).

7.1.3 Deposition Efficiency

Deposition efficiency 'η_d' is measure of deposition material utilization. It is the ratio between amount of the material deposited on the substrate and the amount of deposition material delivered to the melt pool. It can be calculated using following equation:

$$\eta_d = \frac{(W_t - W_s)}{W_p} \times 100 \qquad (7.4)$$

Where, W_t is combined weight of the deposition and the substrate material (g); W_s is weight of the substrate material (g), W_p is weight of deposition material delivered to the melt pool (g).

Table 7.1 presents the calculated deposition efficiency of µ-PTAPD process for Ti-6Al-4V deposition on substrate of the same material and Stellite 6 deposition on AISI 4130. It shows that deposition efficiency varies in the range from 76.4 to 89.3 %.

Table 7.1: Calculated deposition efficiency for deposition of Ti-6Al-4V powder on substrate of the same material and deposition of powder of Stellite 6 powder on AISI 4130 substrate by µ-PTAPD process along with corresponding process parameters.

Micro-plasma power '*P*' (W)	Powder mass flow rate of '*f*' (g/min)	Travel speed of deposition head '*T*' (mm/min)	Average value of the deposition efficiency (%)
For deposition of Ti-6Al-4V powder on the same material substrate			
418	2.1	52	89.1
418	2.1	62	79.5
429	1.5	57	85.2
440	1.5	52	89.3
440	2.7	62	79.3
For deposition of Stellite powder on AISI 4130 substrate			
407	3.5	125	76.4
418	1.7	80	81.2
429	2.9	100	84.3
429	1.7	80	87.2
429	3.5	125	79.8

7.2 Assumptions

Following assumption were made in developing model of dilution for single-layer single-track deposition by μ-PTAPD process:

- Thermal properties of the deposition and substrate materials are temperature independent.
- Micro-plasma arc is perpendicular to the substrate material and stand-off-distance between deposition head and substrate is constant.
- Radiative and convective heat losses from the substrate material to the surroundings are neglected.
- Energy transfer efficiency 'η_a' of the micro-plasma arc has been considered as 55 % (Nikam et al. 2016).
- Substrate is a semi-infinite block at the ambient temperature.
- Shape of melt pool is constant throughout the deposition process.
- Deposition efficiency 'η_d' is considered as 83 % (taken as average of the deposition efficiencies mentioned in the Table 7.1).

7.3 Development of Model for Dilution

Dilution is ratio of the diluted area 'A' to the sum of the diluted area 'A' and deposited area 'B' and is expressed as percentage (as shown in Eq. 7.5). It quantifies the relative amount of the substrate material mixed with the deposited material.

$$\text{Dilution } = \frac{\mathrm{A}}{(\mathrm{A}+\mathrm{B})} \times 100 \qquad (7.5)$$

Using the fundamental principle of energy balance to equate the total energy available for melting with the energy required to melt the deposition and substrate materials. The energy balance equation is given by

$$\eta_a \eta_m P t = (n_d V_d \rho_d \Delta H_d) + (V_s \rho_s \Delta H_s) \qquad (7.6)$$

Where, ΔH_d is change in enthalpy of the deposition material (J/kg); ρ_d is density of the deposition material (kg/m^3); V_d is volume of the deposited material (m^3); ΔH_s is change in enthalpy of the substrate material (J/kg); ρ_s is density of the substrate material (kg/m^3); V_s volume of the diluted substrate material (m^3); P is micro-plasma power (W); t is the deposition time (second); η_a is the energy transfer efficiency (%); η_m is the melting efficiency; and η_d is the deposition efficiency (%).

Rearranging the Eq. 7.6 to get relationship for volume of diluted substrate 'V_s' (m^3) yields the following equation

$$V_s = \frac{(\eta_a \eta_m P t) - (\eta_d V_d \rho_d \Delta H_d)}{\rho_s \Delta H_s} \tag{7.7}$$

Volume of deposited material 'V_d' for the powdered form can be calculated using the following relation

$$V_d = \frac{\eta_d f_v\, l}{T} \tag{7.8}$$

Where, f_v is volumetric feed rate of the deposition material (m^3/s); l is length of the deposition (m); T is the relative speed between the worktable and the deposition head (m/s); and η_d is the deposition efficiency (%). Dilution of single-layer single-track deposition can be expressed on volumetric basis by multiplying area of diluted substrate material and area of the deposited material by length of single-layer single-track deposition i.e. Eq. 7.5 can be rewritten as

$$D = \frac{V_s}{(V_s + \eta_d V_d)} \times 100 \tag{7.9}$$

$$D = \left(1 + \frac{\eta_d V_d}{V_s}\right)^{-1} \times 100 \tag{7.10}$$

Substituting Eq. 7.7 in the Eq. 7.10 yields following expression for dilution as a function of μ-PTAPD process parameters and the material properties

$$D = \left(1 + \frac{\eta_d V_d \rho_s \Delta H_s}{(\eta_a \eta_m P t) - (\eta_d V_d \rho_d \Delta H_d)}\right)^{-1} \times 100 \tag{7.11}$$

7.4 Experimental Validation

The developed mathematical model for dilution of single-layer single-track deposition (Eq. 7.11) was experimentally validated depositing Ti-6Al-4V powder on substrate of the same material and depositing Stellite powder on AISI 4130 steel substrate by μ-PTAPD process.

7.4.1 For Deposition of Ti-6Al-4V Powder on Ti-6Al-4V Substrate

Five experiments were conducted to validate the model predicted values of dilution of single-layer single-track deposition of Ti-6Al-4V powder deposition on substrate of the same material (having material properties as: 1910 K as melting temperature; 4430 kg/m^3 as density; 526.3 J/kgK as specific heat; and 6.7 W/mK as thermal conductivity) by μ-PTAPD process. Table 7.2 presents the model predicted and experimentally measured values of dilution for five experiments whereas Figure 7.1 depicts their comparison graphically. It can be seen from this figure that error between the model predicted and experimental values of dilution (as shown in Fig. 7.1) in a range from -16 to 6.41 %.

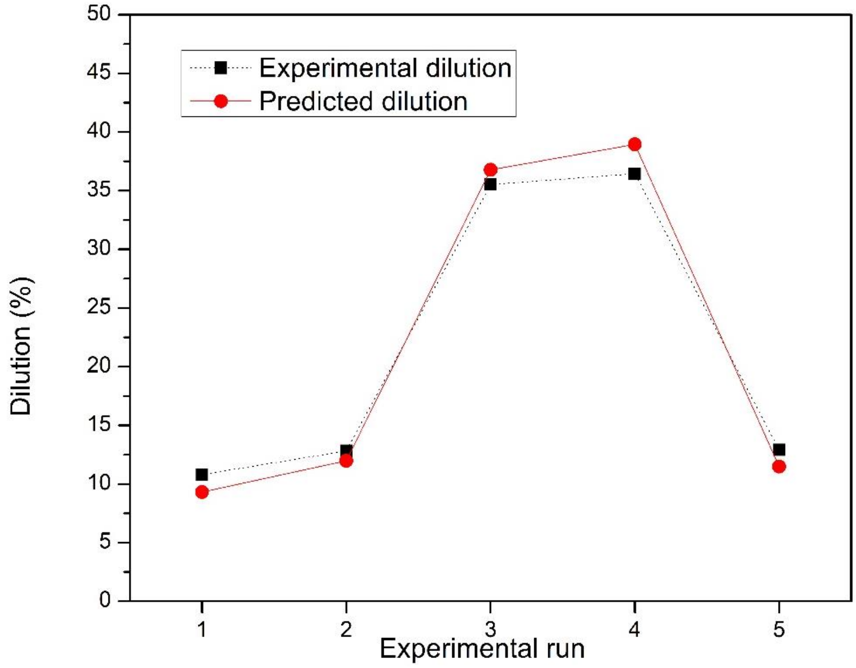

Fig. 7.1: Comparison of predicted and experimental values of dilution for single-layer single-track deposition of Ti-6Al-4V powder on substrate of the same material by µ-PTAPD process.

Table 7.2: Predicted and experimental values of dilution of single-layer single-track deposition of Ti-6Al-4V powder on substrate of the same material and deposition of Stellite powder on AISI 4130 steel substrate by µ-PTAPD process along with corresponding combination of input parameters.

Exp. No.	Variable input parameters			Dilution of deposition	
	Micro-plasma power *'P'* (W)	Powder mass flow rate of *'f'* (g/min)	Travel speed of deposition head *'T'* (mm/min)	Model predicted dilution	Experimental value of dilution
For deposition of Ti-6Al-4V powder on the same material substrate					
1.	418	2.1	52	9.31	10.8
2.	418	2.1	62	11.98	12.82
3.	429	1.5	57	36.78	35.52
4.	440	1.5	52	38.95	36.45
5.	440	2.7	62	11.49	12.9
For deposition of Stellite powder on AISI 4130 steel substrate					
6.	407	3.5	125	6.5	6.3
7.	418	1.7	80	12.58	14.7
8.	429	2.9	100	12.55	12.3
9.	429	1.7	80	19.4	18.2
10.	429	3.5	125	17.62	15.1

7.4.2 For Deposition of Stellite Powder on AISI 4130 Steel Substrate

Five experiments were conducted to validate the model predicted values of dilution of single-layer single-track deposition of Stellite powder on AISI 4130 steel substrate by μ-PTAPD process. Following properties were used in this experimental validation: (i) For Stellite 6: 1667 K as melting temperature; 8690 kg/m^3 as density; and 456 J/kgK as specific heat; (ii) for AISI 4130 steel: 1672 K as melting temperature; 7830 kg/m^3 as density; 479 as J/kgK specific heat; 40.1 W/mK as thermal conductivity. Table 7.2 presents the predicted and experimentally measured values of dilution whereas Figure 7.2 depicts their comparison graphically. It can be seen from this figure that error between the predicted and experimental dilution (as shown in Fig. 7.2) in a range from -16.85 to 14.30%.

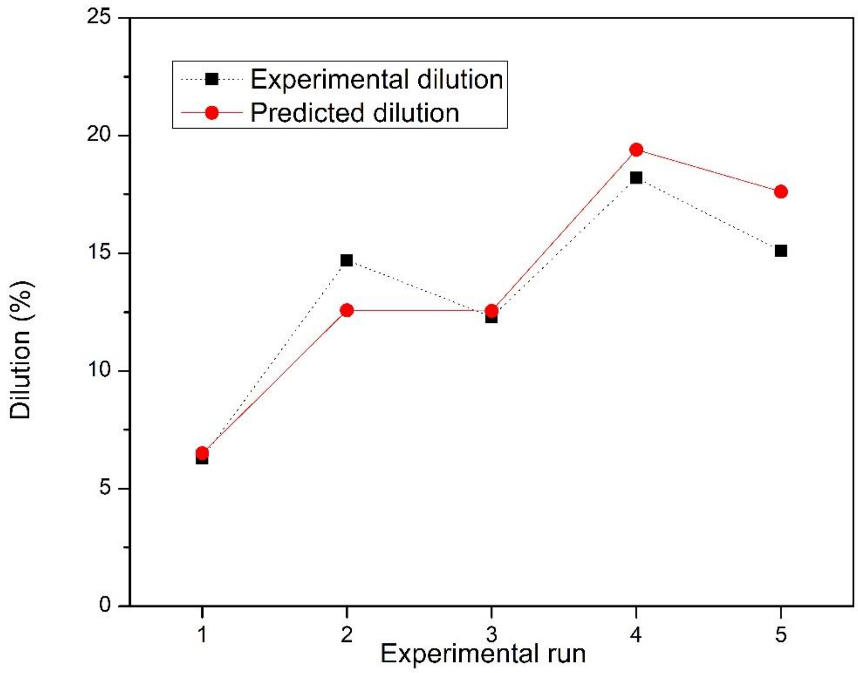

Fig. 7.2: Comparison of predicted and experimental values of dilution for single-layer single-track deposition of Stellite 6 on AISI 4130 by μ-PTAPD process.

7.5 Concluding Remarks

- The developed model has wide applicability because it is based on the material properties of the substrate and the deposition materials and μ-PTAPD process parameters. Therefore, it can be used for predicting dilution of single-layer single-track deposition by μ-PTAPD process for any combination of substrate and deposition materials.

- The error between the predicted and experimental dilution for Ti-6Al-4V deposition on the same substrate and Stellite 6 deposition on AISI 4130 is in range from -16 to 6.41 % and -16.85 to 14.30 % respectively.
- Disagreement between the model predicted and experimental results may be due to the assumptions made such as neglecting convective and radiative heat losses and neglecting dependence of the material properties on temperature.

The ***last chapter*** summarizes the significant achievements and conclusions from the research work reported in this thesis along with the identified directions for the future research work.

Chapter 8

Conclusions and Scope for Future Work

This chapter summarizes the significant achievements and conclusions from the research work reported in this PhD thesis along with the identified directions for the future research work.

8.1 Significant Achievements

The aim of the present research was to establish μ-PTAPD process as a cost effective and energy efficient alternative to existing additive manufacturing processes. Following are the significant achievements of the present research work:

- Successful development of the experimental apparatus for μ-PTAPD process having microcontroller programmable movement of the micro-plasma deposition head along X, Y and Z axes for various AM applications of the metallic materials.
- Development of the feeding system to ensure an uninterrupted supply of the deposition material in powdered form having capability to handle the powder particle size in the range from 20 to 200 μm.
- Development of the deposition head consisting of the micro-plasma torch surrounded by four identical nozzles placed in an inclined manner circumferentially at equal angular interval enabling supply of the powdered deposition material at feed angle of 46^0 to the centre of melt pool for the stand-off-distance from 8 to 10 mm. Value of the feed angle was chosen in such a way that ensures maximum powder deposition efficiency.
- Development of an interface with Arduino based microcontroller to control movement of the deposition head along X, Y and Z axes.

8.2 Conclusions

The work presented in this thesis illustrates the potential of μ-PTAPD process for Stellite coating, additive manufacturing of typical components from titanium alloy and texturing of HSS machining tool. Following conclusions can be made from these investigations:

8.2.1 For Stellite Coating

- For single-track deposition of Stellite (i) deposition height decreases with increase in micro-plasma power and worktable travel speed while increases with powder mass flow rate; (ii) deposition width decreases with increase in worktable travel speed, increases with powder mass flow rate and not affected by micro-plasma power; (iii) dilution increases with micro-plasma power and decreases with increase in worktable travel speed and powder mass flow rate.

- Deposition height of multi-track increases with overlapping but its dilution decreases with it. Overlapping value of 30% was found as optimum for multi-track deposition of Stellite.
- Phase analysis of Stellite coating revealed that primary phase consists of cobalt matrix consisting of ε-Co and α-Co having HCP and FCC crystal structure respectively mixed with chromium-rich carbides ($C_{r23}C_6$, $C_{r7}C_3$), and tungsten containing complex carbides (W_2C).
- Travel speed of worktable found to be the most important parameter affecting the characteristics of Stellite coating.
- Stellite coating using higher value of travel speed of worktable had smaller SDAS value, lower iron content and higher microhardness due to higher cooling rate and consequently formation of finer carbides.
- Stellite coating using lower travel speed of worktable yielded larger SDAS value, higher iron content and lower microhardness due to lower cooling rate and consequently formation of coarser carbides.
- Stellite coating manufactured by μ-PTAPD and laser-based deposition processes had smaller HAZ, absence of defects and finer dendritic structure with smaller SDAS value than the coating manufactured by PTA deposition.
- μ-PTAPD and laser-based deposition processes are capable of manufacturing thin coatings of less than 1 mm with lower dilution. It is suitable for wear and corrosion resistant applications where strong bond of thin coating with the substrate material is required.
- Stellite coating manufactured by μ-PTAPD process had almost similar value of average microhardness (553 HV) that manufactured by laser-based deposition (551 HV) and much higher than the coating manufactured by PTAD process (501 HV).
- Stellite coating by μ-PTAPD and laser-based deposition result in a relatively stable coefficient of friction with considerably minor variations and wear of Stellite coating by very shallow grooves while PTAD shows irregular fluctuations with higher coefficient of friction and wear of coating material by extensive ploughing.

- Stellite coating by μ-PTAPD and laser-based deposition processes exhibited lower wear volume than PTA deposition.
- This proves that μ-PTAPD process has the capability to selectively deposit a thin and sound quality coating of Stellite on metallic substrates. It provides advantages of the laser-based deposition for Stellite coating at much lower cost and higher energy and material efficiency. This establishing μ-PTAPD process capable of providing better techno-economic solution than the existing processes for Stellite coating.

8.2.2 For Additive Manufacturing of Component from Titanium Alloy

- Single-layer single-track deposition of Ti-6Al-4V by μ-PTAPD process has deposition height and width in the range of 1.52 to 2.3 mm and 2.68 to 3.3 mm respectively. Higher mass flow rate of powder and travel speed of deposition head result in smaller values of energy consumption per unit traverse length and power consumption per unit mass flow rate of powder and vice-versa.
- Multi-layer single-track depositions of Ti-6Al-4V in both continuous and dwell-time modes have smaller lamellae widths in the top region than that in the bottom region. Lamellae widths of the dwell-time deposition are smaller than that of continuous deposition. Faster cooling rate in dwell-time deposition decreases lamellae width and results in the finer microstructure. Ductility increases with increase in lamellae width but ultimate and yield strength decreases.
- Multi-layer single-track deposition of Ti-6Al-4V in continuous mode has cracks, weak bonding and coarser lamellar microstructure. Fracture of its tensile specimen showed occurrence of tear ridges or elongated regions. Its wear takes place by formation of deep grooves by repetitive ploughing and eventually breaking of grooves' edges.
- Multi-layer single-track deposition of Ti-6Al-4V in dwell-time mode yielded higher deposition efficiency and lower deposition waviness than continuous deposition i.e. continuous deposition will require more finishing which increases cost and wastage of the deposition material. It had good deposition quality with fine partial martensite and basket-weave microstructure. It possessed higher yield and ultimate strength. Fractured surface of its tensile specimen exhibited fine dimple rupture.
- Multi-layer single-track deposition of Ti-6Al-4V in dwell-time mode has higher microhardness, lower wear volume, coefficient of friction than the deposition in continuous mode. Its wear takes place by micro-ploughing which forms very shallow grooves and micro-cutting resulting in very less wear debris. This is important because

titanium alloys are widely used in biomedical applications such as knee implants, hip joints, surgical devices, bone screws, bone plates, dental implants and industrial applications of compressor blades, fan blades, hubs and discs where wear resistance is extremely important requirement.

- Comparative evaluation confirms that multi-layer single-track deposition of Ti-6Al-4V by μ-PTAPD process in dwell-time mode has higher efficiency in power consumption and cost-effective than laser-based deposition processes and yields higher microhardness which will result in smaller wear volume.
- It demonstrates that μ-PTAPD process has capability to additively manufacture complex part geometry of different metallic materials including titanium alloys. It can be used for similar as well as dissimilar deposition and substrate materials.

8.2.3 Texturing of HSS Machining Tool

- Micro-plasma power as 264 W and exposure time as 45 seconds were identified as optimum values to obtain dimple-texture with high aspect ratio and approximately circular shape. They were used for producing an array of dimple texture on the rake face of the HSS tool.
- Micro-plasma power as 316 W; exposure time as 14 seconds; and powder mass flow rate as 1.76 g/minute were identified as optimum values to achieve approximately sphere-shaped spot-textures having high dilution ratio and minimum unmolten particles attached. These values were used to produce an array of spot-textures on the rake face of the HSS tool.
- Use of spot-textured HSS machining tool in cylindrical turning of Ti-6Al-4V alloy workpiece resulted in least values of cutting force, thrust force, tool temperature, flank wear and average surface roughness value of the turned workpiece than the dimple-textured and non-textured HSS machining tools at different cutting speed. Performance of the dimple-textured HSS tool was better than the non-textured tool in these aspects.
- At higher cutting speed (i.e. 105 m/min), only spot-textured HSS tool resulted in formation of segmented chips during turning of Ti-6Al-4V whereas dimple-textured and non-textured HSS tools gave long continuously curling ribbon-like chips. But, at lower cutting speed (i.e. 45 m/min), both the spot-textured and dimple-textured HSS tools resulted in formation of segmented chips whereas non-textured tool formed long continuously curling ribbon-like chips. Spot-textured HSS tool also showed adhesion

of least amount of workpiece material to the tool than the dimple-textured and non-textured tools.

- By virtue of their shapes, spots act as fins which enhance convective heat transfer to the machining fluid or the surroundings. It helps in improving life of the HSS tools during machining of Ti-6Al-4V.
- This study proves that spot texturing of rake face of HSS machining tools by µ-PTAPD process is an economical, effective and environment friendly method to improve machining of titanium alloys.

8.2.4 Modelling of Dilution

- The developed model has wide applicability because it is based on the material properties of the substrate and the deposition materials and µ-PTAPD process parameters. Therefore, it can be used for predicting dilution of single-layer single-track deposition by µ-PTAPD process for any combination of substrate and deposition materials.
- The error between the predicted and experimental dilution for Ti-6Al-4V deposition on the same substrate and Stellite 6 deposition on AISI 4130 is in range from -16 to 6.41 % and -16.85 to 14.30 % respectively.
- Disagreement between the model predicted and experimental results may be due to the assumptions made such as neglecting convective and radiative heat losses and neglecting dependence of the material properties on temperature.

8.3 Scope for the Future Work

Since the present work was the first attempt to establish µ-PTAPD process as an alternative to the existing AM processes for different metallic materials therefore, there is plenty scope for future research in this area as mentioned below:

- The present study was conducted using 3 axes automated manipulator system. It can be extended to use 5 axes automated manipulators such as CNC machine or robotics to manufacture complex parts.
- The present study was limited for the Stellite coating and the additive manufacturing of titanium alloy. However, additive manufacturing of some other very useful materials such as functionally graded material (FGM), shape memory materials (SMM), metal matrix composites (MMC), and nano-composites by µ-PTAPD process can be investigated which extend the applications of µ-PTAPD process in areas of nuclear, space, biomedical engineering and related areas.

- Use of adaptive control and following automation strategies in µ-PTAPD process can be explored to enhance its capabilities and to more robustly challenge the energy beam based AM processes:
  - Use of computer-aided manufacturing (CAM) system for the simulation
  - On-line monitoring and control to improve the deposition quality
  - Industry 4.0 for the current trend of automation and data exchanges by cyber-physical system.
- The process can be integrated with some finishing processes to reduce total manufacturing time.

References

Afonso D., Pires L., Alves de Sousa R., Torcato R., **2017.** Direct rapid tooling for polymer processing using sheet metal tools. **Procedia Manufacturing,** 13, 102-108. https://doi.org/10.1016/j.promfg.2017.09.016

Apay S., Gulenc B., **2014.** Wear properties of AISI 1015 steel coated with Stellite 6 by microlaser welding. **Materials & Design**, 55, 1-8. https://doi.org/10.1016/j.matdes.2013.09.056

Astcad, **2015**, https://www.astcad.com.au/cad-innovations-in-rapid-prototyping/

Brandl, E., Palm, F., Michailov, V., Viehweger, B., Leyens, C., **2011.** Mechanical properties of additive manufactured titanium (Ti-6Al-4V) blocks deposited by a solid-state laser and wire. **Materials & Design**, 32, 4665-4675. https://doi:10.1016/j.matdes.2011.06.062

Baufeld, B., Brandl, E., and Van Der Biest, O., **2011.** Wire Based Additive Layer Manufacturing: Comparison of Microstructure and Mechanical Properties of Ti-6Al-4V Components Fabricated by Laser-Beam Deposition and Shaped Metal Deposition. **Journal of Materials Processing Technology**, 211, 1146-1158. https://doi.org/10.1016/j.jmatprotec.2011.01.018

Cengel, Y. A., **2002.** Heat Transfer: A Practical Approach, second ed., McGraw-Hill, USA, 156-166.

Chandramohan, P., Bhero, S., Obadele, B.A., Olubambi, P.A., **2017.** Laser additive manufactured Ti-6Al-4V alloy: tribology and corrosion studies. **The International Journal of Advanced Manufacturing Technology,** 92, 3051-3061 https://doi.org/10.1007/s00170-017-0410-2

Chang, S.S., Wu, H.C., Chen, C., **2008**. Impact wear resistance of Stellite 6 hard faced valve seats with laser cladding. **Materials and Manufacturing Process,** 23, 708-713. https://doi.org/10.1080/10426910802317102

da Silva, R.B., Machado, Á.R., Ezugwu, E.O., Bonney, J., Sales, W.F., **2013.** Tool life and wear mechanisms in high speed machining of Ti-6Al-4V alloy with PCD tools under various coolant pressures. **Journal of Materials Processing Technology,** 213, 1459-1464. https://doi.org/10.1016/j.jmatprotec.2013.03.008

Edwards, P., O’Conner, A., Ramulu, M., **2013**. Electron beam additive manufacturing of titanium components: properties and performance. **Journal of**

Manufacturing Science and Engineering, 135, 61016-7. https://doi.org/10.1115/1.4025773

Feng, K., Chen, Y., Deng, P., Li, Y., Zhao, H., Lu, F., et al., **2017.** Improved high-temperature hardness and wear resistance of Inconel625 coatings fabricated by laser cladding. **Journal of Materials Processing Technology**, 243, 82-91. https://doi.org/10.1016/j.jmatprotec.2016.12.001

Gharbi, M., Peyre, P., Gorny, C., Carin, M., Morville, S., Le Masson, P., Carron, D., Fabbro, R., **2013.** Influence of various process conditions on surface finishes induced by the direct metal deposition laser technique on a Ti-6Al-4V alloy. **Journal of Materials Processing Technology,** 213, 791-800. https://doi.org 10.1016/j.jmatprotec.2012.11.015

Gholipour A., Shamanian M., Ashrafizadeh F., **2011**. Microstructure and wear behavior of Stellite 6 cladding on 17-4 PH stainless steel. **Journal of Alloys and Compounds,** 509, 4905-4909. https://doi.org/10.1016/j.jallcom.2010.09.216

Gunay, M., Korkut, I., Aslan, E., Seker U., **2005**. Experimental investigation of the effect of cutting tool rake angle on main cutting force. **Journal of Materials Processing Technology,** 166, 44-49. https://doi.org/10.1016/j.jmatprotec.2004.07.092

Gurr, M., Mülhaupt, R., **2016.** Rapid Prototyping. **Reference Module in Materials Science and Materials Engineering** https://doi:10.1016/B978-0-12-803581-8.01477-6

Han P., **2017**. Additive Design and Manufacturing of Jet Engine Parts, **Engineering**, 3 648-652. http://dx.doi.org/10.1016/J.ENG.2017.05.017

Hao X., Cui W., Li L., Li H., Khan A.M., He N., **2018**. Cutting performance of textured polycrystalline diamond tools with composite lyophilic/lyophobic wettabilities. **Journal of Materials Processing Technology,** 260, 1-8. https://doi.org/10.1016/j.jmatprotec.2018.04.049

Heralic A., Christiansson A. K., Lennartson B., **2012.** Height control of laser metal-wire deposition based on iterative learning control and 3D scanning. **Optics and Lasers in Engineering**, 50, 1230-1241. http://dx.doi.org/10.1016/j.optlaseng.2012.03.016

Horii, T., Kirihara, S., Miyamoto, Y., **2009.** Freeform fabrication of superalloy objects by 3D micro welding. **Materials & Design**, 30, 1093-1097.

https://doi.org/10.1016/j.matdes.2008.06.033

Hutasoit, N., Yan, W., Cottam, R., Brandt, M., Blicblau, A., **2013.** Evaluation of microstructure and mechanical properties at the interface region of laser-clad Stellite 6 on steel using nanoindentation. **Metallography, Microstructure, and Analysis,** 2, 328-336. https://doi.org/10.1007/s13632-013-0093-5

Jandric, Z., Labudovic, M., Kovacevic, R., **2004.** Effect of heat sink on microstructure of three-dimensional parts built by welding-based deposition. **International Journal of Machine Tools & Manufacture,** 44, 785-796. https://doi.org/10.1016/j.ijmachtools.2004.01.009

Jain N.K., Sawant M.S., Nikam S.H., Jhavar S., **2016**. Metal Deposition: Plasma-Based Processes. **Encyclopedia of Plasma Technology** (Editor: J. Leon Shohet), CRC Press, pp. 722-740 (eBook ISBN: 978-1-4822-1431-4). doi: 10.1081/E-EPLT-120053919.

Jendrzejewski R., Navas C., Conde A., de Damborenea J. J., Gerard S., **2008.** Properties of laser-cladded Stellite coatings prepared on preheated chromium steel. **Materials & Design,** 29, 187-192. https://doi.org/10.1016/j.matdes.2006.10.020.

Jeshvaghani R.A., Shamanian M., Jaberzadeh M., **2011.** Enhancement of wear resistance of ductile iron surface alloyed by Stellite 6. **Materials & Design,** 32, 2028-2033. https://doi.org/10.1016/j.matdes.2010.11.060.

Jhavar, S., Jain N.K., Paul C.P., **2013.** Causes of failure and repairing options for dies and molds: A review. **Engineering Failure Analysis**, 34, 519-535. http://dx.doi.org/10.1016/j.engfailanal.2013.09.006

Jhavar, S., Jain N.K., Paul C.P., **2014**. Development of micro-plasma transferred arc (μ-PTA) wire deposition process for additive layer manufacturing applications. **Journal of Materials Processing Technology,** 214, 1102-1110. https://doi.org/10.1016/j.jmatprotec.2013.12.016

Kalpakjian S., Schmid S., **2014**. **Manufacturing Engineering & Technology**, Seven ed. Prentice Hall, New York.

Karlsson, J., Snis, A., Engqvist, H., Lausmaa, J., **2013**. Characterization and comparison of materials produced by electron beam melting (EBM) of two different Ti-6Al-4V powder fractions. **Journal of Materials Processing Technology,** 213, 2109-2118. https://doi.org/10.1016/j.jmatprotec.2013.06.010

Leon A., Aghion E., **2017.** Effect of surface roughness on corrosion fatigue performance of AlSi10Mg alloy produced by Selective Laser Melting (SLM). **Materials Characterization** 131, 188-194. http://dx.doi.org/10.1016/j.matchar.2017.06.029

Li, N., Chen, Y., Kong, D., Tan, S., **2017.** Experimental investigation with respect to the performance of deep submillimeter-scaled textured tools in dry turning titanium alloy Ti-6Al-4V. **Applied Surface Science**, 187-199. https://doi.org/10.1016/j.apsusc.2017.01.166

Lin, J.J., Lv, Y.H., Liu, Y.X., Xu, B.S., Sun, Z., Li, Z.G., Wu, Y.X., **2016.** Microstructural evolution and mechanical properties of Ti-6Al-4V wall deposited by pulsed plasma arc additive manufacturing. **Materials & Design,** 102, 30-40. https://doi.org/10.1016/j.matdes.2016.04.018

Liu R., Yao J., Zhang Q., Yao M.X., Collier R., **2015.** Effects of molybdenum content on the wear / erosion and corrosion performance of low-carbon Stellite alloys. **Materials & Design**; 78, 95-106. https://doi.org/10.1016/j.matdes.2015.04.030

Lu Y., Huang G., Wang Y., Li H., Qin Z., Lu X., **2018**. Crack-free Fe-based amorphous coating synthesized by laser cladding. **Materials Letters,** 210, 46-50. http://dx.doi.org/10.1016/j.matlet.2017.08.125

Luo, F., Cockburn, A., Lupoi, R., Sparkes, M., O'Neill, W., **2012**. Performance comparison of Stellite 6 deposited on steel using supersonic laser deposition and laser cladding. **Surface and Coatings Technology,** 212, 119-127. http://dx.doi.org/10.1016/j.surfcoat.2012.09.031

Luo, F., Lupoi, R., Cockburn, A., Sparkes, M., O'neill, W., Yao, J., **2013.** Characteristics of Stellite 6 deposited by supersonic laser deposition under optimized parameters. **Journal of Iron and Steel Research, International,** 20, 52-57. https://doi.org/10.1016/S1006-706X(13)60056-4

Madadi F., Ashrafizadeh F., Shamanian M., **2012**. Optimization of pulsed TIG cladding process of Stellite alloy on carbon steel using RSM. **Journal of Alloys and Compounds,** 510, 71-77. https://doi.org/10.1016/j.jallcom.2011.08.073

Mahamood, R.M., Akinlabi, E.T., **2017**. Scanning speed and powder flow rate influence on the properties of laser metal deposition of titanium alloy. **The International Journal of Advanced Manufacturing Technology,** 91, 2419-

2426. https://doi.org/10.1007/s00170-016-9954-9

Martina, F., Mehnen, J., Williams, S.W., Colegrove, P., Wang, F., **2012.** Investigation of the benefits of plasma deposition for the additive layer manufacture of Ti–6Al–4V. **Journal of Materials Processing Technology,** 212, 1377-1386. https://doi.org/doi:10.1016/j.jmatprotec.2012.02.002

Motallebzadeh A., Atar E., Cimenoglu H., **2015**. Sliding wear characteristics of molybdenum containing Stellite 12 coating at elevated temperatures. **Tribology International,** 91: 40-47. https://doi.org/10.1016/j.triboint.2015.06.006

Nikam, S.H., Jain, N.K., Jhavar, S., **2016**. Thermal modeling of geometry of single-track deposition in micro-plasma transferred arc deposition process. **Journal of Materials Processing Technology,** 230, 121-130. https://doi.org/10.1016/j.jmatprotec.2015.11.022

Palčič, I., Balažic, M., Milfelner, M., Buchmeister, B., 2009. Potential of laser engineered net shaping (LENS) technology. **Materials and Manufacturing Processes**, 24, 750-753. https://doi.org/10.1080/10426910902809776

Sasi, R., Kanmani Subbu, S., Palani, I.A., **2017.** Performance of laser surface textured high speed steel cutting tool in machining of Al7075-T6 aerospace alloy. **Surface and Coatings Technology,** 313, 337-346. https://doi.org/10.1016/j.surfcoat.2017.01.118

Shoja-Razavi R., **2016**. Laser Surface Treatment of Stellite 6 Coating Deposited by HVOF on 316L Alloy. **Journal of Materials Engineering and Performance**, 25, 2583-2595. https://doi.org/10.1007/s11665-016-2138-9

Sugihara, T., Enomoto, T., **2017.** Performance of cutting tools with dimple-textured surfaces: A comparative study of different texture patterns. **Precision Engineering**, 49, 52-60. https://doi.org/10.1016/j.precisioneng.2017.01.009

Suryakumar, S., Karunakaran, K.P., Bernard, A., Chandrasekhar, U., Raghavender, N., Sharma, D., **2011**. Weld bead modeling and process optimization in hybrid layered manufacturing. **Computer Aided Design,** 43, 331-344. https://doi.org/10.1016/j.cad.2011.01.006

Wei, Y., Kim, M.R., Lee, D.W., Park, C., Park, S.S., **2017**. Effects of micro textured sapphire tool regarding cutting forces in turning operations. **International Journal of Precision Engineering and Manufacturing: Green Technology,** 4, 141-147. https://doi.org/10.1007/s40684-017-0017-y

Yılmaz, B., Karabulut, Ş., Güllü, A., **2018.** Performance analysis of new external chip breaker for efficient machining of Inconel 718 and optimization of the cutting parameters. **Journal of Manufacturing Processes**, 32, 553-563. https://doi.org/10.1016/j.jmapro.2018.03.025

Yuan, S., Zheng, Y., Kai Chua, C., Yan, Q., Zhou, K., **2017**. Electrical and Thermal Conductivities of MWCNT/Polymer Composites Fabricated by Selective Laser Sintering. **Composites Part A: Applied Science and Manufacturing**, 105, 203-213. https:// doi.org/10.1016/j.compositesa.2017.11.007

Zheng, G., Xu, R., Cheng, X., Zhao, G., Li, L., Zhao J., **2018.** Effect of cutting parameters on wear behavior of coated tool and surface roughness in high-speed turning of 300M. **Measurement**. https://doi.org/10.1016/j.measurement.2018.04.078

Zhong, M.; Liu, W.; Yao, K.; Goussain, J.; Mayer, C.; Becker, A. **2002**. Microstructural evolution in high power laser cladding of Stellite 6+WC Layers. **Surface and Coatings Technology**, 157, 128-137. https://doi.org/10.1016/S0257-8972(02)00165-2

Appendix A

Details of the Instruments Used for the Evaluation of Deposition Geometry and its Characterization

- **Leica Stereo Microscope (IIT Indore)**

Make	Leica Microsystems, Germany
Model	*EZ4HD*
Full frame image acquisition	2048 × 1536 pixels, 3.1 megapixels
Pixel size	3.2 µm × 3.2 µm

- **Scanning Electron Microscope (IIT Indore)**

Make	Carl Zeiss NTS GmbH, Germany
Model	*SUPRA 55*
Resolution	1.0 nm @ 15 kV 1.7 nm @ 1 kV 4.0 nm @ 0.1 kV
Acceleration Voltage	0.1 – 30 kV
Magnification	12x – 900,000 x
Stages	5-Axes Motorized Eucentric Specimen Stage X = 130 mm, Y = 130 mm and Z = 50 mm, T = -3° to + 70°, R = 360°

- **Microhardness Testing Machine (IIT Indore)**

Make	Walter UHL Technische Mikroskopie GmbH, Germany.
Model	*VMH002 V*
Load Range	1 grams – 2000 grams
Type of intender	Diamond square base hexagonal Pyramid

- **Tensile Testing Machine (IIT Indore)**

Make	Tinius Olsen USA
Model	*H50KL*
Load Range	1-50 kN
Clearance Between Columns	405 mm
Testing Speed Range	0.001 to 500 mm/min

- **Pin-on-disk Type Wear Test Machine (IIT Indore)**

Make	Ducom, USA
Model	*Ducom-TR20LE*
Load Range	1-60 N
Rotational Speed	1-500 rpm
Frictional Force Measurement	0-20 N

- **Linear Reciprocating Type Wear Testing Machine (IIT Indore)**

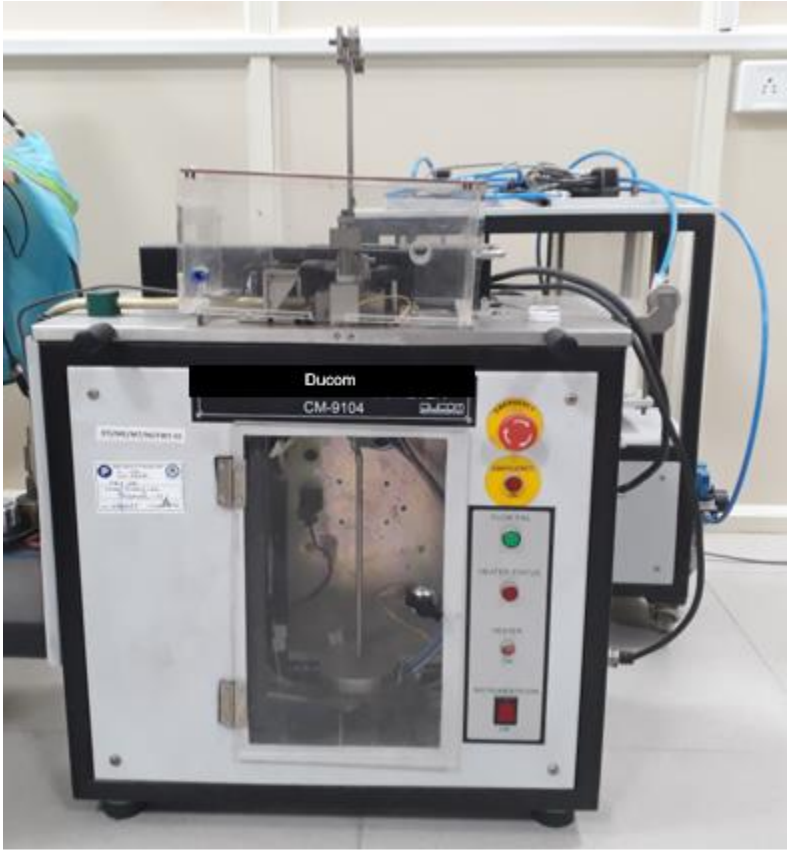

Make	Ducom, USA
Model	*Ducom- CM9104*
Load Range	1-200 N
Frequency	1-40 Hz
Stroke Range	1-30 mm

- **Surface Profilometer (IIT Indore)**

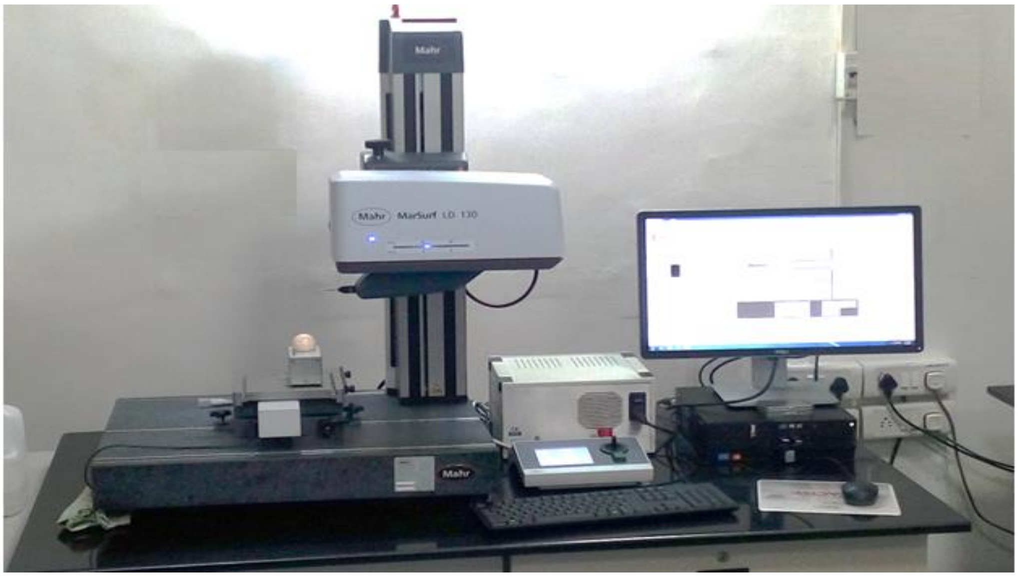

Make	Mahr GmbH, Germany
Model	*MarSurf LD 130*
Resolution	0.8 nm
Positioning speed	0.02 mm/s to 200 mm/s
Traversing lengths	0.1 mm - 130 mm